A study of the image formation model and noise characterization in SPECT imaging. Applications to denoising and epileptic foci localization.

Master Thesis in Electrical Engineering

Cecilia Aguerrebere Otegui

Advisors: Julie Delon and Pablo Musé

Instituto de Ingeniería Eléctrica
Facultad de Ingeniería
Universidad de la República

March 2011

Acknowledgements

First of all I would like to thank Julie and Pablo for their guide, their constant support and overall for their human warmth that always made work pleasant. I would also like to thank the Group of the Center of Nuclear Medicine at the Hospital de Clínicas for providing fundamental data for the correct development of this work. In particular, I would like to thank Dr. Rodolfo Ferrando for his constant disposition to answer all my questions, his help in providing and analyzing data and suggesting very useful ideas to continue the line of work in the field of biomedical engineering.
I would like to express my gratitude to the members of the committee: Dr. Gregory Randall, Dr. Alvaro Pardo and Dr. Rodolfo Ferrando. Their comments and questions have highly contributed to the improvement of this work. Besides, I am very grateful for the external reports made by Dr. Elsa Angelini and Dr. Alvaro Pardo. Their close reading of this work is of great importance, not only as a validation but also for their relevant and very interesting contributions.
Last but not least, I would like to thank my family, my friends, Mauricio and *tout le monde* that contributed, in the most varied ways, to complete this work.

Resumen

La epilepsia es una enfermedad neurológica que produce de forma espontánea repetidas alteraciones del funcionamiento normal del cerebro. La epilepsia refractaria es un tipo de epilepsia que no puede ser controlada con medicación. Dichos pacientes se ven imposibilitados de llevar una vida normal por la elevada frecuencia de sus crisis. En particular, los pacientes pediátricos pueden tener consecuencias severas sobre el neurodesarrollo. En estos casos se considera la cirugía para remover las células anormales causantes de las crisis. Esta técnica requiere una localización previa precisa de la región del cerebro donde se origina las crisis.

Imágenes SPECT de la actividad cerebral, durante y entre crisis, son obtenidas utilizando radiotrazadores que se acumulan y quedan fijos de forma proporcional al flujo sanguíneo cerebral local al momento de su administración. La técnica más utilizada para detectar los focos epileptógenos es umbralizar la diferencia de estas imágenes, corregistrada y normalizada. Este método ha demostrado gran utilidad, pero presenta algunas desventajas: los resultados dependen fuertemente del umbral elegido y presenta un alto número de falsas detecciones. Además, la elección del umbral no tiene una sólida base estadística.

En esta tesis se presenta un modelo matemático de la formación de las imágenes de SPECT y una caracterización estadística de las mismas. El modelo estadístico y las hipótesis realizadas son validadas por medio de tests estadísticos no paramétricos. Dicho modelo es luego aplicado al problema de la localización de focos epileptógenos utilizando un método basado en la teoría de a-contrario y el mejoramiento de la calidad de las imágenes de SPECT a través de la remoción de ruido en las mismas. Ambas técnicas, la propuesta para realizar la detección y la remoción de ruido, son evaluadas en fantomas y casos reales y validadas por un médico experto con profundo conocimiento de la historia clínica de los pacientes. Los resultados son prometedores: la localización de los focos epileptógenos muestra mejores resultados que la técnica clásica de umbralización, y el método de remoción de ruido parece mejorar globalmente la calidad de las imágenes de SPECT.

Abstract

Epilepsy is a brain disorder involving repeated, spontaneous episodes of disturbed brain function. Medically refractory epilepsy is a type of epilepsy that cannot be controlled with drugs. It may have strong disturbing effects in the daily life of the patient and, in particular, poor neurodevelopmental outcomes in children. Brain surgery to remove the abnormal cells causing the seizures may be considered in these situations. This technique requires a previous precise localization of the brain zone causing the seizure.

Tracers that accumulate and remain fixed proportional to regional cerebral blood flow at the time of injection are used to obtain SPECT images of the brain activity during and between seizures. The most used technique for detecting the epileptogenic zone (EZ) is to threshold the co-registered and normalized subtraction of these two images. This method has proven to be very useful but has some disadvantages: results depends on the selected threshold and abundance of false detections. Moreover, the choice of the threshold is not based on firm statistical basis.

In this thesis we present a mathematical model of the SPECT image formation process and a statistical characterization of these images. The statistical image model and the associated assumptions are validated by means of non-parametric statistical tests. Then, the model is applied to the problem of EZ localization by means of an a-contrario based detection approach and the improvement of SPECT image quality through denoising. Both detection and denoising are evaluated on phantoms and real cases, and validated by an expert physician with deep knowledge on the patients' medical histories. Results are promising: the EZ localization approach shows better performance than the classic thresholding technique, and the denoising method seems to globally improve the quality of SPECT images.

It is important to remark that the mathematical model presented for SPECT images may be used in a wide variety of applications, beyond the ones analyzed in this work, and may contribute to improve the performance of techniques developed for ET images.

Contents

1. Introduction **2**

I Modelization of the SPECT image formation process **5**

2. Emission Tomography **6**
2.1. What is emission tomography? . . . 6
2.2. Stages of an ET study . . . 7
2.3. ET data acquisition . . . 8
2.4. Reconstruction methods . . . 11
2.4.1. Analytic methods: FBP . . . 11
2.4.2. Iterative methods: ML-EM . . . 12
2.4.3. OSEM . . . 16

3. SPECT **19**
3.1. General principles . . . 19
3.2. The physics of SPECT . . . 20
3.2.1. Basic definitions . . . 20
3.2.2. Nuclear energy states . . . 20
3.2.3. Nuclear de-excitation and stability . . . 21
3.2.4. Nuclear decay statistical model . . . 21
3.2.5. Interactions of gamma-photons in matter . . . 23
3.3. Gamma cameras . . . 24
3.3.1. The Anger camera . . . 24
3.3.2. Principles of collimation . . . 26
3.3.3. Principles of detection . . . 26

4. SPECT Simulations **28**
4.1. Steps of an ET simulation . . . 28
4.1.1. Phantom definition . . . 28
4.1.2. Gamma-photon emission simulation . . . 29
4.1.3. ET acquisition simulation . . . 29
4.1.4. Image reconstruction . . . 30
4.1.5. Data analysis . . . 30
4.2. SimSET package . . . 30
4.2.1. Package description . . . 31
4.2.2. Importance sampling techniques . . . 33
4.3. Realistic SPECT simulations . . . 34

5. SPECT Images Characterization **35**
5.1. Sinogram Images Characterization . . . 35
5.1.1. Noise Sources . . . 36
5.1.2. Photon Emission Model . . . 37
5.1.3. First Stage: Photon evolution . . . 39
5.1.4. Second Stage: Acquisition Process . . . 41
5.1.5. Noise-free Sinogram Formation . . . 42
5.1.6. Experimental Validation . . . 45
5.2. Tomographic Images Characterization . . . 50
5.2.1. Image characterization after ML-EM reconstruction . . . 50
5.2.2. Extension to OSEM . . . 54
5.2.3. OSEM sensitivity to projection matrix . . . 56

II SPECT image model applied to epileptogenic foci localization **58**

6. Epileptogenic foci detection **59**
6.1. Epilepsy and the problem of epileptogenic zones localization . . . 59
6.2. Proposed solutions . . . 60
6.3. A-contrario EZ detection . . . 61
6.3.1. The a-contrario theory: basic concepts . . . 61
6.3.2. Application to EZ detection . . . 62
6.4. A-contrario EZ detection: new approach . . . 64
6.4.1. The new model . . . 64
6.4.2. The measurement . . . 66
6.4.3. Multi-scale approach . . . 67
6.4.4. Number of false alarms . . . 67
6.5. Experiments . . . 69
6.5.1. Simulations . . . 69
6.5.2. Real cases . . . 71

7. SPECT denoising **89**
7.1. Denoising photon low-counts images . . . 89
7.2. Poisson Non-local Means . . . 90
7.3. Experiments . . . 93
7.3.1. Simulations . . . 93
7.3.2. Real scans . . . 100
7.3.3. Thresholding . . . 101

8. Conclusions and future work **112**

Appendices **115**

A. V(r) expected value **115**

B. Pearson Chi-square test **117**

C. Rank Correlation Coefficients **118**
C.1. Spearman's rank correlation . . . 118
C.2. Kendall's rank correlation . . . 118

D. Post-reconstruction Noise - C and D matrices **119**

Chapter 1

Introduction

Single photon emission computed tomography (SPECT) is a diagnosis nuclear imaging technique that uses gamma-ray emissions to describe the spatial or spatial-temporal distribution of physiological processes. A radioactive labeled tracer is administered to the patient and the emitted gamma-photons are recorded to describe the properties of the physiological process of interest. Among other applications, it is used for cancer detection, myocardial perfusion assessment, infection or lymphoma detection, brain perfusion assessment. SPECT is an example of *functional* imaging technique, as opposed to *structural* imaging techniques as MRI, that principally depict the patients anatomy. In routine nuclear medicine imaging, SPECT studies are performed using one or more rotating gamma cameras, which acquire projections of the radionuclide distribution. Then, image reconstruction is performed to obtain the tomographic study from projections. Two major advantages of the SPECT over other functional medical imaging techniques, are its high sensitivity -very low quantities of radiotracer material can be detected- and the fact of being non-invasive -the concentration of radiotracer is estimated from counts of gamma rays emitted from within the body. The counterpart is the exposition to radioactive material suffered by the patient, which must be strictly controlled not to exceed safety limits. Another weakness of the SPECT study is its low spatial resolution. It depends on the gamma camera characteristics but may vary from 8mm to 4mm in the best case.

A particular application that makes use of SPECT studies is epilepsy. Epilepsy is a brain disorder involving repeated, spontaneous episodes of disturbed brain function that cause changes in attention or behavior. A particular kind of epilepsy, called medically refractory epilepsy, cannot be controlled with drugs. This type of epilepsy may have strong disturbing effects in the daily life of the patient and, in particular, poor neuro-developmental outcomes in children. Brain surgery to remove the abnormal cells causing the seizures may be a plausible action in these situations. This technique requires a previous precise localization of the brain zone causing the seizure, i.e. the epileptogenic zone (EZ). SPECT images are used for such purpose. The analysis of the studies by the specialists can be done either by visual inspection only, or including an image processing technique to assist the diagnosis.

Two principal methodologies based on functional neuroimaging techniques have been developed for EZ localization [1]. Both make use of at least two SPECT scans: the ictal scan, with the radiotracer administered at the beginning of the seizure; and the inter-ictal scan, performed in-between seizures. The scans are compared in order to find regions of high activity during the seizure (ictal scan) that are not so active in basal state (inter-ictal scan).

The first methodology considers differences in the ictal/inter-ictal comparison which are checked against a healthy normal database. Differences too far from normal behavior are considered EZ candidates. To perform this comparison, spatial normalization is first used to wrap images to a SPECT template [2]. This approach is problematic in that comparison against a normal database

is not always valid. It cannot, for example, be used on children (there are no healthy normal databases for children) or patients with anatomical lesions.

The second approach compares ictal and inter-ictal images of the same patient. Information from other patients is not included. The most common method to localize the EZ is to detect hyperperfusion regions on the ictal/inter-ictal subtraction image by thresholding. A global fixed threshold is used, usually proportional to the standard deviation of the gray level values in the subtraction image. Although the global thresholding technique has been evaluated and proven successful in EZ localization [3], there are some disadvantages to this method. The global approach is prone to corregistration, even when registration errors are low. Also high dependence on precise masking is observed. Regarding the choice of the threshold value, despite being based on clinical experience, it still lacks a solid statistical basis. An evident drawback is that this thresholding technique will always detect regions above the threshold, even in the absence of EZ.

In [1], we proposed a method that aims to determine detection thresholds from ictal/inter-ictal images of the same patient, in a more rigorous framework. We propose to use the a-contrario theory, a statistical framework developed by Desolneaux et al. [4]. Good results are obtained, with better defined activations in the EZ and less amount of false detections than the classical thresholding technique. The proposed solution appears to be more robust to registration errors than thresholding and less sensible to masking errors. The counterpart of the low number of false detections is having no detections in cases of known EZ presence. The threshold defined by this method turns out to be too restrictive in some cases. Despite being an statistically based approach, the statistical image model proposed in [1] was too naive and turned out not to be fully consistent with the underlying image formation physics. Because of this, we find the need to formalize the data analysis methods, studying in depth the SPECT image formation process and the resulting image characteristics. In this manner, a statistical model based on this study can be proposed for the SPECT scans. Once the model is proposed, statistical detection methods can be developed and applied to the EZ localization task. The EZ can be found as *rare* events in the SPECT image model.

In this work we present a study of the SPECT image formation process and develop an image characterization model based on it. We first define the noise sources in the SPECT generation process and then propose a mathematical model for the acquisition process. As will be presented in Section 5.1, we conclude that the pixels in the SPECT sinograms can be modeled as independent, Poisson distributed random variables. These variables are not identically distributed since the spatially non-stationary nature of the images imposes different underlying Poisson parameters for different pixels. The Poisson model for the detected photon counts is widely known and was presented by Barrett et al. [5] and Harrison et al. [6] for Anger like cameras and by Marcovski [7] for projection radiography. However, to the best of our knowledge, a detailed analysis of the acquisition process and justification of the conditions of validity of the previous assumption was not presented.

In Section 5.2, a statistical model is presented for the SPECT reconstructed images, which was introduced by Barrett et. al in [8]. Under an assumption of low noise level with respect to the mean reconstruction values, the SPECT image voxels are shown to follow a multivariate log-normal distribution. Thus, returning to the previous idea, the EZ candidates may be found as outliers in a log-normal model.

Including some extra precisions on the statistical image model, in Section 6.4 we present an extension of the a-contrario EZ detection method [1], which takes into account the log-normal distribution of SPECT images. Moreover, a local-global combined measurement is introduced, which covers different EZ sizes through a multi-scale approach. Inspired in the method proposed by Burrus et al. [9], different NFA thresholds are computed for each scale. The detection performance of the new approach is evaluated using both simulated and real scans. We found that it maintains the positive features of the previous a-contrario detection approach such as: robustness to

alignment and masking problems, correct foci definition and low number of false positives. Some improvements were found in the experimental evaluation. One of the most remarkable is the greater sensitivity of the new method (a lower detectable activity threshold). The new threshold is less restrictive than the previous one, allowing the reduction of false negatives, which is critical in the EZ localization application. Moreover, the reduction on the false negatives is achieved without a significant increase in false positives. The new threshold also allows the emergence of new detections that belong to the seizure activation circuit. This aspect is remarkable since the highly restrictive thresholding of the old a-contrario method gives *clean* images (low number of false detections) which are not in accordance with reality. The perfusion circuits are complex and several brain regions are active during the seizure.

Another application, where the SPECT statistical model has special utility, is the denoising of the sinogram images. Denoising may be considered complementary to detection, since it may assist the task of specialists improving the reconstructed image quality or even be used to improve the detection result itself. Knowing the characteristics of image noise should help choosing a denoising method and therefore contributes to improve several algorithm performance on this type of images. Based on the Poisson model proposed for the sinogram images, we applied a denoising technique specially developed for Poisson noise. The algorithm, presented in [9], is an extension of NL means to the case of images corrupted by Poisson noise. The denoising performance was evaluated using phantoms and real scans. In both cases results are promising. In particular, for real scans, the denoising method seems to improve edges definition and better distinguish small adjacent structures. Moreover, it seems to increase the intensity in areas of low uptake, as the temporal lobes, which is a positive aspect.

Outline

This manuscript is organized in two parts. Part I is focused on the SPECT images modelization, while Part II is devoted to the application of this model to the EZ localization task in medically refractory epilepsy. More precisely, Part I includes: a general description of the ET techniques, including the data acquisition process and reconstruction methods (Chapter 2); a general description of the SPECT technique, covering the basic physics acting on SPECT and the gamma camera operation description (Chapter 3); a description on how to perform SPECT simulations (Chapter 4); the study of SPECT images formation process and characterization, including sinograms and reconstructed image model (Chapter 5). In Part II we present the new a-contrario EZ detection method (Chapter 6) and the denoising techniques (Chapter 7). In both chapters, results on phantom and real patients are presented.

Part I

Modelization of the SPECT image formation process

Chapter 2

Emission Tomography

This chapter presents a general approach to emission tomography. In Section 2.1, we start describing the ET nuclear imaging technique, its fundamental aspects and variants. Next, in Section 2.2, we give a block diagram describing the stages that compose an ET study, with a brief description of each of them. Section 2.3 is devoted to describing the data acquisition stage in more detail, describing the planar projections acquisition by means of a gamma camera. Finally, in Section 2.4, we present the problem of image reconstruction and the description of two of the most widely used image reconstruction techniques: FBP and ML-EM, the latter with its variant OSEM.

2.1. What is emission tomography?

Emission tomography (ET) is a subset of the nuclear medicine techniques, which use radioactive materials to image characteristics of the body's physiology. It comprises two main techniques: single-photon emission computed tomography (SPECT) and positron emission tomography (PET). ET images can represent the spatial distribution of various physiological processes, like glucose metabolism, blood perfusion, receptors concentration, etc. For this reason these techniques are highly used, both to diagnose and assess the response to therapy, of a wide variety of diseases. Cancer, cardiac and neurological disorders (e.g. atherosclerosis, Alzheimer, epilepsy), psychiatric illnesses, are some examples of them. Table 2.1 [10] presents a brief summary of the principal applications of both, PET and SPECT. ET is an example of *functional* imaging techniques, as opposed to *structural* imaging techniques (e.g. MRI) that principally depict the patients anatomy. Figure 2.1 shows a comparative example of both of these techniques.

ET is founded on a major principle known as the *tracer principle*, proposed in the early 1900s by the Hungarian radio-chemist George de Hevesy. This principle states that radioactive compounds participate of physiological processes in the same way as non-radioactive materials. As radioactive compounds can be detected by means of their emission of gamma rays, they can be used to depict the flow and distribution of several substances on the body. The use of radioactive materials as a representative tracer of non-radioactive substances is the basis of the ET techniques. These materials are called **radiopharmaceuticals** or **radiotracers** and can be created to trace a wide variety of substances. They consist of two components: the *tracer compound*, e.g. fluorodeoxyglucose (FDG), that interacts with the body, and the *radioactive label*, e.g. ^{18}F, that allows the imaging through the radioactive emission. Radiotracers must present certain characteristics, among them: to be detectable by an observer, not to perturb the studied system when introduced and to have indistinguishable properties from those of the studied substance. Two major advantages of ET techniques over other functional medical imaging techniques, are its high sensitivity -very little quantities of radiotracer material can be detected- and the fact of being non-invasive -the concentration of radiotracer is estimated from counts of gamma rays emitted from within the body.

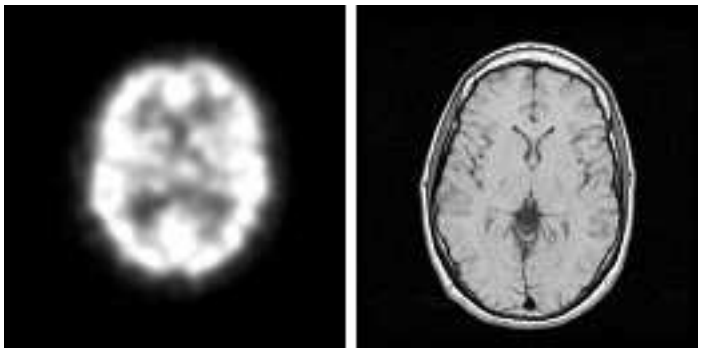

Figure 2.1: **Left:** SPECT image. **Right:** MRI image. Note the difference between the anatomical detail found in the MRI study and the much more diffuse nature of the functional image. Images provided by the Center of Nuclear Medicine of Hospital de Clínicas, Facultad de Medicina, Universidad de la República, Uruguay.

	Radiotracer	**Application**
SPECT	^{67}Ga citrate	Infection or lymphoma detection
	^{111}In capromab pentetide	Prostate cancer detection
	^{201}Tl TlCl	Myocardial perfusion or viability assessment
	^{99m}Tc TlCl	Brain lymphoma detection
	^{99m}Tc sestamibi or tetrofosmin	Myocardial perfusion or viability assessment
	^{99m}Tc MDP	Metastases or fracture detection
	^{99m}Tc HMPAO	Brain perfusion assessment
	^{99m}Tc RBCs	Liver hemangioma detection
	^{99m}Tc sulfur colloid	Liver/spleen assessment, lymphoscintigraphy
	^{99m}Tc sestamibi or tetrofosmin	Parathyroid localization
PET	^{18}F FDG	Characterization, diagnosis, staging, and restaging of many forms of cancer
		Solitary pulmonary nodule assessment
		Epilepsy (refractory seizures)
		Myocardial perfusion or viability assessment
	^{82}Rb RbCl	Myocardial perfusion or viability assessment

Table 2.1: Clinical applications of SPECT and PET and their corresponding radiotracers. From [10].

The counterpart is the exposition to radioactive material suffered by the patient, which must be strictly controlled not to exceed safety limits.

2.2. Stages of an ET study

Figure 2.2 shows a pipeline of the ET study representing the stages involved in the process. The first step is the production of the radiotracer, which depends on the particular application, since the radioactive material will be used for imaging a particular organ or disease. Radioactive labels can be classified into two broad groups: *positron emitters*, used in PET, and *single-photon emitters*, used in SPECT. Some of the most commonly used positron emitters are: ^{18}F, ^{82}Rb, ^{11}C and ^{15}O. And for single-photon emitters we have: ^{99m}Tc, ^{201}Tl, ^{123}I, ^{131}I. Their radioactive *half-life* ($t_{1/2}$) is listed in Table 2.2 [10]. The half-life is the average time in which the nuclei of half of a given population of atoms will undergo radioactive decay. Next, the radiotracer is administered to the patient, by injection or inhalation, the first being the most frequent one. The quality of the image increases with the dose of radiotracer. However, safety limits on radiation exposure of internal

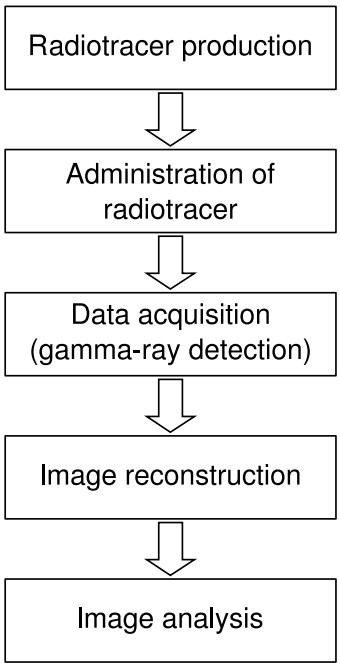

Figure 2.2: ET study pipeline representing the different stages that make up the process. Based on [10].

organs limit this dose.

The next step is the data acquisition by means of a gamma camera. It takes place with the patient lying still on a bed surrounded or revolved by the camera. The gamma camera detects and records the gamma-rays emanating from the body, caused by the radioactive decays of the radioactive isotope used to label the radiotracer. For example, more gamma-rays are emitted from a tumor than from the surrounding tissues if it has higher glucose uptake and is being imaged with ^{18}F-fluorodeoxyglucose (^{18}F-FDG). The time period between the radiotracer administration and the data acquisition varies depending on the application. It can go from some minutes to some hours or days. As will be explained in detail in Sections 2.3 and 2.4, the acquired data are projections of the volume of interest that are used to estimate the desired tomographic images through a process called *tomographic image reconstruction*. Tomographic images can be either 2D slices or a 3D image of the volume of interest. There exist different reconstruction techniques. The conventional method is called filtered backprojection (FBP). In recent years, more sophisticated techniques, including iterative statistical estimation procedures, have been developed. Maximum-likelihood expectation maximization (ML-EM), and its variation, ordered-subsets ML-EM (OSEM), are examples of the most commonly used image reconstruction techniques.

The last step of the process is the image analysis by the physicians or medical staff. It traditionally consisted of visual inspection and evaluation of the images, but in recent years, computerized analysis has been greatly developed and plays a key role providing supplementary information to the expert.

2.3. ET data acquisition

In the present section we present the basic ideas of planar projection acquisition. The approach is set for SPECT acquisition, since it is the case of interest of this work. However, the PET case is analogous.

Isotope	Half-life ($t_{1/2}$)
^{18}F	110 min
^{82}Rb	1.25 min
^{11}C	20.4 min
^{15}O	124 s
^{99m}Tc	6.02 h
^{201}Tl	73.1 h
^{123}I	13.2 h
^{131}I	8.02 days

Table 2.2: Half-life of some commonly used radioisotopes. From [10].

In ET, data acquisition is done in the form of planar projections by means of a gamma camera. An ideal gamma camera detector can be modeled as a 2D surface, which records the impacting photons. More precisely, for a given detector position, an ideal gamma camera records all photons hitting the detector in that position coming in normal direction to the detector. The camera moves around the object in order to capture photons coming in different directions and thus obtaining different object views (see Figure 2.3). In Section 3.3, we present a description of the gamma camera operation, which will make clear how acquisition is achieved in practice.

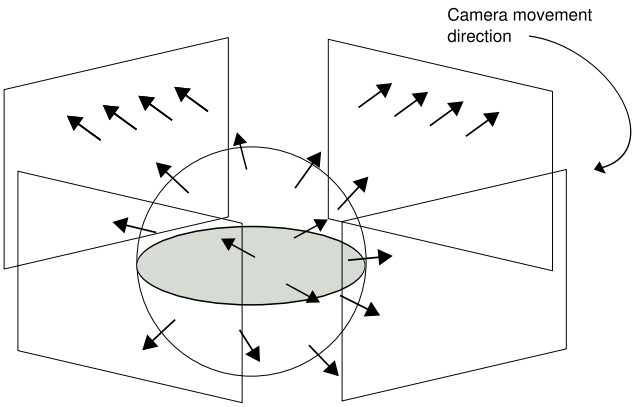

Figure 2.3: ET data acquisition. Photons are emitted in all directions. The camera rotates around the volume capturing photons arriving in normal direction from different perspectives.

We introduce some notation in order to formalize these ideas. We will consider two reference frames. The first one is attached to the volume of interest, described by coordinates (x, y, z). The second one is rotative, described by coordinates (x_r, y_r) with the rotation angle θ, verifying

$$\begin{bmatrix} x \\ y \end{bmatrix} = \begin{bmatrix} \cos\theta & -\sin\theta \\ \sin\theta & \cos\theta \end{bmatrix} \begin{bmatrix} x_r \\ y_r \end{bmatrix}.$$

The second frame of reference can be thought of as attached to the gamma camera, allowed to move around the patient in order to view it from different perspectives. See Figure 2.4 for an illustration of this. Finally, we define function $V(x, y, z)$, representing the radiotracer distribution in the volume of interest. For simplicity, we will consider the 1D projection corresponding to a given $z = z_0$. The 2D projection is obtained with the same procedure repeated for all z positions. This can be thought of as considering only one slice of the volume, the one corresponding to $z = z_0$. The procedure is then extended to all the slices that make up the volume.
The 1D projection $p(x_r, \theta, z = z_0)$ at a given perspective or angle θ, is the parallel projection of $V(x, y, z = z_0)$ along y_r, when viewed at angle θ, i.e.

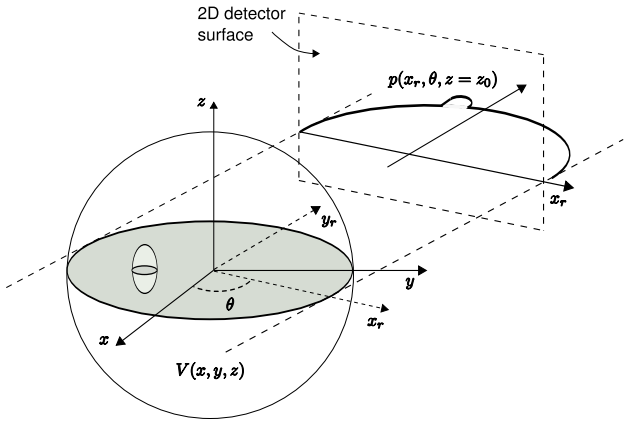

Figure 2.4: ET data acquisition. One slice of the volume of interest, $V(x, y, z = z_0)$, is integrated along direction y_r, for all x_r and for a given projection angle θ. The obtained 1D projection is $p(z_r, \theta, z = z_0)$. The same procedure is repeated for all angles and all slices to scan the complete volume.

$$p(x_r, \theta, z = z_0) = \int_{-\infty}^{+\infty} V(x, y, z = z_0) \mathrm{d}y_r. \tag{2.1}$$

For a given θ, the projection $p(x_r, \theta, z = z_0)$ represents, as a function of position x_r, the integral of the radiotracer distribution function $V(x, y, z = z_0)$ along each normal direction y_r. The set of all projections, for $0 \leq \theta < 2\pi$, as a 2D function of x_r and θ is named **sinogram**. This is because one fixed point (x_0, y_0, z_0), describes a sinusoid $x_r = x_0 \cos\theta + y_0 \sin\theta$ in the (x_r, θ) plane. A sinogram for a general object is the superposition of the sinusoids for all the points in the object. Figure 2.5 shows an example of a slice and its corresponding sinogram. Note the two sinusoids described by the bright sources.

Although this can be considered a kind of 3D imaging (repeating the procedure for each slice), there also exist the fully 3D imaging which we will not describe in detail. For a description of fully 3D imaging we refer the reader to [11]. Tomographic images (2D slices or 3D volume images) are then obtained from these projections. A tomographic pixel, or voxel, represents a measurable parameter at one point in space. On the contrary, a projection pixel represents the result of the integration of that parameter along a line-shaped volume through the object of interest. The estimation of tomographic images from projections is called tomographic reconstruction. The tomographic image reconstruction problem can be formally stated as, given $p(x_r, \theta, z = z_0)$, for all x_r and θ, which is the original function $V(x, y, z = z_0)$? In the presence of statistical noise, the exact solution to this problem is not possible. Various methods have been proposed in order to tackle this problem.

On the other hand, an exact solution can be found for the noise-free case. The most commonly used reconstruction method in that case is called filtered backprojection (FBP). Despite having several disadvantages (e.g. it does not consider the Poisson nature of photon emission neither the acquisition process non-idealities) the FBP method has been widely applied to image reconstruction in clinical imaging. The main reason is its simplicity, leading to an easy implementation and low processing times. In some proposals [12], the FBP reconstruction is combined with low-pass filtering techniques (e.g. Butterworth filters) in order to reduce noise and improve the reconstructed image quality. Obviously, this has the counterpart of the increased blur, caused by the high frequencies attenuation. In Section 2.4 we will present some of the most widely used image reconstruction techniques.

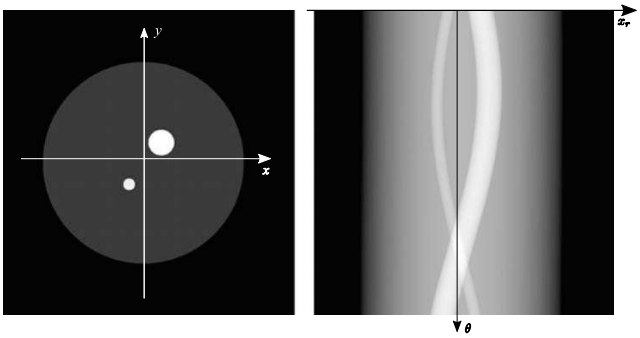

Figure 2.5: **Left:** Slice from the volume of interest. **Right:** Corresponding sinogram. Notice the two sinusoids described in the (x_r, θ) plane by each of the bright circular sources. Picture from [10].

2.4. Reconstruction methods

The image reconstruction problem can be stated as follows: given the set of projections $p(x_r, \theta, z)$, find the original distribution function $V(x, y, z)$. This reconstruction can be performed independently for each slice, in that case the problem would be to find $V(x, y, z = z_0)$, given the projections $p(x_r, \theta, z = z_0)$, for each slice; or fully 3D, including all the available information to reconstruct the whole volume $V(x, y, z)$. In the present work we will only consider the former approach. Reconstruction methods can be classified into two broad classes: analytic and iterative methods. Analytic methods neglect real physical factors, affecting the acquisition process, in an effort to obtain explicit inversion formulas for the reconstruction process. They usually provide solutions which are simple to compute and interpret. The FBP method is an example of this techniques. On the contrary, iterative methods allow to include various realistic factors of the image acquisition process. They are mostly statistical based approaches and obtain, in general, better quality results. The counterpart is that they are computationally expensive and more difficult to interpret. In the following we describe two of the most commonly used reconstruction methods: FBP and ML-EM.

2.4.1. Analytic methods: FBP

The best known example of analytic reconstruction is FBP. Most conventional approaches to image reconstruction are based on this method. FBP is a mathematical technique which assumes an idealized form of the ET images. It models the number of photons traveling in a given direction as the integral line of the tracer distribution along that direction, i.e. the parallel projection introduced in equation (2.1). It ignores effects such as the Poisson nature of emissions, scatter noise, the blur introduced by the camera non-ideal response. In spite of this, reasonable results can be obtained through FBP. In fact, it has been widely used in clinical applications, largely because of its computational simplicity.

In FBP, the sinogram is turned into a tomographic image by means of a method called *backprojection*. Backprojection consists in smearing projection data into the object region along the direction θ in which it was measured. Because the knowledge of where the values came from was lost in the integration with respect to y_r, the best we can do is assign the constant value $p(x_r, \theta, z = z_0)$ along y_r for each x_r, with given θ and z_0 values. Figure 2.6 illustrates the backprojection process for a given direction of a slice image. The same procedure is repeated for all directions θ and the results are added together. For a reasonable number of projection angles, this gives a good interpretation of the original object. Figure 2.7 shows the FBP reconstruction, of the object presented in Figure 2.5, for different number of projection angles. It can be shown [11], that the backprojection method introduces blur in the reconstructed image, with a point-spread function given by $1/r$, with $r = \sqrt{x^2 + y^2}$. Thus, the FBP method includes a filtering stage that

cancels this blurring effect. For this purpose, the projections are pre-processed with a ramp filter before backprojection.

The FBP method is originally developed for the noise-free case. However, it is also applied in the presence of noise, including a smoothing step either applied to the projections (before backprojection) or to the reconstructed 2D image (after backprojection).

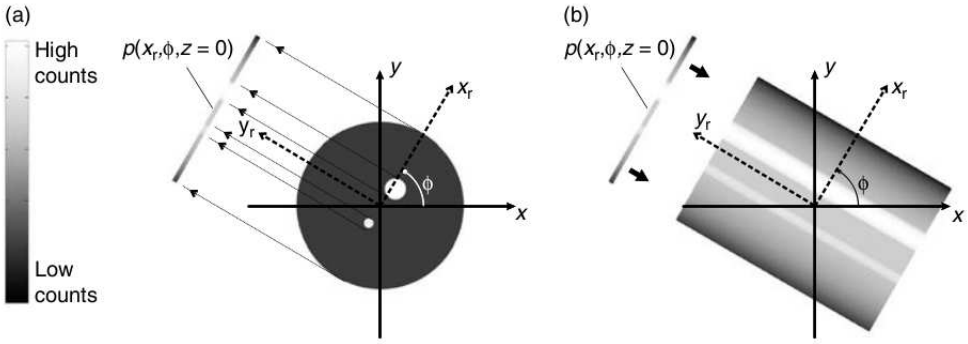

Figure 2.6: Representation of the backprojection process. **Left:** Parallel projection $p(x_r, \phi, z = 0)$ along y_r, for all x_r and a given projection angle $\theta = \phi$. **Right:** The projection $p(x_r, \phi, z = 0)$ is backprojected. Since we have no information about the values at each y_r coordinate, the projection value for each x_r is assigned along the y_r direction. The same procedure is repeated for each angle projection θ and the results are added together. Picture from [10].

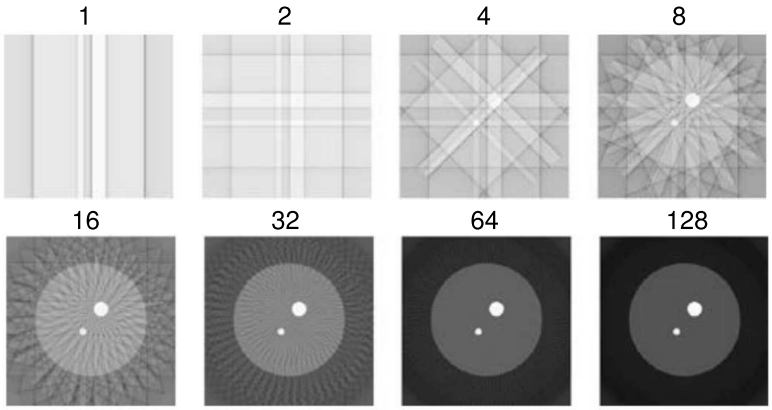

Figure 2.7: FBP reconstruction of the object presented in Figure 2.6 for different number of projection angles. Note how reconstruction quality increases with increasing number of projections. Picture from [10].

2.4.2. Iterative methods: ML-EM

In 1982, A. Shepp and Y. Vardi proposed a method [13] for ET reconstruction based on the idea of maximizing the probability $p(\mathbf{G}|V)$ of observing the actual detector counts $\mathbf{G}$ over all possible emission densities V. Unlike previous methods, they give an accurate mathematical model for ET, which takes into account the Poisson nature of the emission process and the non-idealities of the acquisition. Based on this model, they give a formula to compute the likelihood function $p(\mathbf{G}|V)$, and using special properties of the Poisson distribution they show that the log-likelihood function l is a concave function of V. Given that l is a concave function of V, any local maxima has to be the global. Thus, the authors propose an EM based iterative scheme to find these maxima. This

scheme gives a sequence of estimates $\hat{V}^0, \hat{V}^1, \ldots$ which converges to a global maximum estimator $\hat{V}^\infty$. Using an EM approach to find the V estimate ensures that in each step, the new estimate $\hat{V}^{new}$ is an improvement of the previous estimate $\hat{V}^{old}$

$$l(\hat{V}^{new}) \geq l(\hat{V}^{old}),$$

where the equality is reached if and only if $l(\hat{V}^{old}) = \max_V l(V)$. They show, by simulation, that the proposed method decreases the statistical noise artifacts compared to conventional convolution backprojection algorithms without introducing excessive smoothing. Despite having very good quality reconstruction results, the method was not widely incorporated for clinical use due to its slow convergence and high computational cost. It was not until 1994, when Hudson et al. [14] proposed a variation of the method, that it became widely applied in clinical use until today. This variation is known as OSEM, and accelerates the algorithm convergence by dividing input data into subsets and applying an iteration of the original algorithm to each subset. In the following we present a description of the original ML-EM method and its variation OSEM.

ML-EM: General description

We start by introducing some notation. The unknown object is represented by a set of N volume elements, each of which have constant value V_n, $n = 1, \ldots, N$. This value represents the **average number** of gamma-rays emitted from that volume element during the study period T and is directly related to the radiotracer concentration in that volume element. The complete volume is represented by the $N \times 1$ column vector V, with V_n its n-th component.

Let a Poisson distributed number $\mathbf{V}_n$, with expected value V_n, be generated independently in each voxel $n = 1, \ldots, N$. $\mathbf{V}_n$ represents the number of photons emitted in voxel n. In Section 3.2.4 we will show that these are reasonable hypotheses to model photon emission. The $N \times 1$ column vector $\mathbf{V}$, is the vector of components $\mathbf{V}_n$, $n = 1, \ldots, N$.

Sinogram data is represented by the $M \times 1$ column vector $\mathbf{G}$, with $\mathbf{G}_m$ its m-th component. If we discretize de 2D detector surface in D detector elements, index $m = 1, \ldots, M$ represents all possible combinations of projection angle and detector element. $\mathbf{G}_m$ represents the number of detected photons in data bin m. As will be shown in Section 5.1.1, for a given V, $\mathbf{G}$ components can be modeled as independent Poisson random variables. Note that V is deterministic, while $\mathbf{V}$ and $\mathbf{G}$ are Poisson distributed random variables.

Proposed model Suppose that each emission in voxel n is detected in detector m with known probability

$$h(m, n) = P(\text{detected in } m | \text{emitted in } n),$$

so that $h(m, n) \geq 0$. Thus, the probability of an emission in n being detected at all is given by

$$h(n) = \sum_{m=1}^{M} h(m, n) \leq 1. \tag{2.2}$$

Inequality in (2.2) shows that some photons might not be detected at all. The transition matrix $h(m, n)$ is assumed to be known exactly from the detector array geometry and other characteristics of the system, described later in this Section. After each emission moves to some detector element, or is missed and undetected, there is a known total number $\mathbf{G}_m$ of counts in each detector $m = 1, \ldots, M$. The probability $P(\mathbf{G}|V)$ of observing $\mathbf{G}_m$, $m = 1, \ldots, M$ is a function $L(V)$ of the unknown rate V. Thus, we want to choose an estimate $\hat{V}$ of V to maximize $L(V)$. Such an estimate is called a **maximum likelihood** estimate of V given $\mathbf{G}$. Finally, the **target** is to propose an expression for $L(V)$ and find an estimate $\hat{V}$ of $\mathbf{V}$ which maximizes $L(V)$ given $\mathbf{G}$.

Before proceeding with our pose of finding $L(V)$ and the maximum estimator $\hat{V}^{\infty}$, it is important to notice that Shepp et al. show that, without loss of generality, it can be assumed that equality in (2.2) holds. In that case, $p(n,m)$ represents the conditional probability that a **detected** photon, emitted in voxel n, is detected in detector m. This is equivalent to thinking of V as the density of **emitted counts which are detected**. They make that assumption along their analysis, which is consistent with a particular property of the algorithm (that we will see later): the total number of detected counts is automatically preserved in the estimate $\hat{V}$, i.e.

$$\sum_{n=1}^{N} \hat{V}_n = \sum_{m=1}^{M} \mathbf{G}_m,$$

This assumption should simplify the task of finding $h(m,n)$, since we do not need to include information about those photons that go undetected.
It is also interesting to notice that the previous approach is an approximate mathematical model of the physics involved. Some of its main assumptions are:

- It exists an ambiguity in the discretization of boxes n and how $h(m,n)$ is determined.
- Scattered count errors should be eliminated in the physical measurement procedure by energy discrimination of scattered counts. This proposal ignores these problems and assumes the only source of difficulty is in the stochastic fluctuations (Poisson nature) of the counting statistics $\mathbf{G}$.

The likelihood function $L(V)$ The count in detector m, $\mathbf{G}_m$, is made up from the contribution of the independent emissions of voxels $n = 1, \ldots, N$

$$\mathbf{G}_m = \sum_{n=1}^{N} \mathbf{G}_{n,m}, \tag{2.3}$$

with $\mathbf{G}_{n,m}$ the emissions from voxel n detected in m. The variable $\mathbf{G}_{n,m}$ is a binomial selection of the process $\mathbf{V}_n$ according to the probability $h(m,n)$, thus according to the Binomial Selection Theorem 5.1.1 (c.f. Section 5.1.2) we have

$$G_{n,m} = \mathrm{E}(\mathbf{G}_{n,m}) = V_n h(m,n). \tag{2.4}$$

Now from (2.3) and (2.4) we can find the expected value of $\mathbf{G}_m$ as

$$G_m = \mathrm{E}(\mathbf{G}_m) = \sum_{n=1}^{N} \mathrm{E}(\mathbf{G}_{n,m}) = \sum_{n=1}^{N} V_n h(m,n). \tag{2.5}$$

As mentioned before, the variables $\{\mathbf{G}_m\}_{m=1}^{M}$ are independent Poisson random variables. Thus, the likelihood function $L(V)$ is given by

$$L(V) = P(\mathbf{G} = k|V) = \prod_{m=1}^{M} e^{-G_m} \frac{G_m^{k_m}}{k_m!},$$

where the dependence of V is given by Equation (2.5). Then, using properties of the Poisson model, it can be shown [13] that the log-likelihood $l(V) = \ln L(V)$, is a concave function of V.

Maximizing l via Expectation Maximization Now we describe the iterative algorithm proposed by Shepp et al., based on the EM algorithm [15], to maximize the log-likelihood function l. Using an EM approach to find the V estimate ensures that in each step, the new estimate $\hat{V}^{new}$ is an improvement of the previous estimate $\hat{V}^{old}$

$$l(\hat{V}^{new}) \geq l(\hat{V}^{old}),$$

where the equality is reached if and only if $l(\hat{V}^{old}) = \max_V l(V)$. The concavity of $l(V)$ ensures that all maxima are global maxima, thus the EM based iteration scheme gives a sequence $\hat{V}^0, \hat{V}^1, \ldots$ which converges to a global maximum estimator $\hat{V}^\infty$.

The first step to pose the EM iterative scheme is to notice that if we believe that $\hat{V}^{old}$ is the true V, we should estimate the unobserved number of emissions in voxel n, $\hat{\mathbf{V}}_n$, as

$$\hat{\mathbf{V}}_n = \mathrm{E}(\mathbf{V}_n | \hat{V}^{old}, \mathbf{G}),$$

this is the **expectation step**. Then, if $\hat{\mathbf{V}}_n$ is our estimate for the emission count in voxel n we should, in order to be consistent, estimate the emission density V_n by $\hat{\mathbf{V}}_n$ (because $\hat{\mathbf{V}}_n$ is the maximum likelihood estimate of V_n if indeed $\hat{\mathbf{V}}_n$ is the emission count in voxel n); this is the **maximization step**. This gives the iterative scheme,

$$\hat{V}_n^{new} = \mathrm{E}(\mathbf{V}_n | \hat{V}^{old}, \mathbf{G}) \quad n = 1, \ldots, N. \tag{2.6}$$

It can be shown [13] that

$$\mathrm{E}(\mathbf{V}_n | \hat{V}^{old}, \mathbf{G}) = \hat{V}_n^{old} \sum_{m=1}^{M} \frac{\mathbf{G}_m h(m,n)}{\sum_{n'=1}^{N} \hat{V}_{n'}^{old} h(n',m)}. \tag{2.7}$$

Finally, the EM iterative scheme to find the maximum likelihood estimator $\hat{V}^\infty$ is:

Start with an initial guess V_n^0 (usually uniform constant) satisfying $V_n^0 > 0$, $n = 1, \ldots, N$. Then, at each iteration, $\hat{V}^{new}$ is updated according to

$$\hat{V}_n^{new} = \hat{V}_n^{old} \sum_{m=1}^{M} \frac{\mathbf{G}_m h(m,n)}{\sum_{n'=1}^{N} \hat{V}_{n'}^{old} h(n',m)}. \tag{2.8}$$

Because of being an EM algorithm, we have that if $\hat{V}_n^{new} \neq \hat{V}_n^{old}$, then $l(\hat{V}_n^{new}) > l(\hat{V}_n^{old})$, i.e. the algorithm is monotone. The likelihood increases in each step of (2.8), unless $\hat{V}_n^{new} = \hat{V}_n^{old}$, in which case convergence is achieved. As mentioned before, it is interesting to notice that the following equality is fullfilled [13]

$$\sum_{n=1}^{N} \hat{V}_n^{new} = \sum_{m=1}^{M} \mathbf{G}_m \quad \text{and} \quad \hat{V}_n^{new} \geq 0.$$

This ensures that the total number of counts is automatically preserved in the estimate $\hat{V}^{new}$ and $\hat{V}^{new} \geq 0$ at each stage. This condition is highly useful from the practical point of view but is not verified by most of the reconstructions methods.

In the following we will present a more intuitive explanation for (2.8), analyzing the role of each of the formula components. We divide (2.8) into four parts, each representing a stage of the estimation process. The four steps complete one iteration, which is repeated until convergence.

Projection This step includes the passage from the 3D volume to the 2D projections (as those obtained with the gamma camera). Here, the 3D volume is represented by the actual estimate $\hat{V}^{old}$ of V and the projections are represented by the $M \times 1$ vector G'. For each projection component m, the projection estimate G'_m is given by

$$G'_m = \sum_{n=1}^{N} \hat{V}_n^{old} h(m,n), \tag{2.9}$$

where $h(m,n)$ was previously defined and can be thought of as the sensitivity of detector m to volume V. $h(m,n)$ will be non-zero only for those voxels contributing to detector m.

Correction Image The previously found projections are then compared to those actually acquired by the gamma camera **G**. This is done dividing **G** by G' in a pixel by pixel basis. This way we obtain the correction images, represented by the $M \times 1$ vector C, as

$$C_m = \frac{\mathbf{G}_m}{G'_m}.$$

Backprojection The next step consists in backprojecting the correction images to obtain a volume of scaling factors, which will then be used to adjust the current estimation of volume V. The backprojection operation was previously presented in the description of the FBP algorithm. We represent the volume of scaling factors by the $N \times 1$ vector F.

$$F_n = \sum_{m=1}^{M} C_m h(m,n).$$

Volume Update Finally, the current estimation $\hat{V}^{old}$ is updated according to the volume correction factors given by F, yielding $\hat{V}^{new}$. This is done multiplying volumes $\hat{V}^{old}$ and F in a voxel by voxel basis.

$$\hat{V}_n^{new} = \hat{V}_n^{old} F_n.$$

Choice of $h(m,n)$ values

The probabilities $h(m,n)$, as components of a $M \times N$ matrix H, are known as *projection matrix*. This is because each value $p(n,m)$ represents the probability of a photon emitted in voxel n being detected in detector m, i.e. $h(m,n)$ can be thought of as the sensitivity of detector m to voxel n. Equation (2.9), from the **Projection** stage of the ML-EM algorithm, can be written in matrix form as

$$G' = H\hat{V}^{old},$$

which gives an explicit form of matrix H as a projection matrix of the 3D volume $\hat{V}^{old}$ to the 2D projections G'. Now, how are the component values of H defined? Firstly, matrix H must reflect the geometry of the gamma camera acquisition process, i.e. for each detector m, its value should be close to that of the parallel projection of the volume of interest, defined by (2.1). The distance from this ideal value will be given by the inclusion of different effects as the non-ideal camera response, including collimator and detector non-idealities, and the attenuation effects. The collimator non ideal response is usually modeled as a Gaussian blur, and includes effects as the septal penetration and the non infinitesimal bore radio. Non-ideal detector response is also modeled as a Gaussian blur and includes effects as the crystal quantum efficiency and the uncertainty on the photon impact location. Attenuation is usually modeled as an exponential decay along the path normal to the camera from a given detector element. All these non-ideal effects will be explained in more detail in sections 3.2.5 and 3.3. The inclusion of matrix H in the reconstruction method allows to consider various non-idealities of the acquisition process, which was not possible in the FBP reconstruction. It is interesting to mention that Shepp et al. found [13] that the reconstruction does not depend too critically on the choice of H assuming that it is reasonable.

2.4.3. OSEM

As mentioned before, despite leading to good quality reconstruction results, the ML-EM algorithm has a slow convergence rate. This motivated Hudson et al., to propose a variation of the ML-EM algorithm, called OSEM [14]. In the ML-EM algorithm, all projection data **G** is used to obtain the scaling factors F used to update the volume estimation. With OSEM, the projection data is divided into subsets and an iteration of the ML-EM algorithm is applied to each of the

subsets in turn. The resulting reconstruction becomes the current estimate for use with the next subset. Using subsets allows to calculate the scaling factors at a smaller cost. The convergence rate is found to be increased by a factor proportional to the number of subsets.

Continuing with the notation introduced for ML-EM, $\hat{V}^0$ is the initial estimate of V (e.g. uniform) and $\hat{V}^j$ denotes the estimate of V after iteration j. Let $S_1, \ldots, S_Q$ denote the chosen projection subsets. The OSEM algorithm can then be summarized as follows:

1. $j = 0$, $\hat{V}^j$ initialized verifying $\hat{V}^j > 0$
2. Repeat until convergence of $\hat{V}^j$
   a) $x^1 = \hat{V}^j$, $j = j + 1$
   b) For subsets $q = 1, \ldots, Q$
      1) **Projection:** Calculate
      $$G'^q_m = \sum_{n=1}^{N} x^q_n p(n, m),$$
      for detector elements m in subset S_q.

      Notice that the projection values G'^q_m are calculated using the updated value of x^q, which includes the corrections introduced from the iterations on the subsets $S_1, \ldots, S_{q-1}$.
      2) **Correction, backprojection and update:** Calculate
      $$x^{q+1}_n = x^q_n \sum_{m \in S_q} \frac{\mathbf{G}_m p(n, m)}{G'^q_m} / \sum_{m \in S_q} p(n, m),$$
      for voxels $n = 1, \ldots, N$. This step updates the volume estimate x^{q+1} with the scale factors obtained from detector elements m in subset S_q.
   c) $\hat{V}^j = x^{q+1}$. The volume estimate $\hat{V}^j$ is updated as the estimate x^{q+1}, obtained with the corrections from all subsets in turns.

Each iteration of item (b) performs one iteration of the ML-EM algorithm with the projection data restricted to a subset of the complete data set $\mathbf{G}$. This can also be written as the standard ML-EM algorithm with the projection matrix H substituted by the subset dependent projection matrix H_q

$$[H_q]_{mn} = \begin{cases} (H)_{mn} & q \in S_q \\ 0 & \text{otherwise} \end{cases}$$

An OSEM iteration is a single pass through all the subsets. With mutually exclusive and exhaustive subsets, one OSEM iteration has a similar computation time to one standard ML-EM iteration. Despite this, OSEM usually achieves higher reconstruction quality for the same computation time.

Subsets definition and order

In SPECT, subsets correspond naturally to groups of projections, e.g. for 64 projection angles in the range 0-360 degrees, we can choose 8 subsets of 8 projections each, uniformly distributed along the acquisition angle range. This way, each subset has varied views of the volume of interest. In that case, an OSEM sub-iteration will update the volume with the information obtained from the detector elements corresponding to 8 of the 64 projections. Examples of subset elections are:

non-overlapping subsets With q subsets each of p detectors per projection, sets $S_1 = 1, \ldots, p, S_2 = p + 1, \ldots, 2p, \ldots, S_q = (q - 1)p + 1, \ldots, qp$. Data used in each sub-iteration (with a given subset) includes the given p detectors of all projections.

cumulative subsets With $S_1 = 1, \ldots, p, S_2 = 1, \ldots, 2p, \ldots, S_q = 1, \ldots, qp$. Data used in each sub-iteration includes the detectors defined for each subset, of all projections. The division is cumulative since data already used in iteration $(q-1)$ is used again to compute the i-th estimation.

standard ML-EM Employing a single subset including all projection data $S_1 = 1, \ldots, pq$.

The order in which subsets are processed is arbitrary. However, it may be advantageous to introduce substantial new information, e.g. corresponding to the direction of greatest variability in the volume, at first.

Some comments...

It was experimentally verified [14] that the execution speed is significantly increased for OSEM compared to the standard ML-EM. To achieve a reconstruction with a given maximum level of error, the number of iterations is inversely proportional to the number of subsets. Also, it was seen that as data is divided into more subsets, accelerated reduction of error is increased up to a critical number of iterations, beyond which the noise artifacts of the ML-EM solution are magnified by OSEM. This well known noise artifact present in ML-EM estimations, motivates its early stopping before convergence is achieved. The same mean square error is obtainable with OSEM with less iterations instead of stopping ML-EM before convergence.

Except for noise-free data, OSEM converges to a non ML-EM solution. Authors do not show whether the algorithm converges or not. Instead they have empirically seen that OSEM follows a cycle between different limiting images, depending on the last projection processed. For real scale applications, these limiting images appear to be very similar, and for a moderate number of subsets, indistinguishable. Computational experiences show that OSEM increases the likelihood function at each iteration.

The most appropriate number of subsets depends on the attenuation density, the subset balance and the level of noise in the projection data. With no attenuation, the use of individual projections as subsets is inefficient. In that case, opposite projections provide estimates of the same regions and should be included together in the same subset. Subset imbalance (variability in the probability of a voxel emission being detected in different subsets) is greater for individual projections used as subsets, thus balance is improved as the number of subsets is reduced. Also, with high levels of statistical noise (low counts images) it is preferable to use smaller number of subsets.

Chapter 3

SPECT

This chapter is devoted to present general aspects of the SPECT nuclear imaging technique. In Section 3.1 we define what SPECT is, its applications and functioning modes. Section 3.2, describes basic concepts related to the physical phenomena causing the radioactive decays and the corresponding SPECT image formation process. A derivation of the well-known Poisson model to describe the nuclear radioactive decay is also presented. Next, the interactions of gamma-photons in matter are analyzed, since these are what really enable SPECT image formation. Section 3.3 describes the operation of a type of gamma cameras, known as Anger cameras, which are nowadays widely used in clinical applications.

3.1. General principles

As introduced in Section 2.1, ET comprises two main techniques: single-photon emission computed tomography (SPECT) and positron emission tomography (PET). The difference between SPECT and PET lies in the radioisotope used to label the tracer, and therefore in the applications each of them encounters. See Table 2.1 for a list of the principal clinical applications of each technique. Radioisotopes used in SPECT studies are single-photon emitters, i.e. one gamma-photon is emitted with each radioactive decay. For PET studies, the radioisotopes are positron emitters which, upon decay, emit a positron. When this positron encounters an electron in the surrounding medium, they mutually annihilate, resulting in the emission of two gamma-photons in opposite directions. The difference between the number of photons emitted in each case, changes the logic of detection and the hardware used to detect and localize them.

SPECT, as an example of ET imaging, is a diagnosis nuclear imaging technique that uses gamma-ray emissions to describe the spatial or spatial-temporal distribution of physiological processes. A radioactive labeled tracer is administered to the patient and the emitted gamma-photons are recorded to describe the properties of the physiological process of interest. In routine nuclear medicine imaging, SPECT studies are performed using one or more rotating gamma cameras, which acquire projections of the radionuclide distribution. Then, image reconstruction is performed to obtain the tomographic study from projections.

SPECT studies can be performed in two modes: planar or tomographic. Planar imaging consists in taking a projection of the radionuclide distribution, i.e. recording the distribution of interest from a single view-point. Tomographic imaging implies a volumetric, or in slices, description of the radiotracer distribution. The latter is obtained by the image reconstruction process from several planar projections. Both modes are routinely used in nuclear medicine clinics.

The SPECT imaging technique can work in two modes, transmission or emission tomography. Emission tomography shows the radiotracer distribution within the body, the emissions coming

from inside the body are detected. Transmission tomography show the attenuation coefficient distribution of the body, the emissions coming from an exterior source and traversing the body are detected. The latter technique is typically an auxiliary step in emission SPECT, since it is used to estimate the attenuation map of the body which is posteriorly used to correct the emission study attenuation.
In the following we will analyze in detail the emission study since it is the principal application of SPECT tomography and the subject of interest in the present work.

3.2. The physics of SPECT

Where do the gamma-ray emissions detected in SPECT emission tomography come from? In the following paragraphs we will briefly summarize the main ideas related to nuclear emissions in SPECT imaging in order to better understand the fundamentals of this nuclear imaging technique. This section is based on [16].

3.2.1. Basic definitions: nuclear constituents, forces and the binding energy

The atomic nucleus is made up of neutrons and protons, also known as nucleons. The proton has one unit of fundamental electronic charge while the neutron is electronically neutral. The size and shape of the nucleus depends on the number of neutrons (N) and protons (Z), their energy states, and the angular momentum of the nucleus. The total number of nucleons in the nucleus (A) is called the mass number. Atoms with identical chemical properties (same Z) but different masses (different A) are called isotopes [16].

The three fundamental forces playing important roles within the nucleus are: the *electromagnetic*, the *strong* and the *weak* nuclear forces. The forth fundamental force, the *gravity*, has negligible effects within the nucleus. The *electromagnetic* interaction is the cause of repulsive Coulomb forces among protons (since neutrons are electrically neutral they do not interact electrically). These electrostatic repulsion forces are immense. The *strong* nuclear force is the responsible of holding the nucleons together in spite of the electrostatic repulsive forces. Is an attractive interaction between nucleons irrespective of their electronic charge. It is typically a factor of 100 times stronger than the electromagnetic interactions among the protons. The *weak* nuclear force is the cause of certain types of radioactive decay (e.g. spontaneous nuclear β decay). Is typically 10^{-3} or 10^{-4} times weaker than the electromagnetic interaction.

The *binding energy* is the energy needed to overcome the forces holding the atomic constituents together and separate it into its components: neutrons, protons and orbital electrons.

3.2.2. Nuclear energy states

The *shell* model is one of the most successful models describing the nucleons energy states within a nucleus [16]. In this model nucleons move in orbits about on another and the types of motion are quantized, i.e. described by discrete nuclear quantum parameters. This way, each nucleon in the nucleus has a unique discrete set of allowed energy states, called *energy levels*. Excited energy states, where some nucleons of the nucleus are in elevated energy states, usually last extremely short times before decaying to a different lower energy state. Those states that last relatively long time before decaying are called *metastable* states.

3.2.3. Nuclear de-excitation and stability

In nature, systems tend to evolve from higher to lower energy levels. As mentioned before, higher energy states usually exist for extremely short periods. These nuclear transitions from higher to lower energy states have as a result the emission of electromagnetic radiation. This is called **radioactive decay** and nuclides undergoing such transformations are called **radionuclides**. Besides, the initial unstable nucleus is called the *parent* and the final, more stable nucleus, is termed the *daughter*. The energy resulting from the nucleons reconfiguration can be released in two ways: in the form of *gamma-ray* photons or as *internal conversion*. *Gamma-rays* or *gamma-photons* are electromagnetic radiation of high frequency. They are the most commonly used nuclear emissions in nuclear imaging. Gamma-ray emission from short-lived nuclear de-excitation is not of use for imaging since it lasts extremely short times. On the contrary, metastable radionuclides are used because of their relatively long lifetimes. Those having lifetimes between a few minutes and a few months can be used for in vivo imaging. For example, the ^{99m}Tc, is highly used in SPECT imaging since its half-life is 6h, it delivers a relatively low radiation dose and it can be used to label a great variety of imaging materials. Also its decay leads to the known 140 keV gamma-photon emission, favorable to use with the gamma-ray cameras. On the other hand, in the *internal conversion*, the nuclear energy is transferred directly to an atomic electron (usually inner shell). These electrons are rapidly absorbed in tissue and so that not directly useful in radioactive imaging.

3.2.4. Nuclear decay statistical model

In the following we present a derivation of the Poisson model to describe the radioactive nuclear decay process.

Some basics

If an event occurs with probability p, the probability that it occurs n times out of N trials follows the **binomial** law

$$P(n,N) = \frac{N!}{(N-n)!n!}p^n(1-p)^{N-n}, \tag{3.1}$$

with mean value Np and variance $Np(1-p)$.
If N is large and p is close to zero, so that $(1-p)$ is close to 1, the event is called a *rare event* and the binomial distribution is closely approximated by the **Poisson** distribution

$$P(n,N) = \frac{(Np)^n e^{-Np}}{n!} \tag{3.2}$$

with mean and variance equal to Np.

Back to the radioactive decay

The radioactive decay is a stochastic process, it is impossible to predict when a decay will occur. However, given a large number of identical nuclei, the decay rate can be predicted. Given N_0 identical parent nuclei present at time $t = 0$, at time $t = T$, the number N most probably surviving is

$$N = N_0 e^{-\lambda T},$$

where λ is the *radioactive decay constant*, which verifies $\lambda = \frac{\ln(2)}{t_{1/2}}$, with $t_{1/2}$ the isotope radioactive half-life. This exponential decay law is given by the fact that, on average, a constant fraction of

radioactive atoms disappears in a given constant time interval. On the other hand, we can find the number of expected decays as

$$\begin{aligned} D &= N_0 - N \\ &= N_0 - N_0 e^{-\lambda T} \\ &= N_0(1 - e^{-\lambda T}). \end{aligned}$$

Thus, given N_0 identical parent nuclei at time $t = 0$, the probability of any of them suffering a decay in the time interval $(0, T)$ is

$$p = \frac{D}{N_0} = 1 - e^{-\lambda T}. \tag{3.3}$$

We can model the observation of the decaying nuclei during the time period $(0, T)$ as a binomial process [17]. For this purpose, we repeat an experiment N_0 times and find the probability that n of them result successful. Each experiment concerns on whether a particular nucleus suffers a decay or not. The probability of success is thus p, the probability of a nuclei suffering a decay in the time interval $(0, T)$. Thus, equation 3.1 represents the probability of having n decays in $(0, T)$, from $N = N_0$ original parent nuclei. Now that we have modeled the observation of nuclei decay as a binomial process, we ask the question whether the Poisson approximation is valid in this case. The Poisson approximation of the binomial distribution is valid if p is close to zero and N_0 is large (so that $N_0 p$ is finite). We analyze the first condition expanding the term $e^{-\lambda T}$ in equation (3.3)

$$p = 1 - \left(1 - \lambda T + \frac{(\lambda T)^2}{2} + \sigma(\lambda T)\right).$$

Thus we have $p \simeq 0$ if $\lambda T << 1$, so that second order and higher terms can be neglected in the expansion of $e^{-\lambda T}$. This condition ($\lambda T << 1$) is almost always satisfied in real ET studies. For example, for an SPECT study using ^{99m}Tc, the acquisition of each projection lasts about $25s$ so that $\lambda T = \frac{\ln(2)}{6.02h} 25s = 0.001$. Moreover, the second condition fundamentally implies $n \ll N_0$, which is always verified in practice. Therefore the Poisson approximation (3.2) is a reasonable approximation for the nuclear decay process. In the following we will show that $n \ll N_0$ is also the condition for the probability of a nucleus decays in an infinitesimal interval $t + \mathrm{d}t$ to be independent of n.

Let us consider a source with N_0 parent nuclei at time $t = 0$. If n of them decay during the time interval $(0, T)$, the probability that k of the remaining nuclei decay in time period $(T, T + \mathrm{d}t)$ is

$$P(k, T + \mathrm{d}t) = \frac{(N_1)!}{(N_1 - k)!k!} p^k (1 - p)^{N_1 - k}, \tag{3.4}$$

where λ is the decay constant, $N_1 = N_0 - n$ and $p = (1 - e^{-\lambda \mathrm{d}t})$ is the probability that a nucleus decays in the time interval $(T, T + \mathrm{d}t)$[1]. Here we model, as before, the observation of the decay process, in period $(T, T + \mathrm{d}t)$, as a binomial process. The probability of success -probability of decay- is p and the initial total number of parent nuclei is N_1. Note that setting the initial number of parent nuclei N_1 as: $N_1 = N_0 - n$, includes the condition that n of the nuclei decay during the interval $(0, T)$. Hence, from (3.4) and taking $k = 1$, we can find $P(1, T + \mathrm{d}t)$, the probability of

[1] In order to simplify notation, and considering that it should always be clear from context, we do not make explicit the initial time instant in the probability expressions, i.e. $P(n, T + \mathrm{d}t) = P(n, (T, T + \mathrm{d}t))$.

having 1 decay in $(T, T + \mathrm{d}t)$ after n previous decays in $(0, T)$.

$$
\begin{aligned}
P(1, T + \mathrm{d}t) &= \frac{(N_1)!}{(N_1 - 1)!1!} p^1 (1 - p)^{N_1 - 1} && (3.5)\\
&= N_1 p (1 - p)^{N_1 - 1} \\
&= N_1 (1 - e^{-\lambda \mathrm{d}t}) e^{-\lambda \mathrm{d}t (N_1 - 1)} \\
&\simeq N_1 \lambda \mathrm{d}t (1 - \lambda \mathrm{d}t (N_1 - 1)) \\
&\simeq N_1 \lambda \mathrm{d}t \\
&\simeq (N_0 - n) \lambda \mathrm{d}t \\
&\simeq N_0 \lambda \mathrm{d}t, && (3.6)\\
& && (3.7)
\end{aligned}
$$

where we have neglected second and higher order terms of the exponential expansion considering $\mathrm{d}t$ infinitesimal. Therefore, if $n \ll N_0$, the probability of a photon decay in an infinitesimal interval $\mathrm{d}t$, is independent of the previous n decays.

3.2.5. Interactions of gamma-photons in matter

We have seen that unstable nuclei release energy in the form of photons or other particles. In particular, we found that the emitted gamma-photons are very useful for imaging purposes. However, these emissions are too high in energy and too small in size to be seen by the naked eye. Therefore a detection procedure is needed in order to realize the presence of these emissions. In fact, we observe their existence and estimate their energy only through the effects they produce in matter. These effects are the result of the various forces and interactions that nuclear emissions experience when they confront the atoms and molecules of the matter they traverse. Such processes are the basis of radioactive radiation detection and define the efficiency and sensitivity of detectors. The counterpart is that these interactions may interfere with the measurement, since they may disturb the characteristics of radiation before detection. This can be caused, for example, by deflection, absorption or loss of radiation energy before detection is accomplished. Interactions depend on the type of radiation, its energy, and the material being traversed. For the relatively low energies of interest in nuclear imaging, the most common interactions are electromagnetic in nature, involving the atom and nucleus as a whole and also the atomic electrons.

Since photons carry electromagnetic field, they will interact with electric charge. Besides, for the energy levels of interest in nuclear imaging, the most frequent interactions are with individual atomic electrons. The two main interactions among these are the **Compton effect** and the **photoelectric effect**.

Compton effect

If the incident photon energy and momentum are, respectively, much larger than the binding energy and momentum of the struck electron, the latter can be considered, for calculation purposes, as approximately free or loosely bound and at rest. Because the photon is massless and the electron is not, for energy and momentum conservation, the photon cannot transfer all its energy and be absorbed by a loosely bound electron at rest. Therefore, this interaction results in a deviation or **scatter** of the photon and a reduction of its energy. Such an interaction between a high-energy photon (in our case a gamma-photon) and a loosely bound electron is termed **Compton scatter**.

Photoelectric effect

Unlike the previous case, a gamma-ray can transfer all its energy to a bound electron, since the atom can absorb part of the recoil momentum allowing both, energy and momentum, to be

conserved. The result of this interaction is the ejection of the electron, known as photoelectron, and the complete absorption and disappearance of the incident photon. This process is known as photoelectric effect.

Attenuation

A beam of photons traversing matter is degraded in intensity (number of photons forming the beam) since, along its path, photons may be removed from the beam either by deviation (Compton scatter) or absorption (photoelectric effect). However, those that remain part of the beam, i.e. do not suffer interactions with matter, retain their full energy. This intensity reduction phenomenon is known as attenuation. Together with other effects, is one of the image quality degradation causes.
The attenuation for a narrow photon beam in uniform matter follows an exponential law with the penetration distance x

$$I(x) = I_0 e^{-\mu x},$$

where $I(x)$ is the beam intensity at penetration distance x, I_0 is the non-attenuated incident beam and μ is the attenuation coefficient. The μ value is related to the density and atomic number of the absorbing material and the energy of the incoming photons.

Exploiting interactions for detection

As mentioned before, the way of detecting photons is by their interaction with matter, in particular, with the detector. A photon will be detected when it impacts the detector and interacts with it, either transferring all its energy (photoelectric absorption) or part of it (Compton scatter). The total amount of energy deposited and recorded in the detector represents the energy of the incoming photons. The absorbed energy follows different paths depending on the detector characteristics. For example, for scintillator detectors, the absorbed energy produces either electron-holes pairs if the scintillator material is inorganic crystal or excitation of molecular valence electrons if it is an organic compound. The excitation produced with the absorption of the photon energy will generate the energy, timing and positioning information necessary for imaging. See Section 3.3.3 for more details about the detection process and the evolution of the absorbed energy.

3.3. Gamma cameras

In the present section we will describe the principal characteristics and functioning scheme of the gamma cameras. We are interested in knowing their operation in order to better understand the image formation process, the characteristics of the obtained images and the different aspects concerning image quality. A gamma camera is a camera capable of capturing gamma-photons. Different types of gamma cameras have been developed over the years, usually with a common basic modular structure and varying the characteristics of certain modules. In the present work we will focus on a particular type of gamma camera, known as the Anger camera, since it is the most widely used camera in clinical applications. However, many general concepts are still valid for most cameras and can be directly extended. This section is based on [18].

3.3.1. The Anger camera

The Anger camera was originally proposed by Hal Anger, a scientist at the University of California at Berkeley, in 1958. He developed a device capable of imaging gamma emissions. Despite many innovations have been introduced since then, the basic functioning principles remain the same in today's most commonly used clinical gamma cameras. For this reason they are still called Anger cameras. In the following we describe the basic operation of the Anger like cameras.

Figure 3.1 presents a sketch of an Anger camera showing its principal components. We can summarize them as: the collimator, the scintillator crystal, light guides, photomultiplier tubes (PMT), energy discrimination and positioning electronics and the display of the acquired data. The collimator works as a photon direction selector, since it allows photons coming in certain directions to go through and absorbs the others. The selected directions are defined by its bores. Those photons that successfully traverse the collimator reach the scintillator crystal. A fraction of them will interact with the crystal and the rest will pass through without interacting. When interacting with the crystal, the photon deposits part or all of its energy, generating multiple light photons. These light photons propagate through the crystal and light guides to an array of PMTs. The PMTs are sensitive high-voltage devices that produce measurable electric current from as little as a single light photon. Each PMT outputs a current proportional to the number of light photons reaching it. Since the light output from the scintillator crystal is spatially broad, several PMTs in the array are reached by light photons from a single gamma-photon - crystal interaction. Hence, electronic and software is used to infer the gamma-photon real impacting location (impacting location in the crystal) from the output PMT currents. In addition to being used to estimate the interaction location in the crystal, these signals are used to estimate the deposited energy. An energy window is defined in order to avoid recording reduced energy photons. If the photon deposited energy value is not in the pre-defined valid energy range (energy window), the photon is rejected. Reduced energy is an indication that the photon has undergone a scatter in its path from the patient to the crystal. This means it has been deflected from its original direction and thus its inclusion reduces image quality since it will be counted in the incorrect location (scattering noise). The detected photons are recorded together with their estimated locations and the information is discretized to be displayed as a digital image. Each image pixel value represents the total photons counted in its corresponding crystal area. Thus, the image produced by the Anger camera is a histogram of the spatial distribution of all detected photons.

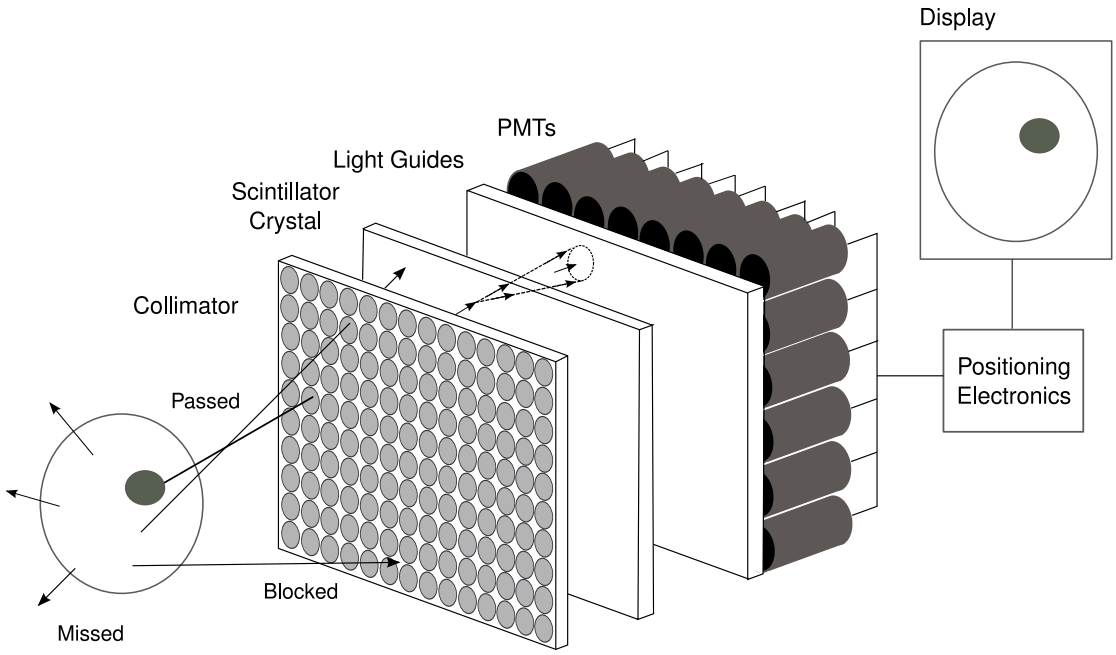

Figure 3.1: Principal components of an Anger camera. The emitted gamma-photons that manage to pass through the collimator, impact the scintillator crystal. Photoelectrons produced in the gamma-photon - crystal interaction are captured by the photomultiplier tubes. The gamma-photon energy and impact location is estimated from the photoelectron's deposited energy and impact location.

3.3.2. Principles of collimation

A parallel-hole collimator is an array of parallel bores of uniform size surrounded by septa. It allows only all photons traveling in (or nearly) a particular direction to pass through by absorbing those not verifying this condition. For this reason, its sensitivity is highly dependent on its ability to absorb the non-desired photons. Ideally, those photons not traveling along the direction of the bores (i.e. normal to the face of the scintillation crystal) should be absorbed. However, since the bore diameter is not infinitesimally small, there exists a range of incident angles that will be accepted. The larger the bore diameter, the larger the acceptance angle range and the poorer the camera spatial resolution. In addition, the collimator performance is affected by the fact that the septa material does not absorb all the incident photons. This effect, called septal penetration, accounts for some of the incident photons making it to traverse the collimator, not through the bores but through the septa. Also, part of the photons may undergo scatter, either in the bores or the septa, before reaching the scintillator crystal. All of these effects contribute to degrade image quality and are thus related to the collimator sensitivity.

For the reasons previously exposed, it is necessary that the collimator septa is composed of a highly absorbing material. Alloys of lead are the most commonly used ones. Alloys of tungsten and gold are also used, but not so frequently since the former is difficult to work and the latter is relatively expensive. The holes can vary in shape (e.g. circular, square, triangular, hexagonal), with the hexagonal being the commonly preferred for its efficiency. The bores pattern can also vary. Parallel patterns are the most frequent ones but converging and diverging patterns can also be found. For example, converging collimators magnify the image on the camera face and thus can yield to finner resolution images than those obtained with parallel-hole collimators. They may result specially useful when imaging objects of small size with respect to the camera detector face. In clinical use, they are primarily used for brain SPECT because the brain size is relatively small with respect to the field of view of most cameras.

3.3.3. Principles of detection

The scintillator detector, used to detect photons in the gamma camera, comprises: a scintillation crystal, a light guide, an array of PMTs and positioning electronics and software.

The scintillator crystal absorbs gamma-photons by the interactions of these with crystal matter (see Section 3.2.5 for a description of these interactions). This absorption results in an energy transfer from the photon to the crystal, and the corresponding emission of light and ultraviolet (UV) photons. The process is known as scintillation. The scintillator crystal can be seen as a wavelength shifter, since it emits long wavelength radiation (visible and UV) from short wavelength radiation (gamma-photons). Since the number of light photons generated in the crystal depends on the energy of the impacting photon, the scintillation process can be used for energy-selective counting. In order to increase the crystal detection capability, it is desirable for it to have high atomic number and high density, so that to augment the probability of interaction. The most commonly used materials is NaI(Tl) (thallium-doped sodium iodide). Also a thicker crystal would lead to a higher detection capability, since it can stop more gamma-photons. However, it exists a trade-off between the thickness and the intrinsic resolution of the crystal. The thicker the crystal, the poorer its intrinsic resolution.

Once the photon is absorbed by the crystal, visible light photons are created and propagate through the crystal. Each *event*, gamma-photon - crystal interaction, is seen at the outer face of the crystal as a broadly spatially distributed region of light and not as a tiny punctual spot, as we might expect. The brightest part of the region will roughly coincide with the gamma-photon impact location. The generated light photons are then transfered to the PMTs through a plate of optically transparent material called light guide. The characteristics of the light guide (e.g. thickness and shape) are sometimes chosen so that to improve the impact location estimation

from the PMTs output.

A PMT is a vacuum-tube light detector made up with an evacuated glass envelope containing an anode, a cathode and several intermediate electrodes called dynodes. They are fabricated with glass faceplates, which can be circular, square or hexagonal. Typical gamma cameras have an array of 37 to 93 hexagonal PMTs. The light photons impinge on the PMTs cathodes and generate electrons that will be measured at the PMT output. In their path through the PMT, the number of electrons is multiplied by the dynodes, since the dynodes are coated with a material that emits secondary electrons when struck by an electron. As a result, the PMT output is an amplified version of the signal initiated at the cathode when triggered by the light photons resulting from the gamma-photon - crystal interaction. As previously mentioned, each gamma-photon - crystal interaction is seen as a broadly spatially distributed region of light in the outer face of the crystal. This causes that several PMTs are reached by the light photons resulting form one interaction. The sum of all PMT outputs is computed to estimate the energy of the impacting gamma-photon. If this energy value is not within a set energy window, the photon is discarded. This energy-selective counting allows to reduce the count of scattered photons, improving image quality. The output of the PMTs is also used to compute an estimate of the photon impact location, which in general should be close to the central region of the reached PMTs. This introduces an uncertainty in photon impact location, that is intrinsic to the photon detection process.

Chapter 4

SPECT Simulations

Simulations can become a very useful tool in nuclear imaging applications because of the frequent lack of ground-truth. We found it very helpful, along this work, to perform several experimental tests, using simulations, to verify various statements and proposed models. For that reason, we dedicate this section to the description of ET simulations. In Section 4.1 we present a block diagram that defines the principal steps composing the simulation process. We mention some of the tools available for each step and pay specific attention to SimSET, the software package we chose to perform simulations. Section 4.2 describes the SimSET package, its modular structure and principal facilities. Finally, Section 4.3 is dedicated to describe some ideas related to the generation of a realistic SPECT simulation.

4.1. Steps of an ET simulation

Quantitative evaluation of ET processing methods (e.g. reconstruction, registration, denoising methods) is difficult due to the frequent lack of ground-truth. Because of this, the use of simulation tools plays a key role in algorithm testing and evaluation. We can broadly summarize the steps involved in an ET simulation according to the following pipeline:

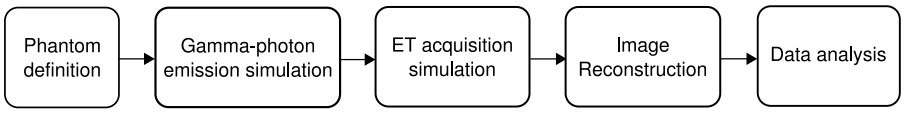

4.1.1. Phantom definition

The phantom definition depends on the particular application the simulations is done for. Phantoms can vary from a simple combination of geometrical shapes to a complex structure representing a part of the body. Figure 4.1 shows an example of a simple geometrical phantom, known as the Shep-Logan brain phantom and a more complex one, the NCAT brain phantom. Lots of phantoms have been developed for different applications. Among the most complex and most widely used, we can find the thorax and brain Zubal phantoms [19], the MCAT and NCAT phantoms [20]. These phantoms are usually based on MRI studies, since these studies achieve high quality anatomical detail. The phantom definition usually involves the definition of its shape and the radiotracer concentration level for each point. Varying these levels it is possible to perform more, or less, realistic simulations. For example, if we want to simulate a brain tumor, we could set the radiotracer concentration level to higher values in the specific tumor region. An interesting approach is presented in [21], where Grova et al. propose a procedure to generate normal and pathological brain perfusion SPECT images for evaluation of epilepsy related techniques.

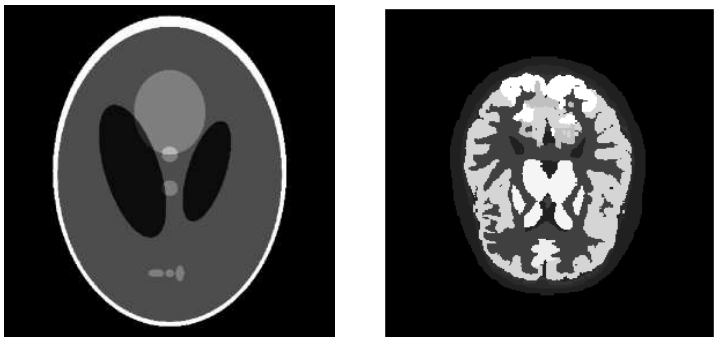

(a) Shep-Logan brain phantom (b) NCAT brain phantom

Figure 4.1: Examples of brain phantoms.

4.1.2. Gamma-photon emission simulation

The gamma-photon emission simulation consists in simulating the photon evolution process from its emission from each phantom position to its arrival to the detector or discard. Monte Carlo simulations are the most widely used techniques for this purpose. Attenuation effects throughout the phantom, i.e. scattering and absorption, can be included in the simulation process.

4.1.3. ET acquisition simulation

The ET acquisition process is the simulation of the SPECT or PET acquisition, depending on the application and thus on the chosen technique. A fraction of those photons simulated in the emission step will reach the gamma camera and will be counted as detected photons. The output data will be the corresponding sinogram images. Monte Carlo techniques are also widely used for this stage and different camera non-idealities can be included. For example, septal penetration for the collimator or the quantum efficiency for the scintillator detector.

In the field of nuclear medicine, specifically for ET, we can find tools developed to accomplish the second and third tasks: gamma-photon emission and ET acquisition simulation. These are usually the most complex and computationally demanding tasks of the simulation process. Among other aspects, they differ in complexity and the capability of incorporating different stages of the ET acquisition process. In [22, 23] the authors present a comparison of the available ET simulation tools and a summary of the tools evolution in the last decade. According to [22], in 2004 there were 7 publicly available ET simulation software packages (EGS4, MCNP, SimSET, SIMIND, GEANT, Penelope and GATE). Up to the article [22] publication date in 2006, SimSET [24] and SIMIND [25] were the most widely used packages. Nowadays, the GATE package, released in 2004, is also widely used.

In the present work, we decide to use the SimSET simulation package for the experimental verifications and analysis. Various reasons lead to this decision. First, its capacity to simulate attenuation effects (scattering and absorption), non-ideal collimator (by means of a transfer function), non-ideal detector (energy resolution, scatter, absorption and penetration in planar multilayered detectors), which are the principal non-idealities we are interested in testing. Second, the possibility of designing, either simple or complex phantoms. Third, the quality and simplicity of its on-line documentation, which allows a proper understanding of the software operation and facilities. Finally, the fact that it is currently supported by its designers (current version released in April, 2009) and is also being used by the research community.

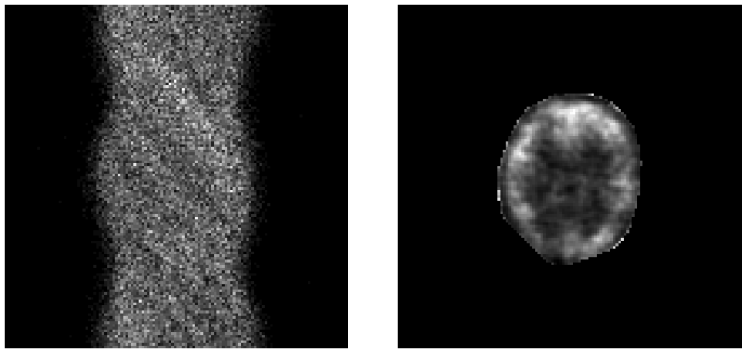

(a) Simulated sinogram (b) Reconstructed image

Figure 4.2: Sinogram and reconstructed image slices of a SPECT simulation performed with SimSET, using the NCAT brain phantom and the OSEM package for image reconstruction.

4.1.4. Image reconstruction

Up to this point we have simulated the emission and acquisition process, thus we have the projection data or sinogram images. We must therefore reconstruct the sinogram images to obtain the tomographic images. For this task we can chose among the different image reconstruction techniques, for example FBP, ML-EM or OSEM techniques presented in Section 2.4.

In the present work, for the experimental evaluations we used an implementation of the OSEM algorithm developed by Richard Larkin. This package implements the OSEM algorithm described in [14]. Apart from basic options as the number of subsets, the number of iterations, the size of the reconstruction grid, it allows to model the camera non-idealities, through a point spread function, and the attenuation effects, including them in the projection matrix computation. The election of the OSEM algorithm was based on the wide usage of that technique in nowadays clinical applications.

4.1.5. Data analysis

The last step is the data analysis, which will obviously depend on the specific application the simulation is done for. It usually includes the computation of error indicators (e.g. MSE) comparing the obtained reconstructed image against the ground-truth (phantom radioactive distribution).

4.2. SimSET package

In the following sections we present a brief description of the simulation options and operation of the SimSET package, since it is the tool that was chosen to perform all experimental testing along this work, and a proposal for realistic SPECT simulations.

SimSET (Simulation System for Emission Tomography) is a freely available software package developed by the Division of Nuclear Medicine of the University of Washington, Image Research Laboratory [24]. It uses Monte Carlo techniques to simulate the physical process and acquisition of ET, for both PET and SPECT applications. It was first released in 1993 and is in constant maintenance and development by the Image Research Laboratory group of the University of Washington. It is widely used by the nuclear medicine research community with citations in a wide variety of publications [26, 27, 28, 29]. It has a quite good on-line documentation describing its different features.

4.2.1. Package description

The software is written in a modular format, each module representing a stage of the ET acquisition process. The principal modules are: the Photon History Generator (PHG), the Collimator module, the Detector module and the Binning module. Figure 4.3 shows a block diagram representing the relationship between them and other auxiliar modules.

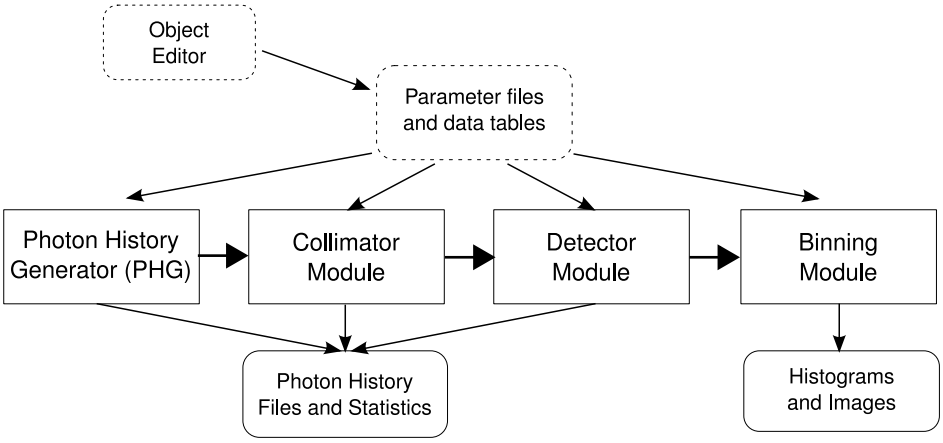

Figure 4.3: Simset package: modular structure. Block diagram showing the link between the different modules. Picture based on diagram from [24].

Photon History Generator (PHG)

The core module is the PHG, which models photon emission and transport through heterogeneous attenuators in the object of interest (phantom). Both SPECT and PET can be simulated. Scattering and photoelectric absorption simulation are supported. The inputs to the PHG module are:

- the spatial activity distribution in the phantom, i.e. the radiotracer concentration level in curies/cc assigned to each voxel
- the spatial attenuation distribution, i.e. the attenuation coefficient value (μ) assigned to each phantom voxel
- simulation options, e.g. SPECT or PET, the length of the scan, the phantom size (size in pixels and pixel size in cm), whether importance sampling is to be included or not
- data tables, used in the case of performing importance sampling

The software includes a tool called Object Editor, which facilitates the creation of the activity and attenuation spatial distribution files to be used with the PHG. This tool enables to create phantoms combining different basic shapes (voxel, sphere, cylinder) or a more complex one, previously defined (from a file). The activity and attenuation distribution files do not carry the real activity or attenuation values but indices, then used as table lookup indices in the so called translation tables. Translation tables are auxiliary text files which maps each possible object index to a corresponding data index, which is ultimately used to retrieve the specific data value. This level of indirection between the activity/attenuation indices and real values facilitates the value change of a particular voxel. The PHG allows to define the *acceptance angle* parameter, which imposes a detection constraint on the incident photon's angle. Those photons reaching the detector with an impact angle larger than the acceptance angle are discarded. This allows to simulate non-ideal collimation even if not including a specific collimator model through the Collimator Module. The PHG outputs are:

- the tracked photons information
- a statistical summary, detailed statistical information of the simulation results
- a productivity table, in case importance sampling is being used

The Collimator Module

The Collimator module receives photons from the PHG and tracks them through the collimator being modeled. Depending on the chosen collimator, different non-idealities can be simulated. For SPECT, collimators are modeled using geometric transfer functions. The available options are parallel, fan and cone beam hole collimators. For each photon, the software computes the probability that the photon would pass through a hole without interacting with the collimator. If this probability is non-zero the photon is accepted. Septal penetration and scatter within the collimator are not modeled. For PET, collimators are simulated using Monte Carlo techniques.

The Detector Module

The detector module receives photons, either directly from the PHG (if no collimator is simulated) or from the Collimator module. It tracks photons through the specified detector, recording the interactions within the detector for each photon. This interactions are used to compute the photon deposited energy and impact location. The currently supported detector models are: simple (SPECT and PET), planar (SPECT), dual head (PET), cylindrical (PET) and block (SPECT and PET). The latter is still under testing. The simple model includes only Gaussian energy blurring. The planar detector is modeled as layered rectangular parallelepipeds of different materials, where each layer can be modeled as active or inactive. Photons transport is identical for all layers, but only interactions in the active layers are considered to compute the deposited energy and impact location. The simulated interactions include scatter, absorption and penetration. Scintillation photons and photomultiplier tubes are not simulated.

The Binning Module

The Binning module is used to process the photon information recorded during the simulation. It can be used during the simulation, *on-the-fly*, or after simulation is finished, processing the corresponding *photon history files*. The photon history files contain the records of the photons evolution during the simulation (emission direction, interactions, energy levels, etc), and can be created at any stage of the simulation as outputs of the different modules. For example, the Detector module can generate a photon history file containing the records of all the detected photons. Binning can be done according to different event properties, e.g. photon energy, scattering history; and into different histogram formats, e.g. sinograms. Binning according to photon energy is done specifying the accepted energy range (minimum and maximum accepted deposited energy values) and the number of desired bins. Binning according to scattering is done specifying the minimum and maximum number of allowed scatters and the number of desired bins. In order to define the sinogram creation, the user must specify the number of bins for each binning direction: number of axial slices (e.g. the number of detector rows), the number of projection angles (must be equal to the number of collimator positions), the number of transaxial bins (i.e. the number of detector elements in a 1D projection). Also a minimum and maximum acceptable values may be defined in each direction. All photons that fall within these ranges are included in the histogram while the others are discarded. The order in which the binning parameters are specified in the Binning module parameters input file is very important, since data will be ordered in the histograms according to this ordering. Going from slowest varying to fastest varying, top to bottom. The first dimension specified in this file will vary the slowest while the last dimension specified in this file will vary the fastest. For example, if we specify the parameters in the following ordering: projection angle bins, axial slices, transaxial bins; in the output sinogram files data will be ordered: projection angle (slowest varying), axial slices, transaxial bins (fastest varying). Suppose

that we also include 2 bins to differentiate scattered and non scattered photons, and define this parameter at the beginning of the binning parameter file. In that case the output file will include two sinograms, with directions in the previous order, the first one for the non-scattered photons and the second one for the rest.

Output data

Three different output files may be obtained from the Binning module. These are: the count image, the weight image and the weight squared image. If no importance sampling is used (e.g. no stratification, forced detection, or forced non-absorption in the PHG, no forced interaction in the detector module, and no SPECT collimation), the counts image can be used directly as normal nuclear medicine data, i.e. as the number of detected photon counts. Otherwise, this is not possible since the count values are biased and do not represent real photon counts. In this case, the valuable information is carried by the weights and square weights images. When using importance sampling techniques, the weights image is the expected value image, i.e. the image that would be obtained in a sufficiently long scan with sufficiently high administered radiotracer levels [30]. If we accept the hypothesis that the photon counts are Poisson distributed, we could generate a Poisson image from the weights image, taking the latter as the Poisson parameter for each voxel. This way we could generate different ET realizations (with different Poisson realizations) from the same weights image, which can be very useful for evaluation and testing. It is also very important to take into account the squared weights image. This image represents the variance in the expected value estimation. For each of the sinogram voxels, the corresponding weights image voxel gives an estimation of the expected value of the photon counts in that voxel, and the corresponding squared weights image voxel gives the variance of that estimation. If we obtain a squared weights image with values in the order of magnitude of the weights image, that tells us that the expected photon counts estimation is not highly reliable. The same thing happens when setting the number of decays to simulate (num_to_simulate) to a number different from zero. In that case the number of decays to simulate is fixed and not computed from the scan length and phantom activity. Hence, the count values do not correspond to the real scan with the given activity and length and the weights image must be used again.

4.2.2. Importance sampling techniques

Monte Carlo techniques are widely used to study the transmission and scattering of photons through both, homogeneous or heterogeneous materials. In a conventional Monte Carlo scheme, emissions occur isotropically and photons are tracked until they escape the object. Because of the relatively small solid angle of acceptance of most cameras, the vast majority of all emitted photons either are absorbed in the object, escape without impacting the inner face of the collimator or impact the latter with an angle of incidence resulting in absorption by the collimator. Therefore, in conventional simulations, only a small percentage of decays will actually result in detected particles. A series of techniques have been developed to overcome this problem and increase the efficiency of simulations. The primary techniques are forced detection and stratification [30]. These techniques require the assignment of a *weight* to each simulated photon history, a positive real number representing the *real world* histories that particular history represents.

Stratification consists in determining the frequencies with which the various regions of the state-space are used to start a particle simulation. For example, the possible starting states can be divided into stratification cells according to the tomograph axis, the angle of photon direction with respect to the tomograph axis, and whether the starting particle will be used for sampling of non-scattered particles, scattered or both. These variables may be chosen for stratification because of their major effect on the probability on a photon being detected. A couple of *training* simulations must be performed before the real simulation in order to determine the frequencies of detected photons for each stratification cell (productivity table). Then the simulation is done

according to the found frequencies. i.e. more particles are started from the stratification cells of highest frequency. Each simulated photon path must be assigned a weight to compensate this bias effect.

In conventional Monte Carlo simulations, photons are tracked until they escape the object, are absorbed or their energy drops down from a defined threshold. Force detection refers to the modification of this technique to forbid photoelectric absorption. Instead, the photon weight is decremented at each scatter to reflect the possibility of absorption. The computational performance of the simulations is considerably increased by the combination of stratification and force detection techniques [30].

4.3. Realistic SPECT simulations

When evaluating data analysis or processing algorithms it is important to use testing images in accordance with real image characteristics. The usage of phantoms, as those mentioned in Section 4.1, helps in this sense. For the particular case of ET images, it is important to study aspects as the total number of photon counts and contrast levels in real scans. This information can then be used to generate realistic phantoms. We computed the total number of counts in SPECT sinograms of a brain perfusion study for 14 healthy adult patients. The average value of photon counts found is 5.7×10^6, with a standard deviation of 1.2×10^6 counts. This result is in agreement with the one presented by Grova et al. in [21]. Studying real contrast levels is also very important since it has great impact in a wide variety of applications. In particular, for the epileptogenic zones detection problem in medically refractory epilepsy cases (which will be presented in Section 6.1), it is of special interest since simulating a epileptogenic zone too contrasted compared to what would be normal, greatly simplifies the detection and will distort the results. Other examples can also be found in corregistration and denoising applications.

Another aspect to be considered is the number of non-idealities included in the simulation. Many of them have already been mentioned and can be simulated by the SimSET package. The larger the number of non-idealities that are taken into account, the more realistic the simulation. In [21] Grova et al. present an interesting methodology to generate normal or pathological SPECT data perfectly aligned with a high-resolution MRI, using the SimSET package. They model brain perfusion function by proposing a theoretical model of brain perfusion from measurements performed on real SPECT images. Two models are proposed, one for normal perfusion and one for ictal brain perfusion characteristic of mesial temporal lobe epilepsy. This methodology may be of interest for evaluating various methods, in particular those of epileptogenic zones localization. One disadvantage of the method is the need to combine information from various patients. As will be mentioned in posterior sections, a model made from the combination of different patients can be questionable since patients with particular lesions may present particular function patterns and also patient's age affects the results.

Chapter 5

SPECT Images Characterization

One of the main goals of the present study is to achieve a deep understanding of the SPECT images, in order to have a reasonable image characterization, which allows to design denoising and data analysis techniques. For that reason, we have dedicated Chapter 2 to the analysis of the ET techniques in general, including the acquisition process and the reconstruction techniques, and Chapter 3 to the analysis of the SPECT studies, including the physical phenomena involved and the specific SPECT acquisition process performed by the Anger cameras. This chapter focuses on the SPECT images characterization. In Sections 5.1 and 5.2, image models are derived for sinogram and tomographic (post-reconstruction) images, respectively. For sinogram characterization, a mathematical model is proposed, including the Poisson nature of the radioactive decays, the attenuation effects (scatter and absorption), non-ideal collimation and non-ideal detection effects. The derived model poses a Poisson distributed sinogram image, with the pixels being represented by independent Poisson distributed random variables. This result is widely accepted and used in the nuclear medicine research community [10, 31, 13]. Anyway, we felt it was necessary to make the analysis since, in general, the previous result is accepted but no justification or mention to its validity assumptions, are provided. Besides, we consider that the exercise of analysis, modeling and deduction up to reaching the result is crucial to understand in depth the image formation process and its characteristics. A derivation of the estimation of the Poisson parameter for each pixel, taking into account the previously mentioned effects, is also provided. In Section 5.1.6 we present some tests performed to experimentally verify the proposed model. For the tomographic or post-reconstruction images we introduce the approach proposed in [8] by Barrett et al. They study the tomographic images characterization after ML-EM reconstruction. The sinogram's independent Poisson distributed pixels are found to be transformed by ML-EM, up to a first order approximation, into a multivariate log-normal law, with a given correlation matrix. In [32], experimental tests are performed to verify the accuracy of the proposed model and the validity of the approximation.

5.1. Sinogram Images Characterization

This section focuses on the description of sinograms. In Section 5.1.1 we start introducing some basic concepts related to the sinogram formation process and general sinogram characteristics. Next, in Sections 5.1.2, 5.1.3 and 5.1.4, we proceed to introduce a mathematical model of the sinogram formation process in SPECT with Anger like cameras. For simplicity, we divide the formation process into three main stages: photon emission, photon evolution and camera acquisition. Through this approach, we verify the accepted model of independent, Poisson distributed pixels in the sinograms and find certain conditions of validity of the model. We also propose a model of the *noise-free* sinogram, i.e. the image of the Poisson parameters corresponding to each sinogram pixel. Finally, in Section 5.1.6 we perform experimental tests to validate the theoretical results.

The idea of modeling the detected photon's distribution as a binomial selection of a Poisson process, and therefore remaining Poisson distributed, is also presented by Barrett et al. [5] and Harrison et al. [6] for Anger like cameras and by Marcovski in [7] for projection radiography. As far as we are concerned, a detailed analysis of the acquisition process and justification of the validity of the previous assumption at each step is not presented. In this work we take the previous idea and analyze each step of the acquisition process, starting from the 3D volumetric emission, considering photon evolution throughout the volume and the acquisition process itself, in order to understand in depth the process, study the applicability of the model and justify each assumption that is made.

5.1.1. Noise Sources

One of the main causes of SPECT image degradation is *photon* noise. *Photon* noise, also known as Poisson noise, has its origin in the random nature of radioactive decays. Gamma-rays are the result of radioactive decays, which can be modeled as a Poisson process (c.f. Section 3.2.4). The probability of an event being counted in a certain detector region is proportional to the expected number of gamma-rays arriving to that region. Thus the expected value of counts in bright areas is higher than that of dark areas. However, the exact number of counts is a random variable. If the same emission experiment is repeated several times, the number of recorded photons during a given time period will be different each time. As will be shown in the following, the fluctuation in photon counts is accurately modeled by a Poisson distribution. This fluctuation gives a speckled appearance to the sinograms, giving it the name *noise*. Figure 5.1 shows an example of a real sinogram. We recall the definition of sinogram introduced in Section 2.3: for a given volume slice, the set of all 1D projections for $0 \leq \theta < 2\pi$, as a 2D function of x_r and θ, is named sinogram.

Let us cal *noise-free* sinogram the image of expected count values. If we could repeat the exact acquisition experiment infinite times, the *noise-free* sinogram would be the average of the sinograms obtained experimentally. It could also be obtained with high enough total counts, i.e. for a sufficiently high radioactive concentration level or for a long enough scan. The latter taking into account the scan length restriction impossed by the approximation $\lambda T << 1$ (c.f. Section 3.2.4). However, nuclear medicine images tend to be very noisy, since the low radiotracer doses administered to the patient results in low count images.

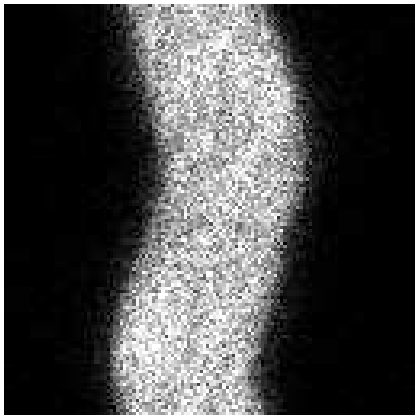

Figure 5.1: Real sinogram image. Notice the speckled appearance of the image. Image provided by the Center of Nuclear Medicine of Hospital de Clínicas, Facultad de Medicina, Universidad de la República, Uruguay.

There exists other sources of SPECT images degradation such as attenuation effects, scatter noise, the camera non-ideal response. However, it is important to remark that those degradation

sources are not the cause of photon counts fluctuations but it is the random nature of radioactive decays. As it will be explained in the following sections, for those gamma cameras working in *counting* mode, effects as attenuation, scatter noise and the camera non-ideal response will affect the expected counts value image or *noise-free* sinograms.

5.1.2. Photon Emission Model

The following analysis is strongly based on the studies of photon detection in ET images presented by Barrett and Swindell in [6] and by Barret, Myers and Dhurjaty in [5]. We have already seen that photon emission can be modeled by a Poisson process (c.f. Section 3.2.4). Given an emitting volume $\mathcal{V}$ we propose to model the distribution of emitted photons $\mathbf{V}(\mathfrak{r})$ in a time period T as a sequence of Poisson impulses randomly distributed in space,

$$\mathbf{V}(\mathfrak{r}) = \sum_{k=1}^{\mathbf{K}} \delta(\mathfrak{r} - \mathbf{R}_k),$$

where $\mathfrak{r}$ and $\mathbf{R}_k$ are three-dimensional vectors, and $\mathbf{R}_k$ is a random variable. We consider the volume $\mathcal{V}$ and exposure time T during which emissions occur at positions $\{\mathbf{R}_k\}$ contained in $\mathcal{V}$. $\mathbf{K}$ is a Poisson random variable of parameter λ representing the total number of photons emitted by volume $\mathcal{V}$ during time period T. δ is the delta function (a generalized function) so that $\mathbf{V}(\mathfrak{r})$ is a generalized random process.

It can be shown (see Appendix A) that the expected value of the process $\mathbf{V}(\mathfrak{r})$ is

$$\mathrm{E}[\mathbf{V}(\mathfrak{r})] = \lambda p(\mathfrak{r}), \tag{5.1}$$

with $p(\mathfrak{r})$ the probability density function of the *i.i.d* random variables $\mathbf{R}_k$. Thus for a given location $\mathfrak{r}$ in $\mathcal{V}$, the mean number of photons emitted per unit volume is proportional to both, the probability of a photon being emitted at that location and the expected total number of emitted photons λ.

Let us introduce function $V(\mathfrak{r})$ with

$$V(\mathfrak{r}) = \mathrm{E}[\mathbf{V}(\mathfrak{r})], \tag{5.2}$$

i.e. $V(\mathfrak{r})$ represents the expected number of photons emitted in all directions from a unit volume centered at $\mathfrak{r}$ in a time period T. Since λ is the expected **total** number of emitted photons in $\mathcal{V}$, it must verify

$$\lambda = \int_{\mathcal{V}} V(\mathfrak{r}) d\mathfrak{r}. \tag{5.3}$$

Finally, from equations 5.1-5.3 we have

$$p(\mathfrak{r}) = \frac{V(\mathfrak{r})}{\lambda} = \frac{V(\mathfrak{r})}{\int_{\mathcal{V}} V(\mathfrak{r}) d\mathfrak{r}}. \tag{5.4}$$

The autocorrelation and autocovariance functions of $\mathbf{V}(\mathfrak{r})$ are given by [5],

$$R_{\mathbf{V}}(\mathfrak{r}, \mathfrak{r} + \mathfrak{l}) = V(\mathfrak{r})\delta(\mathfrak{l}) + V(\mathfrak{r})V(\mathfrak{r} + \mathfrak{l})$$

$$K_{\mathbf{V}}(\mathfrak{r}, \mathfrak{r} + \mathfrak{l}) = V(\mathfrak{r})\delta(\mathfrak{l}).$$

It is interesting to notice that $V(\mathfrak{r})$ has a dual interpretation. It is the mean number of emitted photons per unit volume and after normalization (5.4) is the probability density on the position of any individual emission.

It is also of interest to study the statistics of the number of emitted photons from a given region or sub-volume of $\mathcal{V}$. Let us consider a division of volume $\mathcal{V}$ in N voxels of equal volume v. The random variable $\mathbf{V}_n$, $n = 1, \ldots, N$, representing the number of photons emitted from the n-th voxel is given by

$$\mathbf{V}_n = \int_{v_n} \mathbf{V}(\mathfrak{r}) d\mathfrak{r},$$

where the integration is over the volume of the n-th voxel. Note that even if all voxels have equal volume v, we make the subindex n explicit in the integral (v_n) since the integral of $\mathbf{V}(\mathfrak{r})$ varies with position. $\mathbf{K}$ photons are emitted in time T and each has a probability P_n of being emitted from pixel n with

$$P_n = \frac{\int_{v_n} V(\mathfrak{r}) d\mathfrak{r}}{\int_{\mathcal{V}} V(\mathfrak{r}) d\mathfrak{r}}.$$

As the emissions are statistically independent the conditional probability $P(\mathbf{Q} = q | \mathbf{K} = k)$ of q of the k photons being emitted from the n-th voxel is binomial with probability P_n. Therefore $\mathbf{Q}$ is Poisson distributed with parameter λP_n, since a binomial selection of a Poisson variable remains Poisson distributed with parameter equal to the mean of the input Poisson times the probability of success of the binomial distribution. This fundamental result is known as the Binomial Selection Theorem [5] and is formalized as follows.

Binomial Selection Theorem 5.1.1. *Let $\boldsymbol{K}$ be a Poisson distributed random variable with parameter λ. Let $\boldsymbol{Q}$ be a selection of $\boldsymbol{K}$ according to a binomial process with probability of selection p. Then the random variable $\boldsymbol{Q}$ is Poisson distributed with parameter λp.*

Proof. The marginal probability of $\mathbf{Q}$ is given by

$$P(\mathbf{Q} = q) = \sum_{k=q}^{\infty} P(\mathbf{K} = k) P(\mathbf{Q} = q | \mathbf{K} = k).$$

Since $\mathbf{K}$ is a Poisson random variable and $P(\mathbf{Q} = q | \mathbf{K} = k)$ is binomial we have,

$$\begin{aligned} P(\mathbf{Q} = q) &= \sum_{k=q}^{\infty} e^{-\lambda} \frac{\lambda^k}{k!} \frac{k!}{(k-q)!} p^q (1-p)^{k-q} \\ &= e^{-\lambda} \frac{(\lambda p)^q}{q!} \sum_{k=q}^{\infty} \frac{(\lambda(1-p))^{k-q}}{(k-q)!} \\ &= e^{-\lambda p} \frac{(\lambda p)^q}{q!}. \end{aligned}$$

Thus $\mathbf{Q}$ follows a Poisson distribution with expected value λp. □

Now that we have a model for the emission distribution, we can analyze the sinogram formation process. For illustration purposes we will divide the process in two stages. The *first stage* will consider the photons evolution throughout the volume $\mathcal{V}$ ending in the outer face of the collimator. The *second stage* will include the camera acquisition process, from collimation until the sinogram formation. Figure 5.2 illustrates this.

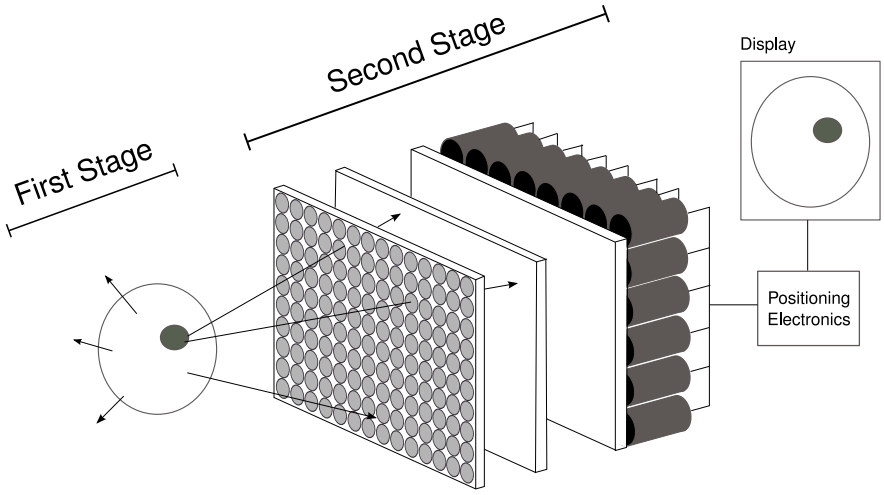

Figure 5.2: Sinogram formation process. The two stages represent the photons evolution (First Stage) and the acquisition process (Second Stage).

5.1.3. First Stage: Photon evolution

The input to the *first stage* is the array of delta functions modeled by the process $\mathbf{V}(\mathfrak{r})$. The output will be the photons reaching the collimator plane $\mathcal{C}$. By collimator plane we understand the plane limited to the collimator area, since we are not interested in the region outside the collimator/camera limits. Each delta input (emitted photon) $\delta(\mathfrak{r} - \mathbf{R}_k)$ will produce a delta output $\delta(\mathbf{r} - \mathbf{R}'_i)$ in the case of the photon reaching the collimator plane and no output if it is absorbed or out of the collimator limits. We can model the evolution of photons throughout the volume as a mapping of a sequence of impulses $\mathbf{V}(\mathfrak{r})$ to another sequence of impulses $\mathbf{U}(\mathbf{r})$.

It is not relevant to the $\mathbf{U}(\mathbf{r})$ process characterization whether the photons arrived directly or suffered deviations. The key point is whether an emitted photon impacts the collimator plane or not, so that the input delta sequence is transformed into an output delta sequence. The random variable $\mathbf{R}'_i$ represents the photon impact location in the collimator plane. Since the photons are emitted in all directions and can suffer multiple deviations until reaching the collimator plane, the impact location is not a deterministic but a random variable. Besides, considering the Binomial Selection Theorem 5.1.1 it can be seen that the number of photons reaching the collimator plane $\mathbf{K}_d$ is a Poisson random variable. The total number of emitted photons $\mathbf{K}$ follows a Poisson distribution with expected value λ. A binomial process of probability p_d rules the arrival of photons to the collimator plane, i.e. every emitted photon reaches the collimator plane with a probability p_d and is discarded with probability $(1 - p_d)$. Thus the number of photons reaching the collimator plane $\mathbf{K}_d$ follows a Poisson distribution with expected value λp_d. We represent the distribution of photons reaching the collimator plane as

$$\mathbf{U}(\mathbf{r}) = \sum_{i=1}^{\mathbf{K}_d} \delta(\mathbf{r} - \mathbf{R}'_i),$$

where $\mathbf{r}$ and $\mathbf{R}'_i$ are two-dimensional vectors, and $\mathbf{R}'_i$ is a random variable[1].

Each photon reaches the collimator plane $\mathcal{C}$ independently of the others, therefore the number of counted photons for different locations are independent. Photon counts independence could be questioned for photons coming from the same emitting source. Let us define a **punctual emitting source** as an emitting source of unit volume. If we consider a punctual emitting source $\mathcal{S}$, with $\mathbf{S}$

[1]We will use the notation $\mathbf{r}$ to differentiate the two-dimensional vectors from the three-dimensional vectors $\mathfrak{r}$.

modeling the number of emitted photons, and two collimator plane disjoint areas with number of counts $\mathbf{D}_A$ and $\mathbf{D}_B$, one might expect in the case of $\mathbf{S}$ being high, that both $\mathbf{D}_A$ and $\mathbf{D}_B$ would also be high. The same when $\mathbf{S}$ happens to be low, both $\mathbf{D}_A$ and $\mathbf{D}_B$ might be expected to be low. In that case the correlation between $\mathbf{D}_A$ and $\mathbf{D}_B$ would not be zero and the counts in both locations would not be independent. We will show in the following that this is not the case and the counts in any different locations are independent.

In the same way we did for volume $\mathcal{V}$, we discretize the collimator plane $\mathcal{C}$ in N pixels of equal area d. The random variable $\mathbf{D}_j^S$, $j = 1, \ldots, N$, representing the number of photons emitted by source $\mathcal{S}$ and reaching the collimator plane pixel j-th is given by,

$$\mathbf{D}_j^S = \int_{d_j} \mathbf{U}_S(\mathbf{r}) d\mathbf{r},$$

where the integration is over the area of pixel j and

$$\mathbf{U}_S(\mathbf{r}) = \sum_{i=1}^{\mathbf{K}_{d_S}} \delta(\mathbf{r} - \mathbf{R}_i'),$$

is the spatial random process modeling the distribution of photons reaching the collimator plane and coming from the emitting source $\mathcal{S}$.

Once again, by means of the binomial selection theorem we can prove that $\mathbf{D}_j^S$ follows a Poisson distribution for each j. The total number of photons $\mathbf{K}_{d_S}$ reaching the collimator plane and coming from $\mathcal{S}$ follows a Poisson distribution with expected value λ_S. On the other hand, with probability P_j a photon reaches the j-th pixel. Therefore we have a binomial selection of a Poisson process, which yields a Poisson variable with expected value $\lambda_S P_j$.

Let us consider the Poisson random variables $\mathbf{D}_A^S$ and $\mathbf{D}_B^S$, for $A \neq B$ two pixels in $\mathcal{C}$. Let $\mathbf{X}_k^{S,A}$ be the random variable taking value 1 if the k-th photon emitted by $\mathcal{S}$ reaches pixel A and 0 otherwise. Idem for $\mathbf{X}_k^{S,B}$.

$$\begin{aligned} P\left[\mathbf{D}_A^S = a \text{ and } \mathbf{D}_B^S = b\right] =& P\left[\sum_{k=1}^{\mathbf{K}_{d_S}} \mathbf{X}_k^{S,A} = a \text{ and } \sum_{k=1}^{\mathbf{K}_{d_S}} \mathbf{X}_k^{S,B} = b\right] \\ =& \sum_{n=a+b}^{\infty} e^{-\lambda_S} \frac{\lambda_S^n}{n!} P\left[\sum_{k=1}^{n} \mathbf{X}_k^{S,A} = a \text{ and } \sum_{k=1}^{n} \mathbf{X}_k^{S,B} = b\right]. \end{aligned}$$

$P\left[\sum_{k=1}^n \mathbf{X}_k^{S,A} = a \text{ and } \sum_{k=1}^n \mathbf{X}_k^{S,B} = b\right]$ is the probability that a of the n emitted photons reach pixel A while b reach pixel B. Photons are independent of each other, but one given photon cannot reach pixels A and B at the same time. The probability is then calculated using the trinomial law

$$\begin{aligned} P\left[\mathbf{D}_A^S = a \text{ and } \mathbf{D}_B^S = b\right] =& \sum_{n=a+b}^{\infty} e^{-\lambda_S} \frac{\lambda_S^n}{n!} \frac{n!}{(n-a-b)!a!b!} \\ & (p_{S,A})^a (p_{S,B})^b (1 - p_{S,A} - p_{S,B})^{n-a-b} \\ =& e^{-\lambda_S} \frac{(\lambda_S p_{S,A})^a}{a!} \frac{(\lambda_S p_{S,B})^b}{b!} \\ & \sum_{n=a+b}^{\infty} \frac{(\lambda_S (1 - p_{S,A} - p_{S,B}))^{n-a-b}}{(n-a-b)!} \\ =& e^{-\lambda_S p_{S,A}} \frac{(\lambda_S p_{S,A})^a}{a!} e^{-\lambda_S p_{S,B}} \frac{(\lambda_S p_{S,B})^b}{b!} \\ =& P[\mathbf{D}_A^S = a] P[\mathbf{D}_B^S = b]. \end{aligned}$$

with $p_{S,A} = \lambda_S P_A$ and $p_{S,B} = \lambda_S P_B$.

Therefore the random variables $\mathbf{D}_A^S$ and $\mathbf{D}_B^S$ are independent.
It is interesting to remark that this result is a consequence of the number of emitted photons $\mathbf{S}$ being Poisson distributed. If $\mathbf{S}$ were not Poisson distributed, the number of counts in different locations would not be independent.

5.1.4. Second Stage: Acquisition Process

The *second stage* considers the camera acquisition process. We will consider the case of Anger like cameras since these are the most commonly used cameras nowadays. The input to the camera is modeled by the process $\mathbf{U}(\mathbf{r})$, the distribution of photon counts in the collimator plane. As explained in Section 3.3.1, Anger like cameras work in *counting* mode, namely they count the detected photons. For each detected photon they find its impact location and increment in one the total counts for that location. The output image is a histogram of the detected photons. Thus each delta input $\delta(\mathbf{r}-\mathbf{R}'_i)$ produces a delta output $\delta(\mathbf{r}-\mathbf{R}'_j)$, where $(\mathbf{R}'_i-\mathbf{R}'_j)$ is a position uncertainty introduced by the camera. No output is obtained if the photon is not counted. As for the *first stage*, the acquisition process can be modeled as a mapping of a sequence of impulses $\mathbf{U}(\mathbf{r})$ to another sequence of impulses $\mathbf{G}(\mathbf{r})$. The position uncertainty is related to the acquisition process. The photon impacts the collimator plane in a certain position $\mathbf{R}'_i$. If it manages to traverse the collimator, it will impact the scintillator crystal in a position $\mathbf{R}'_c$, where $(\mathbf{R}'_i - \mathbf{R}'_c)$ accounts for the collimator effects (scatter in the collimator). The gamma-photon - crystal interaction will generate multiple light photons used to estimate the interaction position and deposited energy. The generated light photons propagate through the crystal and light guides to an array of photomultiplier tubes (PMTs). Each PMT generates an output voltage proportional to the number of light photons detected. A weighted sum of PMTs output voltages is used to estimate the deposited energy and photon impact location $(\mathbf{R}'_d)$. Thus there is a position uncertainty $(\mathbf{R}'_c - \mathbf{R}'_d)$ introduced by the detection process. The uncertainty $(\mathbf{R}'_i - \mathbf{R}'_j)$ is the resulting combination of all the detection process briefly summarized here.

As for the *first stage* case we can show that the total number of counted photons remains Poisson distributed. Once again, the input Poisson process is combined with a binomial process of counting or not counting each photon. With a binomial probability p_c the photon will be counted and with probability $(1 - p_c)$ it will be discarded. According to the Binomial Selection Theorem 5.1.1 the total number of counted photons is Poisson distributed.

Let $\mathcal{D}$ be the detector plane where the detected photons are located and counted, i.e. a detected photon is located at a position $\mathbf{R}'_j$ in $\mathcal{D}$ (which is not necessary the same location $\mathbf{R}'_c$ where it actually impacts the camera detector). We consider a division of $\mathcal{D}$ in M' pixels of equal size d. Let $\mathbf{G}_m$ be the random variable representing the number of photons counted in pixel m of the detector image. $\mathbf{G}_m$ is thus given by

$$\mathbf{G}_m = \int_{d_m} \mathbf{G}(\mathbf{r}) d\mathbf{r},$$

where the integral is over the area of the m-th detector pixel.
Following the same ideas used to show that $\mathbf{V}_n$ (the number of photons emitted from the n-th voxel) is Poisson distributed, we can show that $\mathbf{G}_m$ is also Poisson distributed. Besides, following an analysis similar to that performed for the *first stage* we can show that the number of photon counts in different locations, $\mathbf{G}_A$ and $\mathbf{G}_B$ with $A \neq B$ two different detector pixels, are independent.

It is important to highlight that **the previous approach is valid in the case of the Anger like cameras, where one detected photon is counted as one event**. For other imaging

systems where, for example, one event is mapped to an image region, this approach is not valid and different detector pixels become correlated.

To complete the sinogram formation process we still have to consider the camera rotation around the volume of interest. The previous analysis, which led us to describe the photon counts in the camera detector as a mutually independent, Poisson distributed, grid of pixels $\{G_m\}_{m=1}^{M'}$, is valid for all camera projection angles. Independence between photon counts in different projections is also valid, since projections are acquired in different time instants and therefore can be seen as independent realizations of the Poisson process.

Conclusion The photon counts in each detector pixel $\{G_m\}_{m=1}^{M'}$, for all projection angles $0 \leq \theta < 2\pi$, are mutually independent Poisson distributed random variables. Finally, recalling the definition of sinogram image, we conclude that the sinogram image pixels can be modeled as independent, Poisson distributed random variables.

5.1.5. Noise-free Sinogram Formation

Given that different pixels of the sinogram are independent Poisson random variables, we can have a complete statistical description of the sinogram through its expected value image, namely the *noise-free* sinogram $\{G_m\}_{m=1}^{M}$, with

$$\begin{aligned} G_m &= \mathrm{E}(\mathbf{G}_m) \\ &= \mathrm{E}\left[\int_{d_m} \mathbf{G}(\mathbf{r}) d\mathbf{r}\right] \\ &= \int_{d_m} \mathrm{E}[\mathbf{G}(\mathbf{r})] d\mathbf{r} \\ &= \int_{d_m} G(\mathbf{r}) d\mathbf{r}, \end{aligned}$$

where the integral is over the area of the m-th detector pixel.

This motivates the following analysis, based on an approach presented in [5], by which we model the mean photon counts distribution $G(\mathbf{r})$ as a linear transformation of the mean photon emission distribution $V(\mathfrak{r})$. This linear transformation models the acquisition process.

As defined in equation (5.2), $V(\mathfrak{r})$ is the expected number of photons emitted in all directions from a unit volume centered at $\mathfrak{r}$. We assume that $V(\mathfrak{r})$ is independent of time over the exposure time of the image acquisition process. This hypothesis is reasonable for most of the commonly used radiotracers. We start by introducing some notation. Let us consider the frame of reference attached to the volume of interest, described by the coordinates (x, y, z) as shown in Figure 5.3. Let us introduce plane $\mathcal{P}$ located somewhere in between the volume of interest and the collimator, defined as $\mathcal{P} = \{(x, y, z) \in \mathbb{R}^3 | z = z_p\}$. The mean number of photons per unit area, reaching $\mathcal{P}$ at position $\mathbf{r}_\mathfrak{p} = (x, y)$, coming from $V(\mathfrak{r})$ in straight line, from a given direction $\hat{\boldsymbol{d}}$ is

$$W(\mathbf{r}_\mathfrak{p}, \hat{\boldsymbol{d}}) = \int_0^\infty V(\mathfrak{r} - \hat{\boldsymbol{d}}l) \exp\left[-\int_0^l \mu_{att}(\mathfrak{r} - \hat{\boldsymbol{d}}l')dl'\right] dl. \tag{5.5}$$

where the 3D vector $\mathfrak{r}$, verifies $\mathfrak{r} = (x, y, z_p)$, i.e. $\mathfrak{r}$ and $\mathbf{r}_\mathfrak{p}$ represent the same point (x, y) on plane $\mathcal{P}$. The interpretation of this equation is that $W(\mathbf{r}_\mathfrak{p}, \hat{\boldsymbol{d}})$ is found by integrating the source distribution along a line parallel to $\hat{\boldsymbol{d}}$ and passing through the point $\mathbf{r}_\mathfrak{p}$, weighted with an attenuation factor (μ_{att}), since distant points along the line contribute less. Figure 5.3 illustrates this.

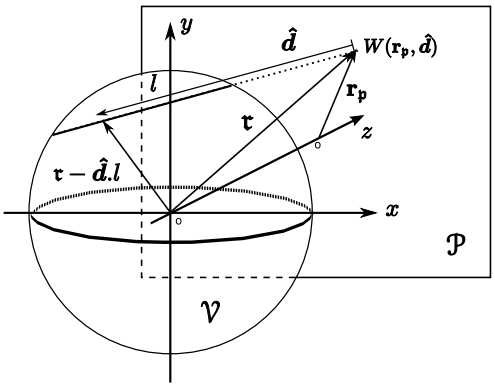

Figure 5.3: 3D to 2D projection. $W(\mathbf{r}_\mathfrak{p}, \hat{\boldsymbol{d}})$ is the mean number of photons per unit area, reaching $\mathcal{P}$ at position $\mathbf{r}_\mathfrak{p} = (x, y)$, coming from $V(\mathfrak{r})$ in straight line, in a given direction $\hat{\boldsymbol{d}}$. It is found integrating the source distribution along a line parallel to $\hat{\boldsymbol{d}}$ and passing through the point $\mathbf{r}_\mathfrak{p}$, weighted with an attenuation factor, since distant points along the line contribute less.

Because we wont consider scattered photons in this analysis, only those originating along this line and traveling with direction $\hat{\boldsymbol{d}}$ can contribute to $W(\mathbf{r}_\mathfrak{p}, \hat{\boldsymbol{d}})$. Scattered photons will affect the image. They may be modeled as additional emissive sources.

We start by including the collimator effects to the acquisition process. If we consider the plane $\mathcal{P}$ as located *behind* the collimator, $W(\mathbf{r}_\mathfrak{p}, \hat{\boldsymbol{d}})$ is the mean photons distribution in that plane when the collimator is not present. Thus the distribution with the collimator in place is

$$W_c(\mathbf{r}_\mathfrak{p}, \hat{\boldsymbol{d}}) = W(\mathbf{r}_\mathfrak{p}, \hat{\boldsymbol{d}}) T(\mathbf{r}_\mathfrak{p}, \hat{\boldsymbol{d}}), \tag{5.6}$$

where $T(\mathbf{r}_\mathfrak{p}, \hat{\boldsymbol{d}})$ is the transmittance of the collimator for photons traveling in direction $\hat{\boldsymbol{d}}$ and striking plane $\mathcal{P}$ at point $\mathbf{r}_\mathfrak{p}$. To define $T(\mathbf{r}_\mathfrak{p}, \hat{\boldsymbol{d}})$ we need a geometrical model of the collimator. We will consider a parallel-hole collimator with bores on a regular grid indexed by n. Let vector $\mathbf{r}_n$, in the collimator plane, denote the center of the n-th bore. We define the function $\beta(\mathbf{r}_\mathfrak{p} - \mathbf{r}_n)$ taking value 1 over the open area of the n-th bore and 0 otherwise. If we neglect septa penetration, the transmittance function $T(\mathbf{r}_\mathfrak{p}, \mathbf{r}_n)$ will be 1 if the entrance and exit points of the photon lie on the same bore and 0 otherwise. We know the exit point $\mathbf{r}_\mathfrak{p}$ since the plane $\mathcal{P}$ is the exit plane. On the other hand, we can find the entrance point $\mathbf{r}_e$ tracing backward from the exit point in direction $-\hat{\boldsymbol{d}}$. Thus we have

$$T(\mathbf{r}_\mathfrak{p}, \hat{\boldsymbol{d}}) = \sum_n \beta(\mathbf{r}_\mathfrak{p} - \mathbf{r}_n) \beta(\mathbf{r}_e - \mathbf{r}_n), \tag{5.7}$$

where the sum is over all bores in the collimator and the entrance point $\mathbf{r}_e$ is a 2D vector on the collimator *entrance* plane. $\mathbf{r}_e = \mathbf{r}_e(\mathbf{r}_\mathfrak{p}, \hat{\boldsymbol{d}})$, depends on $\mathbf{r}_\mathfrak{p}$ and $\hat{\boldsymbol{d}}$.
Therefore from equations (5.5) and (5.6) we have

$$W_c(\mathbf{r}_\mathfrak{p}, \hat{\boldsymbol{d}}) = T(\mathbf{r}_\mathfrak{p}, \hat{\boldsymbol{d}}) \int_0^\infty V(\mathfrak{r} - \hat{\boldsymbol{d}}l) \exp\left[- \int_0^l \mu_{att}(\mathfrak{r} - \hat{\boldsymbol{d}}l') \mathrm{d}l' \right] \mathrm{d}l \tag{5.8}$$

Now we proceed to integrate $W_c(\mathbf{r}_\mathfrak{p}, \hat{\boldsymbol{d}})$ in all directions $\hat{\boldsymbol{d}}$ to obtain the function $I_p(\mathbf{r}_\mathfrak{p})$

$$I_p(\mathbf{r}_\mathfrak{p}) = \int_0^{2\pi} W_c(\mathbf{r}_\mathfrak{p}, \hat{\boldsymbol{d}}) d\Omega(\hat{\boldsymbol{d}}). \tag{5.9}$$

$I_p(\mathbf{r}_\mathfrak{p})$ represents the mean number of photons per unit area reaching $\mathcal{P}$ at position $\mathbf{r}_\mathfrak{p}$. To contextualize with the image formation process, I_p is the mean distribution of photons impacting on the scintillator crystal. This is not the same as the distribution of photons detected on the scintillator

crystal, since that will be affected by the crystal quantum efficiency, i.e. not all the impacting photons are actually detected. From (5.8) and (5.9) we have

$$I_p(\mathbf{r}_\mathfrak{p}) = \int_0^{2\pi} T(\mathbf{r}_\mathfrak{p}, \hat{\boldsymbol{d}}) \int_0^{\infty} V(\mathfrak{r} - \hat{\boldsymbol{d}}l) \exp\left[- \int_0^{l} \mu_{att}(\mathfrak{r} - \hat{\boldsymbol{d}}l')\mathrm{d}l' \right] \mathrm{d}l\mathrm{d}\Omega(\hat{\boldsymbol{d}}). \tag{5.10}$$

We make the change of variables $\mathfrak{r}' = \mathfrak{r} - \hat{\boldsymbol{d}}l$, which will allow us to express (5.10) in the general form

$$I_p(\mathbf{r}_\mathfrak{p}) = \int_{\mathbb{R}^3} V(\mathfrak{r}) h(\mathbf{r}_\mathfrak{p}, \mathfrak{r}) \mathrm{d}\mathfrak{r}. \tag{5.11}$$

First we notice that

$$\mathfrak{r}' = \mathfrak{r} - \hat{\boldsymbol{d}}l \quad \Rightarrow \quad \hat{\boldsymbol{d}} = \frac{\mathfrak{r} - \mathfrak{r}'}{l},$$

$$l = |\mathfrak{r} - \mathfrak{r}'|,$$

and

$$l^2 \mathrm{d}l\mathrm{d}\Omega = \mathrm{d}\mathfrak{r}'.$$

Thus (5.10) can be rewritten as

$$\begin{aligned} I_p(\mathbf{r}_\mathfrak{p}) &= \int_{\mathbb{R}^3} T\left(\mathbf{r}_\mathfrak{p}, \frac{\mathfrak{r} - \mathfrak{r}'}{|\mathfrak{r} - \mathfrak{r}'|}\right) V(\mathfrak{r}') \exp\left[- \int_0^{|\mathfrak{r} - \mathfrak{r}'|} \mu_{att}\left(\mathfrak{r} - \frac{\mathfrak{r} - \mathfrak{r}'}{|\mathfrak{r} - \mathfrak{r}'|} l'\right) \mathrm{d}l' \right] \frac{\mathrm{d}\mathfrak{r}'}{|\mathfrak{r} - \mathfrak{r}'|^2} \\ &= \int_{\mathbb{R}^3} V(\mathfrak{r}') T\left(\mathbf{r}_\mathfrak{p}, \frac{\mathfrak{r} - \mathfrak{r}'}{|\mathfrak{r} - \mathfrak{r}'|}\right) \exp\left[- \int_0^{|\mathfrak{r} - \mathfrak{r}'|} \mu_{att}\left(\mathfrak{r} - \frac{\mathfrak{r} - \mathfrak{r}'}{|\mathfrak{r} - \mathfrak{r}'|} l'\right) \mathrm{d}l' \right] \frac{1}{|\mathfrak{r} - \mathfrak{r}'|^2} \mathrm{d}\mathfrak{r}' \\ &= \int_{\mathbb{R}^3} V(\mathfrak{r}') h(\mathbf{r}_\mathfrak{p}, \mathfrak{r}, \mathfrak{r}') \mathrm{d}\mathfrak{r}' \end{aligned} \tag{5.12}$$

with

$$h(\mathbf{r}_\mathfrak{p}, \mathfrak{r}, \mathfrak{r}') = T\left(\mathbf{r}_\mathfrak{p}, \frac{\mathfrak{r} - \mathfrak{r}'}{|\mathfrak{r} - \mathfrak{r}'|}\right) \exp\left[- \int_0^{|\mathfrak{r} - \mathfrak{r}'|} \mu_{att}\left(\mathfrak{r} - \frac{\mathfrak{r} - \mathfrak{r}'}{|\mathfrak{r} - \mathfrak{r}'|} l'\right) \mathrm{d}l' \right] \frac{1}{|\mathfrak{r} - \mathfrak{r}'|^2}$$

To obtain (5.13) from (5.12) we must note that, since we are concerned by function I_p on the plane $\mathcal{P}$, i.e. $z = z_p$, the vectors $\mathfrak{r} = (x, y, z_p)$ and $\mathbf{r}_\mathfrak{p} = (x, y)$ specify the same point. Therefore we have $h(\mathbf{r}_\mathfrak{p}, \mathfrak{r}, \mathfrak{r}') = h(\mathbf{r}_\mathfrak{p}, \mathfrak{r}')$ and can rewrite (5.12) as

$$I_p(\mathbf{r}_\mathfrak{p}) = \int_{\mathbb{R}^3} V(\mathfrak{r}) h(\mathbf{r}_\mathfrak{p}, \mathfrak{r}) \mathrm{d}\mathfrak{r}. \tag{5.13}$$

This transformation is a linear mapping of the 3D function $V(.)$ to the 2D function $I_p(.)$. The function $h(\mathbf{r}_\mathfrak{p}, \mathfrak{r})$ is the response at point $\mathbf{r}_\mathfrak{p}$ in the collimator exit plane to a point source at $\mathfrak{r}$ in the 3D space. The integral is over $\mathbb{R}^3$, although $V(\mathfrak{r})$ is non-zero only inside the volume of interest $\mathcal{V}$.

Now the following steps are related to the count and location uncertainty for each photon, i.e. the probability that the photon is actually detected, and in that case, in which location. We can describe the location estimation process with the conditional probability density function $p(\mathbf{r}|\mathbf{r}_\mathfrak{p})$, where $\mathbf{r}_\mathfrak{p}$ is the photon impact position in the scintillator crystal (plane $\mathcal{P}$) and $\mathbf{r}$ is the photon position estimated by the camera (plane $\mathcal{D}$). Thus we can find $G(\mathbf{r})$ as

$$\begin{aligned} G(\mathbf{r}, \epsilon) &= \eta \mathrm{P}_{acc}(\epsilon) \int_{\mathbb{R}^2} p(\mathbf{r}|\mathbf{r}_\mathfrak{p}) I_p(\mathbf{r}_\mathfrak{p}) d\mathbf{r}_\mathfrak{p} \\ &= \eta \mathrm{P}_{acc}(\epsilon) \int_{\mathbb{R}^2} p(\mathbf{r}|\mathbf{r}_\mathfrak{p}) \int_{\mathbb{R}^3} h(\mathbf{r}_\mathfrak{p}, \mathfrak{r}) V(\mathfrak{r}) d\mathfrak{r} d\mathbf{r}_\mathfrak{p} \\ &= \eta \mathrm{P}_{acc}(\epsilon) \int_{\mathbb{R}^2} \int_{\mathbb{R}^3} p(\mathbf{r}|\mathbf{r}_\mathfrak{p}) h(\mathbf{r}_\mathfrak{p}, \mathfrak{r}) V(\mathfrak{r}) d\mathfrak{r} d\mathbf{r}_\mathfrak{p}, \end{aligned} \tag{5.14}$$

where η is the detector quantum efficiency -modeling the probability of a photon impacting on the scintillator crystal actually being detected- and $P_{acc}(\epsilon)$ is the probability of the photon being inside the energy window (depending on its impact energy ϵ). We can rewrite equation (5.14) as

$$G(\mathbf{r}, \epsilon) = \int_{\mathbb{R}^3} h_T(\mathbf{r}, \mathfrak{r}, \epsilon) V(\mathfrak{r}) d\mathfrak{r}, \tag{5.15}$$

with

$$h_T(\mathbf{r}, \mathfrak{r}, \epsilon) = \eta P_{acc}(\epsilon) \int_{\mathbb{R}^2} p(\mathbf{r}|\mathbf{r}_\mathfrak{p}) h(\mathbf{r}_\mathfrak{p}, \mathfrak{r}) d\mathbf{r}_\mathfrak{p}.$$

The linear transformation in (5.15) accounts for the projection of 3D data to 2D, the collimator non-ideal response, detection and location uncertainty introduced by the camera. The function $h_T(\mathbf{r}, \mathfrak{r})$ is the *sensitivity* of the camera at the 2D point $\mathbf{r}$ to the emission coming from the 3D point $\mathfrak{r}$. We recall that the scattered photons are assumed to be discarded.
Now we can proceed to find the mean photon counts in each sinogram pixel as

$$\begin{aligned} G_m &= \int_{d_m} \int_{\mathbb{R}^3} \int h_T(\mathbf{r}, \mathfrak{r}, \epsilon) V(\mathfrak{r}) \mathrm{d}\epsilon \mathrm{d}\mathfrak{r} \mathrm{d}\mathbf{r} \\ &= \int_{\mathbb{R}^3} \int_{d_m} \int h_T(\mathbf{r}, \mathfrak{r}, \epsilon) \mathrm{d}\epsilon \mathrm{d}\mathbf{r} V(\mathfrak{r}) \mathrm{d}\mathfrak{r} \\ &= \int_{\mathbb{R}^3} h_m(\mathfrak{r}) V(\mathfrak{r}) \mathrm{d}\mathfrak{r}, \end{aligned} \tag{5.16}$$

with

$$h_m(\mathfrak{r}) = \int_{d_m} \int h_T(\mathbf{r}, \mathfrak{r}, \epsilon) \mathrm{d}\epsilon \mathrm{d}\mathbf{r},$$

$h_m(\mathfrak{r})$ being the *sensitivity* of pixel m to the 3D point $\mathfrak{r}$.

5.1.6. Experimental Validation

Distribution Tests

A series of tests were carried out to experimentally verify the proposed hypothesis of the photon counts distribution. Pearson's chi-square goodness of fit tests (see Appendix B) were performed to verify whether the Poisson distribution is a reasonable hypothesis for photon counts in each sinogram location. We start by the simplest case, a punctual emitting source and then test a more complex case, an emitting sphere. For each case Q simulations are performed. For a given simulation q, $q = 1, \ldots, Q$, data consists of a set of M values G_m^q, $m = 1, \ldots, M$ where the index m represents a pair (*detector element*, *angle*) and G_m^q represents the number of photons detected in the m-th data bin for the q-th simulation. Thus the hypothesis to test is that the set of Q values $\{G_m^q\}_{q=1,\ldots,Q}$ are Poisson distributed. If the null hypothesis cannot be discarded with a significance level of 0.05, we assume that the Poisson distribution is a reasonable hypothesis for the photon counts distribution in the given location m.

Simulations Description

Punctual Source - No effects The emitting source is an off-centered unit volume sphere (1 cc) in a brain-like uniform attenuating sphere ($\mu = 0.15$) of radius 7 cm, so that attenuation (scattering and absorption) is simulated. However, scattered photons are discarded so that no scatter noise is considered. The activity level and the length of the scan are set according to values provided for real scans.

- Scan duration: 30mins

- Mean brain volume: 1200ml
- Approximately 25-30mCi (925-1110MBq) of radioactive tracer are injected to the patient (patient of 70kg approx).
- For perfusion tracers (HMPAO, ECD) approximately 7% of the doses reaches the brain.

RESULT: 1.458e-6 ci/cc tracer concentration in the brain. The acceptance angle (c.f. Section 4.2.1) is set to 4.5 degrees to simulate non-ideal collimation. To set the acceptance angle value we considered real collimator parameters. The value is determined based on the parameters of an hexagonal holes collimator designed for a resolution FWHM = 1.0 cm at distance 10.0 cm [33]. Projections are of 128×128 pixels with a pixel size of 0.22×0.14 cm. A total of 128 projections are obtained in the range $0 - 360$ degrees. Non-ideal detection is not simulated. A total of 1000 simulations are performed.

Punctual Source - Effects The simulation is set as in the previous case but scattered photons are not discarded (scatter noise is included) and non-ideal detector effects are simulated. A total of 1000 simulations are performed.

Sphere - No Effects The emitting source is an off-centered sphere of radius 5 cm, in a brain-like uniform attenuating sphere of radius 7 cm, so that attenuation (scattering and absorption) is simulated. The activity level and scan length are set as for the punctual source case. The acceptance angle is set as in the previous case to 4.5 degrees to include non ideal collimator effects. Projections are of 128×128 pixels with a pixel size of 0.22×0.14 cm. A total of 128 projections are obtained in the range $0 - 360$ degrees. A total of 200 simulations are performed. Note that the number of simulations is significantly reduced compared to the previous case since the sphere simulation is much more time consuming than the punctual source one.

Sphere - Effects The simulation is set as in the previous case but scattered photons are not discarded (scatter noise is included) and non-ideal detector effects are simulated. A total of 200 simulations are performed.

Evaluation and Results

For each sinogram *valid* location, Pearson's goodness of fit test (c.f. Appendix C) was performed considering the corresponding 1000 or 200 samples (depending on the tested configuration). By *valid* location we mean those voxels that are part of the sinogram sinusoid, i.e. not part of the background. For all the tested configurations, punctual source and the emitting sphere with and without effects, the null hypothesis cannot be discarded in **95%** of the tested locations. Since the test significance level is 0.05, we conclude that the Poisson distribution hypothesis cannot be rejected in all the studied cases. Table 5.1 shows the exact percentage of locations where the null hypothesis cannot be rejected for each tested configuration.

Attenuation effects, i.e. scatter and absorption, were simulated in all the studied cases. This way we find that photon counts follow a Poisson distribution even on the presence of attenuation effects. The same outcome is found when adding scatter noise. These results suggest the validity of the model proposed for the *first stage* (Section 5.1.3). Regarding the camera effects, non-ideal detector effects were simulated. Since the simulated non-ideal response is only partial (not all non-ideal effects are included) we conclude that up to the limits of the simulation, the non-ideal camera response does not change the Poisson character of the photon counts distribution. This result is in line to validate the proposed model for the *second stage* (Section 5.1.3).

	Punctual Source		Sphere	
	No-Effects	Effects	No-Effects	Effects
Null Hyp. No Rej. (%)	94.86	94.98	95.00	94.91

Table 5.1: Distribution test results. Percentage of the tested cases where the null hypothesis cannot be discarded with a significance level of 0.05.

Statistical Dependence Tests

We perform statistical dependence tests in order to validate the hypothesis of independence between counts in different sinogram locations. Strictly speaking independence cannot be experimentally verified. Instead certain statistical dependence relationships can be tested, e.g. linear relationships (correlation tests), monotonic relationships (rank correlation tests). With the latter we can verify whether or not data is statistically dependent according to the specific tested relationship, but we will not be able to say that variables are independent. As will be shown in Section 7, we are interested in denoising sinograms before reconstruction to improve the reconstructed image quality. Indeed that is one of the aims motivating the noise statistical characterization. Since the method proposed to perform sinograms denoising is based on the hypothesis of uncorrelated noise, we are interested in verifying this kind of statistical dependence. In that sense we decide to use Spearman's and Kendall's rank correlation tests, since they allow to test for monotonic dependence, therefore including correlation (linear relationship) but not only restricted to it. These tests are a good trade-off between simplicity and accounting for not only linear relationships. Spearman's and Kendall's rank correlation coefficients measure the extent to which, as one variable increases, the other variable tends to increase, without requiring that increase to be linear. Permutation tests can then be used to test the significance of the rank correlation value against the null hypothesis of non-correlation. These kind of tests are non-parametric, since no specific distribution is assumed over the variables. For more details see Appendix C.

We start by the simplest case, a punctual emitting source and then test a more complex case, an emitting sphere. For each test, Q simulations are performed. For a given simulation q, $q = 1, \dots, Q$, data consists of a set of M values G_m^q, $m = 1, \dots, M$ where the index m represents a pair (*detector element*, *angle*) and G_m^q represents the number of photons detected in the m-th data bin for the q-th run. To compute the rank correlation coefficients we will only consider voxels m lying inside the sinogram sinusoid, i.e. we exclude background voxels. Global and local statistical dependence are studied. By global we understand all pairwise dependence[2], i.e. the statistical dependence between the counts in every pair of locations, given by

$$\text{statDep}(G_i, G_j) \quad \forall (i,j) \quad i,j = 1, \dots, M. \tag{5.17}$$

For example, for the Spearman's rank correlation coefficient, Equation (5.17) becomes

$$\rho(G_i, G_j) = \frac{\sum_{q=1}^{Q} (G_i^q - \bar{G}_i)(G_j^q - \bar{G}_j)}{\sqrt{\sum_{q=1}^{Q} (G_i^q - \bar{G}_i)^2 \sum_q (G_j^q - \bar{G}_j)^2}}, \tag{5.18}$$

with $\bar{G}_i = \frac{1}{Q} \sum_{q=1}^{Q} G_i^q$.
On the other hand, by local dependence we mean the dependence of a given variable with its neighbors, given by

$$\text{statDep}(G_i, G_j) \quad \forall i = 1, \dots, M, j \in \text{neighbourhood(i)}.$$

[2] All pairwise dependences are considered when the number of variables is treatable. Otherwise, a percentage of all the possible combinations is tested.

where Equation (5.18) remains valid for the Spearman coefficient, but variables G_j are restricted to a neighborhood of G_i.

Simulations Description

Punctual Source - No Effects Same configuration as in the distribution test case (punctual source - no effects). 1000 simulations are performed.

Punctual Source - Effects Same configuration as in the distribution test case (punctual source - effects). 1000 simulations are performed.

Sphere - No Effects Same configuration as in the distribution test case (sphere no - effects). 200 simulations are performed.

Sphere - Effects Same configuration as in the distribution test case (sphere - effects). 200 simulations are performed.

Evaluation and Results

In order to simplify the global statistical dependence computation, we decide to compute all pairwise correlations between 1000 variables randomly chosen, and repeat the experiment A times, with A depending on the number of total voxels and assuring that the 30% of the total variables are tested. The only exception is the Punctual source - No effects case, where all pairwise correlations have been evaluated since the total number of variables is manageable. For each run a, $a = 1, \ldots, A$, the rank correlation coefficient (Spearman's or Kendall's) is computed pairwise between the 1000 randomly chosen variables (including the Q realizations of each variable obtained from the Q simulations),

$$\text{statDep}_a(G_i, G_j) \quad \forall(i,j) \quad i,j = 1, \ldots, 1000,$$

and the percentage of significantly correlated variables (statDep(%)) is computed as

$$\text{statDep}_a(\%) = \frac{\text{total of significantly correlated variables}}{\text{total tested correlations}},$$

with (total tested correlations $= A(A-1)/2$), considering that the rank correlation coefficient is symmetric ($\text{statDep}_a(G_i, G_j) = \text{statDep}_a(G_j, G_i)$). Then, we compute the mean and standard deviation of the $\text{statDep}_a(\%)$ indicator for the A runs as

$$\text{m}_{\text{statDep}} = \frac{1}{A}\sum_{a=1}^{A} \text{statDep}_a(\%),$$

$$\text{std}_{\text{statDep}} = \frac{1}{A}\sum_{a=1}^{A} (\text{statDep}_a(\%) - \text{m}_{\text{statDep}})^2.$$

For the local dependence case, the neighborhood is defined by the parameters n, m and p, the window size in each direction is $(2n+1)$, $(2m+1)$, $(2p+1)$ with directions representing: $x =$ bin, $y =$ slice and $z =$ angle. The statistical dependence is then evaluated between the central position and its neighboring locations. The experiment is repeated in B randomly chosen locations, with B being 30% of the total considered variables and $n = 4$, $m = 3$, $p = 4$. The rank correlation coefficient (Spearman's or Kendall's) between each location b and each of its neighbors is computed as

$$\text{statDep}(G_b, G_j) \quad \forall b = 1, \ldots, B, j \in \text{neighbourhood(b)}.$$

Stat. Dep. (%)		Punctual Source		Sphere	
		No-Effects	Effects	No-Effects	Effects
GLOBAL	Spearman	4.95 ± 0.05	4.99 ± 0.05	5.00 ± 0.03	5.00 ± 0.03
	Kendall	4.94 ± 0.05	4.99 ± 0.05	4.98 ± 0.03	4.98 ± 0.03
LOCAL	Spearman	5.48 ± 1.62	5.43 ± 1.50	5.19 ± 0.99	5.19 ± 0.99
	Kendall	5.47 ± 1.62	5.42 ± 1.50	5.17 ± 0.99	5.16 ± 0.98

Table 5.2: Statistical dependence experimental results for the Spearman's and Kendall's rank correlation tests.

The percentage of neighboring variables significantly correlated to b (nStatDep(%)) is computed as

$$\text{nStatDep}_b(\%) = \frac{\text{total of neighbours significantly correlated to } b}{\text{total neighbours}}.$$

Then, we compute the mean and standard deviation of the $\text{nStatDep}_b(\%))$ indicator for the B locations as

$$\text{m}_{\text{nStatDep}} = \frac{1}{B}\sum_{b=1}^{B}\text{nStatDep}_b(\%),$$

$$\text{std}_{\text{nStatDep}} = \frac{1}{B}\sum_{b=1}^{B}(\text{nStatDep}_b(\%) - \text{m}_{\text{nStatDep}})^2.$$

Table 5.2 shows the obtained results for the four tested configurations. For each configuration we present the corresponding global ($\text{m}_{\text{StatDep}} \pm \text{std}_{\text{StatDep}}$) and local ($\text{m}_{\text{nStatDep}} \pm \text{std}_{\text{nStatDep}}$) statistical dependence results for both considered coefficients, Spearman's and Kendall's. For all the studied configurations, for both global and local analysis, the percentage statistical dependence is around 5%. Some cases present more variance than others, but the worst case is 7% (local dependence for the Punctual source - No effects case). Given that the statistical dependence significance tests have a significance level of 0.05, we conclude that the hyphotesis of statistial independence cannot be rejected, for all the configurations and in both cases, global and local dependence. The latter (local dependence) is the most critical one, since given the characteristics of the sinogram formation process the most probable statistical dependence is local dependence. This way we can conclude that the hypothesis of uncorrelated sinogram pixel values cannot be rejected.

5.2. Tomographic Images Characterization

In the literature we find many works on tomographic images statistical characterization for various image reconstruction algorithms [34, 35, 36, 37, 36, 38, 39, 40, 41]. In general, these analysis compute first and second order statistics of the image but do not propose a distribution law for it. They are usually focused on correlation analysis, verifying the image correlation matrix characteristics. Depending on the reconstruction algorithm, these approaches study the image noise evolution with parameter variation, with increasing iteration number, etc. We are interested in image characterization after OSEM reconstruction since, as mentioned in previous sections, this algorithm is widely used in clinical applications. In [8], Barrett et al. present a detailed statistical description of tomographic images for ML-EM reconstruction. They show that, up to an approximation, the reconstructed image follows a multivariate log-normal law. In section 5.2.1 we present this approach. Next, in Section 5.2.2, we present the extension of Barrett et al. work, proposed by Soares et al. [42], to images reconstructed using the OSEM algorithm.

5.2.1. Image characterization after ML-EM reconstruction

As described in Section 2.4.2, the ML-EM algorithm is an iterative algorithm that produces a sequence of estimates of an unknown object that converges to its ML estimate. We are interested in knowing noise characteristics in the reconstructed image, i.e. how sinograms noise is transformed by the ML-EM reconstruction method. Unlike for the FBP case, a closed form for the reconstruction noise cannot be found for the ML-EM estimation. Barrett et al. [8] present an approach to describe noise properties in an ML-EM reconstruction. They propose a general theoretical formulation were two basic approximations are made. Experimental validation of both, theory and approximations, is presented in [32]. We present a brief summary of the formulation proposed by Barrett et al. and refer the reader to the original article for further details.

Let us start by introducing some notation and statistical characterization of the variables. Following notation introduced in Section 5.1.1, the unknown object is represented by a set of N volume elements each of which having constant value V_n, $n = 1, \ldots, N$. This value represents the average number of gamma-rays emitted from that volume element during the study period T. The volume is represented by the $N \times 1$ column vector V, where V_n is the n-th component of V. Sinogram data is represented by the $M \times 1$ column vector $\mathbf{G}$, with $\mathbf{G}_m$ its m-th component. Index $m = 1, \ldots, M$ represents all possible combinations of projection angle and detector element. $\mathbf{G}_m$ represents the number of detected photons in data bin m. Note that V is deterministic and $\mathbf{G}$ is a random variable. As shown in Section 5.1, for a given V, $\mathbf{G}$ components are independent Poisson random variables.

The $M \times N$ matrix H is the projection matrix. Each component $[H]_{mn}$ represents the probability that a gamma-ray emitted by the volume element n is recorded in data bin m. The projection matrix H can model the non-idealities affecting detection. See Section 2.4.2 for a description of them. Thus the mean value G of gamma-rays recorded, conditioned to a certain V is

$$G = HV.$$

We define an $M \times 1$ noise vector $\mathbf{N} \equiv \mathbf{G} - G$, so that

$$\mathbf{G} = HV + \mathbf{N}.$$

By construction, the expected value of $\mathbf{N}$ is zero. On the other hand, since $\mathbf{G}$ components are independent Poisson distributed random variables (for a given V), $\mathbf{N}$ components are also independent and $\mathbf{N}_m$ variance is the conditional mean of $\mathbf{G}$, that is $[HV]_n$. To simplify notation, Barrett et al. introduce a *component-operation* notation under which, if a and b are $N \times 1$ vectors, and A is an $M \times N$ matrix, we have

$$[ab]_n \equiv a_n b_n$$

$$[a/b]_n \equiv a_n/b_n$$

$$[\ln a]_n \equiv \ln(a_n)$$

but

$$[Aa]_m = \sum_{n=1}^{N} A_{mn} a_n.$$

Since the ML-EM algorithm correction factor is multiplicative, it is useful to take logarithms in the ML-EM main iteration formula. Taking logarithms, Equation (2.8) in component-operation notation is

$$\hat{\mathbf{Y}}^{(k+1)} = \hat{\mathbf{Y}}^{(k)} + \ln\left[\frac{1}{s} H^T \left(\frac{\mathbf{G}}{H\hat{V}^{(k)}}\right)\right], \tag{5.19}$$

where

$$\mathbf{Y}^{(k)} \equiv \ln[\hat{V}^{(k)}]. \tag{5.20}$$

The conditional expectation value of $\mathbf{Y}^{(k)}$ is defined as

$$E(\mathbf{Y}^{(k)}|V) \equiv \ln(A^{(k)}), \tag{5.21}$$

and the deviation of $\mathbf{Y}^{(k)}$ from its expected value as $\boldsymbol{\epsilon}^{(k)}$, so that

$$\mathbf{Y}^{(k)} = \ln(A^{(k)}) + \boldsymbol{\epsilon}^{(k)}. \tag{5.22}$$

Let us now introduce the first approximation, namely *Approximation 1*, which assumes that the noise in the reconstruction will be small compared to the mean reconstruction. To account for this, the image at the k-th iteration is expanded about the ensemble average image for that iteration and only linear terms in the fluctuation are significant.

$$\hat{V}^{(k)} = A^{(k)} \exp(\boldsymbol{\epsilon}^{(k)}) \simeq A^{(k)}[1 + \boldsymbol{\epsilon}^{(k)}]. \tag{5.23}$$

Thus, if *Approximation 1* holds we have

$$\hat{V}^{(k)} = A^{(k)} + \boldsymbol{\delta}^{(k)}, \tag{5.24}$$

with

$$\boldsymbol{\delta}^{(k)} \simeq A^{(k)} \boldsymbol{\epsilon}^{(k)}. \tag{5.25}$$

We can then assume $\boldsymbol{\epsilon}^{(k)} \ll 1$ when the noise in the reconstruction $\boldsymbol{\delta}^{(k)}$ is small compared to the mean reconstruction $A^{(k)}$. In [32], the authors show a quantitative assessment of the validity range of this approximation. The approximation is in general reasonable, but tends to be more doubtful when the iteration number increases or the number of counts in the image is small, since higher noise levels are present in these cases.
The second approximation is not strictly necessary for the final noise characterization but simplifies the operations. It states that after a few iterations, the projection of the current estimate $HA^{(k)}$, will closely resemble the noise free projection HV. This approximation is also experimentally verified in [32].

Under *Approximation 1* and *Approximation 2*, equation 5.19 becomes

$$\begin{aligned}\hat{\mathbf{Y}}^{(k+1)} &= \ln(A^{(k+1)}) + \boldsymbol{\epsilon}^{(k+1)} \\ &= \ln(A^{(k)}) + \boldsymbol{\epsilon}^{(k)} + \ln\left\{\frac{1}{s}H^T\left[\frac{HV}{HA^{(k)}}\right]\right\} \\ &\quad + \frac{1}{s}H^T\left[\frac{\mathbf{N}}{HA^{(k)}}\right] - \frac{1}{s}H^T\left[\frac{[H(A^{(k)}\boldsymbol{\epsilon}^{(k)})]}{[HA^{(k)}]}\right].\end{aligned}$$

Equating random terms and non-random terms separately,

$$\ln(A^{(k+1)}) = \ln(A^{(k)}) + \ln\left\{\frac{1}{s}\frac{HV}{HA^{(k)}}\right\}, \tag{5.26}$$

and

$$\boldsymbol{\epsilon}^{(k+1)} = \boldsymbol{\epsilon}^{(k)} + \frac{1}{s}H^T\left[\frac{\mathbf{N}}{HA^{(k)}}\right] - \frac{1}{s}H^T\left[\frac{[H(A^{(k)}\boldsymbol{\epsilon}^{(k)})]}{[HA^{(k)}]}\right]. \tag{5.27}$$

It is interesting to notice from Equation (5.26) that the ensemble mean image can be obtained by performing a reconstruction with noise-free data $\mathbf{G} \equiv HV$. On the other hand, Equation (5.27) shows how to obtain the random noise in the $(k+1)$ estimate, based on the noise from data $\mathbf{N}$ and the previous noise estimate $\boldsymbol{\epsilon}^{(k)}$.

After some operations it can be seen that $\boldsymbol{\epsilon}^{(k)}$ can always be written as a linear transformation of the original data noise $\mathbf{N}$

$$\boldsymbol{\epsilon}^{(k)} = Z^{(k)}\mathbf{N}, \tag{5.28}$$

where $Z^{(k)}$ is an $N \times M$ matrix satisfying a recursion relation

$$Z^{(k+1)} = D^{(k)} + [I - C^{(k)}]Z^{(k)},$$

which depends on: the iteration number k, the object V, the system projection matrix H and the noise-free estimates $A^{(k)}$. See Appendix D for the complete expressions of $C^{(k)}$ and $D^{(k)}$.
We are mostly interested in the statistical properties of $\boldsymbol{\epsilon}^{(k)}$, which can be determined from Equation (5.28). From Equation (5.28) and knowing that $E(\mathbf{N}|V) = 0$, the conditional expected value is

$$E(\boldsymbol{\epsilon}^{(k)}|V) = 0.$$

The marginal probability density for any particular component of vector $\boldsymbol{\epsilon}^{(k)}$ can be determined invoking the central-limit theorem. Since at any iteration k the components of $\boldsymbol{\epsilon}^{(k)}$ are a linear combination of a large number of independent random variables (the components of vector $\mathbf{N}$) it follows from the central-limit theorem that each of these components is normally distributed. Another way of achieving the same result is noticing that each component of vector $\mathbf{G}$ is Poisson distributed, which in the case of a large expected value can be well approximated by a Gaussian distribution. Thus if the number of detected photons is sufficiently high for each component (even 10 or so) we can say $\mathbf{G}$ is a vector of independent Gaussian distributed random variables. In that case, each component of $\mathbf{N}$ is also normally distributed and equation (5.28) says that each component of $\boldsymbol{\epsilon}^{(k)}$ is normally distributed. Furthermore, for any of the two previous arguments, any linear combination of the components of $\boldsymbol{\epsilon}^{(k)}$ is normally distributed. This way all marginal probability densities derivable from the full multivariate density on $\boldsymbol{\epsilon}^{(k)}$ must be normal, which is only possible if the multivariate density is Normal. Thus we have

$$p(\boldsymbol{\epsilon}^{(k)}|V) = \frac{1}{(2\pi)N|K_\epsilon^{(k)}|^2}\exp\left[-\frac{1}{2}(\boldsymbol{\epsilon}^{(k)})^T[K_\epsilon^{(k)}]^{-1}(\boldsymbol{\epsilon}^{(k)})\right],$$

where $K_{\boldsymbol{\epsilon}}^{(k)}$ is the covariance matrix for $\boldsymbol{\epsilon}^{(k)}$ and $|K_{\boldsymbol{\epsilon}}^{(k)}|$ is its determinant. $K_{\boldsymbol{\epsilon}}^{(k)}$ is given by

$$K_{\boldsymbol{\epsilon}}^{(k)} = Z^{(k)} K [Z^{(k)}]^T, \tag{5.29}$$

with K the covariance matrix of the data noise $\mathbf{N}$.

Up to this point we have found a full multivariate statistical description of the noise $\boldsymbol{\epsilon}^{(k)}$ in the logarithm of the reconstruction at the k-th iteration. We are now interested in the statistical description of the reconstruction $\hat{V}^{(k)}$ itself.

The conditional expected value of $\hat{V}^{(k)}$ follows from equations (5.24) and (5.25), within *Approximation 1*

$$E(\hat{V}^{(k)}|V) = A^{(k)}. \tag{5.30}$$

Given that the logarithm of $\hat{V}^{(k)}$ follows a multivariate Normal law, $\hat{V}^{(k)}$ must follow a multivariate log-normal distribution. Thus we have

$$p(\hat{V}^{(k)}|V) = J(\hat{V}^{(k)})[(2\pi)N|K_{\epsilon}^{(k)}|]^{-1/2} \exp\left[-\frac{1}{2}[\ln(\hat{V}^{(k)}) - \ln(A^{(k)})]^T [K_{\epsilon}^{(k)}]^{-1} [\ln(\hat{V}^{(k)}) - \ln(A^{(k)})]\right],$$

where $J(\hat{V}^{(k)})$ is the Jacobian of the transformation from $\mathbf{Y}^{(k)}$ to $\hat{V}^{(k)}$, given by

$$J(\hat{V}^{(k)}) = \prod_{n=1}^{N} \frac{1}{|\hat{V}^{(k)}|}.$$

Every component of vector $\hat{V}^{(k)}$ follows a univariate log-normal law.
Up to *Approximation 1*, the covariance matrix of $V^{(k)}$ is equal to that of $\boldsymbol{\delta}^{(k)}$. Thus from (5.25) we have,

$$[K_{\boldsymbol{\delta}}^{(k)}]_{mn} = A_m^{(k)} A_n^{(k)} [K_{\boldsymbol{\epsilon}}^{(k)}]_{mn}.$$

An important case is $m = n$ which gives the variance of $V^{(k)}$ components. For that case we have,

$$\text{var}\{\hat{V}_n^{(k)}|V\} = [A_n^{(k)}]^2 [K_{\boldsymbol{\epsilon}}^{(k)}]_{nn}. \tag{5.31}$$

Note that since the variance of $V^{(k)}$ depends on $[A_n^{(k)}]^2$, bright image regions will have high variance while dark regions will have low variance. However, it is not correct to say that the variance is proportional to the square of the mean since $[K_{\boldsymbol{\epsilon}}^{(k)}]_{nn}$ also depends on the object (see equation (5.29)).

Analyzing the asymptotic case, as $k \to \infty$, we can see that

$$Z^{(k+1)} = D^k + [I - C^{(k)}] Z^{(k)} \to Z^{(k)}.$$

Hence, if $C^{(k)}$ is non-singular

$$Z^{(\infty)} = [C^{(\infty)}]^{-1} D^{(\infty)},$$

and from (5.29) and (5.31) we have

$$\text{var}\{\hat{V}_n^{(\infty)}|V\} = [A^{(\infty)}]^2 \sum_m \{[C^{(\infty)}]^{-1} D^{(\infty)}\}_{nm}^2 [HV]_m.$$

We find that the term $[C^{(\infty)}]^{-1}$ is the one that accounts for the large variance -noise- amplification for large iteration values. Therefore imaging systems for which $C^{(\infty)}$ is poorly conditioned will amplify noise more than those for which it is well conditioned.

To summarize, the analysis presented here gives expressions for the mean vector, the covariance matrix and the multivariate probability density function of the reconstructed image. These values depend on the imaged object, the imaging system projection matrix H and the iteration number. If *Approximation 1* is valid, i.e. the noise in the reconstruction is small compared to the mean reconstruction, the reconstruction noise must follow a multivariate log-normal law. Another interesting result is that the variance at each image point depends on the square of the mean image at that point. This way brighter areas present higher variance while the opposite occurs for dark regions. However, the dependence on the mean image is not only quadratic since $K_{\boldsymbol{\epsilon}}^{(k)}$ also depends on the mean image. This also implies a much more local noise than in the case of FBP reconstruction, where the variance tends to be uniform over the reconstructed image.

5.2.2. Extension to OSEM

In the previous section we studied the noise properties of the reconstructed image for the ML-EM algorithm. Now we are interested in extending this analysis to the OSEM algorithm. We would like to confirm whether the description found for noise reconstructed by the ML-EM algorithm can be extended to OSEM and under which conditions.

Soares et. al present in [42] the extension of the work of Barrett et al. [8] for the OSEM algorithm. In [43] they present an experimental verification of the proposed theory. Following the same ideas presented in [8] it can be shown [42] that for the OSEM algorithm the noise in the logarithm of the reconstruction can be written as a linear transformation of the noise in the projection data, i.e. equation (5.28) is still valid for OSEM. The only difference is that matrix $Z^{(k)}$ now depends also on the subset of projections considered for the iteration k.

Below we present a summary of the steps leading to the previous result. Since the deduction is very similar to that described above we will refer to previous comments whenever it is possible.

The OSEM algorithm in component-operation notation can be expressed as

$$\hat{V}^{(k+1)} = \frac{\hat{V}^{(k)}}{s_q} H_m^T \left(\frac{\mathbf{G}}{H\hat{V}^{(k)}} \right), \tag{5.32}$$

where data projections are divided into Q disjoint subsets $\{S_q\}_{q=1}^{Q}$, H_q is the subset-dependent projection matrix

$$(H_q)_{mn} = \begin{cases} (H)_{mn} & q \in S_q \\ 0 & \text{otherwise} \end{cases}$$

and the subset-dependent projection normalization vectors $\{s_q\}_{q=1}^{Q}$ are given by

$$\{s_q\}_{q=1}^{Q} = H_Q^T 1,$$

with 1 a column vector with all its entries equal to one. It is important to remark that in this formulation, one iteration of the OSEM algorithm is a single pass through one subset of the data. The original OSEM formulation [14] considers one iteration as complete pass through all of the subsets.

Taking logarithm on both sides of Equation (5.32), we have the OSEM version of Equation (5.19)

$$\hat{\mathbf{Y}}^{(k+1)} = \hat{\mathbf{Y}}^{(k)} + \ln \left[\frac{1}{s_q} H_q^T \left(\frac{\mathbf{G}}{H\hat{V}^{(k)}} \right) \right], \tag{5.33}$$

where

$$\mathbf{Y}^{(k)} \equiv \ln[\hat{V}^{(k)}], \tag{5.34}$$

and the conditional expectation of $\mathbf{Y}^{(k)}$ is given by

$$E(\mathbf{Y}^{(k)}|V) \equiv \ln(A^{(k)}). \tag{5.35}$$

If we let $\boldsymbol{\epsilon}^{(k)}$ denote the fluctuation of $\mathbf{Y}^{(k)}$ from its mean value

$$\mathbf{Y}^{(k)} = \ln(A^{(k)}) + \boldsymbol{\epsilon}^{(k)}. \tag{5.36}$$

Now taking exponentials on both sides of (5.36) yields

$$\hat{V}^{(k)} = A^{(k)} \exp(\boldsymbol{\epsilon}^{(k)}),$$

which under *Approximation 1* can be written as

$$\hat{V}^{(k)} \simeq A^{(k)}(1 + \boldsymbol{\epsilon}^{(k)}).$$

Back to Equation (5.33), up to *Approximation 1*, the term $\frac{\mathbf{G}}{H\hat{V}^{(k)}}$ can be written as

$$\frac{\mathbf{G}}{H\hat{V}^{(k)}} \simeq \frac{HV}{HA^{(k)}} + \frac{\mathbf{N}}{HA^{(k)}} - \frac{(HV)(H(A^{(k)}\boldsymbol{\epsilon}^{(k)}))}{(HA^{(k)})(HA^{(k)})}, \tag{5.37}$$

Then, defining

$$P_q^{(k)} = H_q^T \frac{HV}{HA^{(k)}}$$

$$\mathbf{W}_q^{(k)} = H_q^T \frac{\mathbf{N}}{HA^{(k)}}$$

$$\mathbf{R}_q^{(k)} = H_q^T \frac{(HV)(H(A^{(k)}\boldsymbol{\epsilon}^{(k)}))}{(HA^{(k)})(HA^{(k)})}.$$

Equation (5.33) rewrites

$$\hat{\mathbf{Y}}^{(k+1)} = \hat{\mathbf{Y}}^{(k)} + \ln\left[\frac{1}{s_q}(P_q^{(k)} + \mathbf{W}_q^{(k)} - \mathbf{R}_q^{(k)})\right] \tag{5.38}$$

$$= \hat{\mathbf{Y}}^{(k)} + \ln\left(\frac{P_q^{(k)}}{s_q}\right) + \ln\left(1 + \frac{\mathbf{W}_q^{(k)} - \mathbf{R}_q^{(k)}}{P_q^{(k)}}\right). \tag{5.39}$$

With *Approximation 1* ($\ln(1+x) \simeq x$), Equation (5.39) becomes

$$\hat{\mathbf{Y}}^{(k+1)} = \hat{\mathbf{Y}}^{(k)} + \ln\left(\frac{P_q^{(k)}}{s_q}\right) + \frac{\mathbf{W}_q^{(k)}}{P_q^{(k)}} - \frac{\mathbf{R}_q^{(k)}}{P_q^{(k)}} P_q^{(k)}.$$

Equating for the random and non-random terms separately gives

$$\ln(A^{(k+1)}) = \ln(A^{(k)}) + \ln\left[\frac{1}{s_q} H_q^T \left(\frac{HV}{HA^{(k)}}\right)\right],$$

and

$$\boldsymbol{\epsilon}^{(k+1)} = \boldsymbol{\epsilon}^{(k)} + \frac{\mathbf{W}_q^{(k)}}{P_q^{(k)}} - \frac{\mathbf{R}_q^{(k)}}{P_q^{(k)}}. \tag{5.40}$$

Equation (5.40) can be rewritten as

$$\boldsymbol{\epsilon}^{(k+1)} = Z_q^{(k)}\mathbf{N}, \quad k = 1, 2, \ldots,$$

with $Z_q^{(k)}$ satisfying the recursion relation

$$Z_{q'}^{(k+1)} = D_q^{(k)} + [I - C_q^{(k)}]Z_q^{(k)}, \quad k = 1, 2, \ldots,$$

with $q = k + 1$, $q' = ((k + 1) \mod Q) + 1$ and $Z_2^{(1)} = D_1^{(0)}$. See Appendix D for the complete expressions of $C_q^{(k)}$ and $D_q^{(k)}$.
The relation between q' and k ensures that the subsets $1, \ldots, Q$ are used cyclically with iterations, i.e. every Q iterations the subsets $1, \ldots, Q$ are used again.

Finally we find for OSEM the same result as for the ML-EM case: under *Approximation 1* the noise in the logarithm of the reconstruction can be written as a linear transformation of the noise in the projection data, with the only difference that the matrix $Z_q^{(k)}$ also depends on the subsets $\{S_q\}_{q=1}^{Q}$. Hence, the same conclusions made for ML-EM can be extrapolated for the OSEM case. In particular, if *Approximation 1* holds, the reconstructed image must follow a multivariate log-normal distribution.

5.2.3. OSEM sensitivity to projection matrix

In the following we present some experiments performed in order to evaluate the sensitivity of OSEM to the projection matrix. Since the projection matrix H is generally unknown and set according to approximations of the camera characteristics and performance, we are interested in evaluating how different the reconstruction result is when varying H. The OSEM version we are using allows to include in H the camera blur, modeled as a Gaussian blur, attenuation and scatter effects. The following experiments show the dependence of the OSEM reconstruction with changes on H due to different camera blur configurations and different attenuation values. Attenuation is assumed to be along the path normal to the camera from the considered pixel. A multiplicative factor equal to $ac = exp(-\sum_{line} \text{attenuation factor})$ is applied to each voxel.

We performed the experiments using the NCAT brain phantom (Figure 4.1). The phantom activity distribution (activity level in each phantom voxel) was set according to the real scan mean activity levels deduced in Section 5.1.6. Specific brain regions were set to activity level values below or above the mean according to the indication of an expert physician. This way a more realistic brain activity distribution is achieved. A parallel hexagonal-holes collimator was simulated. Collimator dimensions (thickness, hole radius, septal thickness) were set according to a real collimator [33]. The detector is a two-layered detector with an energy resolution (FWHM) of 10% and a reference energy of 140 keV. Attenuation effects are simulated and scatter noise is included.

Since we are interested on knowing the reconstruction results dependence on H, the ground-truth will be the reconstruction obtained with a defined parameter set and the results obtained with variations of these parameters will be compared against it. The comparison indicator will be the MSE against the ground-truth image, computed within a mask defined as the non-zero voxels in the latter. We also compute a relative mean error (RME), defined as the mean absolute error over the mean reconstruction value, $\text{RME} = \frac{\text{mean(|gTruth - reconstruction|)}}{\text{mean(reconstruction)}}$. This indicator is useful to have an idea of the relative mean error done on the reconstruction.

Camera blur

Table 5.3 shows the results obtained for different camera blur parameters. σ_1 is the standard deviation of the Gaussian function on the axial plane (the same value in both directions). σ_2 is the standard deviation of the Gaussian function on the coronal plane (the slices direction). The ground-truth image is computed with $\sigma_1 = 3.02$ and $\sigma_2 = 2.69$. The rest of the parameters are left fixed along the runs.

σ_1	σ_2	MSE	RME
1.41	1.41	62.08	0.07
1.80	1.80	42.81	0.05
2.83	2.24	5.19	0.02
3.60	**3.16**	**3.22**	**0.01**
4.60	4.03	179.77	0.11
5.00	4.47	184.23	0.11
5.41	4.92	189.45	0.11
6.71	6.32	416.13	0.29
8.94	8.25	419.57	0.30

Table 5.3: Results for the evaluation of the OSEM reconstruction dependence with the projection matrix H, **camera blur effect**. The ground-truth was generated with $\sigma_1 = 3.02$ and $\sigma_2 = 2.69$. Note that the minimum MSE value is achieved for $\sigma_1 = 3.60$ and $\sigma_2 = 2.16$, the closest to the ground-truth example. The MSE grows rapidly when the standard deviation values deviate from those used in the ground-truth reconstruction.

Attenuation factor	MSE	RME
0.02	117.76	0.71
0.03	61.41	0.43
0.04	**18.18**	**0.19**
0.07	120.11	0.29
0.09	686.7	0.50
0.10	1290.6	0.57
0.11	2242.2	0.64
0.12	3694.8	0.70

Table 5.4: Results for the evaluation of the OSEM reconstruction dependence with the projection matrix H, **attenuation effect**. The ground-truth was generated with an attenuation factor 0.05. Note that the minimum MSE value is achieved for 0.04, the closest to the ground-truth example. The results show a strong variability with the attenuation parameter.

As expected, the minimum MSE value is achieved for $\sigma_1 = 3.60$ and $\sigma_2 = 2.16$, the closest to the ground-truth reconstruction. Moreover, it is interesting to notice that the MSE grows rapidly when the standard deviation values deviate from those used in the ground-truth reconstruction. This would mean that the dependence on H is not negligible and choosing the camera blur parameters imprecisely may lead to incorrect results. The values obtained for RME show that the error in the reconstruction may be considerable large for standard deviation values distant from the real ones.

Attenuation

Following the same procedure as in the previous case we studied the dependence on the attenuation parameter. Table 5.4 shows the obtained results. The ground-truth was generated with attenuation 0.05. The results show a strong variability with the attenuation parameter. Thus, it is important to have a reasonable estimation of the real attenuation coefficient of the object. In the clinical practice, this calibration is performed using transmission scans.

Part II

Application of the SPECT image model to aid the diagnosis of epileptogenic foci in medically refractory epilepsy

Chapter 6

Epileptogenic foci detection

In this chapter we introduce the problem of epileptogenic foci localization, which finds major application in the medically refractory epilepsy cases. A brief summary of the generally used localization methods is presented in Section 6.2. Section 6.3 presents an a-contrario based localization method proposed in [1]. Next, Section 6.4 introduces a new a-contrario localization approach, including a background model based on the SPECT images characterization presented in Section 5.2.1, a combined local-global measurement and a multi-scale detection strategy. Finally, Section 6.5 presents an experimental validation of the proposed method using phantoms and the detection results obtained in 7 real cases. Results are compared against the old a-contrario detection approach and the classical thresholding technique.

6.1. Epilepsy and the problem of epileptogenic zones localization

"Epilepsy is a brain disorder involving repeated, spontaneous seizures of any type. Seizures are episodes of disturbed brain function that cause changes in attention or behavior. They are caused by abnormally excited electrical signals in the brain." [44]

In some cases of epilepsy, the patient does not get better after trying different seizure drugs. Those patients present medically refractory epilepsy. This type of epilepsy may have strong disturbing effects in the daily life of the patient and, in particular, poor neuro-developmental outcomes in children. Brain surgery to remove the abnormal cells causing the seizures is one of the options in these situations. This technique requires a previous precise localization of the epileptogenic zone (EZ), i.e, the brain zone causing the seizure.

Functional neuroimaging techniques, such as PET or SPECT, are useful for the task of EZ localization and the study of the seizure propagation. They are used to analyze the regional cerebral blood flow (rCBF) which presents defined patterns during seizures. At the beginning of the seizure, the EZ presents high levels of rCBF, followed by a rCBF increase in connected circuits. After the initial rCBF peak in the EZ, its rCBF decreases. Hipoperfusion patterns are also found in defined regions, related to the seizure symptoms. The combination of functional studies and the seizure symptoms help the specialist localize the EZ.

In order to perform the SPECT study, a radioactive tracer is administered to the patient by intravenous injection. Brain perfusion SPECT tracers are lipophilic substances with free diffusion across the blood brain barrier that have a long retention time in the brain. Two ^{99m}technetium(^{99m}Tc)-labeled agents are most commonly used: ^{99m}Tc-HMPAO (hexamethylpropylene amine oxime) and ^{99m}Tc-ECD (ethylcysteinate dimer). The tracer distribution is proportional to the rCBF at the moment of injection and stays stable up to 4 to 6 hours. Gamma rays emitted by the tracer are

detected with a gamma camera about an hour after injection. After reconstruction, this produces a 3D image of the rCBF distribution at the moment the patient was injected. An ictal SPECT is obtained when the tracer is injected during a seizure; an inter-ictal SPECT is obtained in-between seizures. Comparing these two SPECT studies helps identifying the possible EZ candidates: regions with high rCBF during the seizure (in the ictal SPECT) that were not high in the normal state (inter-ictal SPECT).

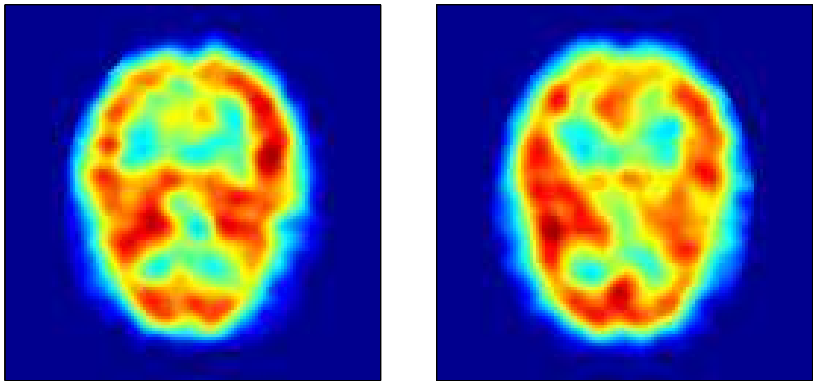

Figure 6.1: One slice of the ictal (left) and inter-ictal (right) SPECT scan of a refractory epilepsy patient. Note that the comparison of the scans to detect the EZ candidates by visual inspection is not simple. The same behavior appears in all slices. Images provided by the Center of Nuclear Medicine of Hospital de Clínicas, Facultad de Medicina, Universidad de la República, Uruguay.

The comparison of the two studies is not an easy task. Visual comparison was initially used, but the images differ too much to allow the detection of punctual activity differences by visual inspection (see Figure 6.1). Then, various techniques have been developed, most of them based in the subtraction of the two scans. Section 6.2 presents a brief summary of the proposed techniques. Among other difficulties, one of the problems of comparing the two studies appears in the case of late injections. When the injection for the ictal study is administered long after the beginning of the seizure, the captured rCBF distribution wont present the EZ among the regions with the highest activity levels. On the contrary, the EZ may appear with low activity level and zones in the propagation circuit of the seizure may appear with the highest levels. In that case, the detection of the zones with highest activity wont include the EZ but connected regions. Moreover, it does not exist an absolute activity threshold defining an EZ. Given the subtraction of the ictal and inter-ictal scans, the EZ or zones in the activation circuit of the seizure, will be among those with highest activity levels. But, what is the threshold differentiating a real detection from a false positive? Where do we set the threshold defining an EZ? What happens if we have the subtraction of two inter-ictal scans? The EZ detection method should be capable of detecting nothing even if the two images differ. In practice, an automatic detection method can only suggest EZ candidates to the specialist, who combining the detection result with a-priori information, may conclude where the seizure originates and which regions belong to the propagation circuits.

6.2. Proposed solutions

As presented in [1], two principal methodologies based on functional neuroimaging techniques have been developed for EZ localization. The first one considers differences in the ictal/inter-ictal comparison which are checked against a healthy normal database. These differences are used to determine the normal expected variation in order to find regions which are outside of normal parameters. To perform this comparison, spatial normalization is first used to wrap images to a SPECT template [2]. This approach is problematic in that comparison against a normal database

is not always valid. It cannot for example be used on children or patients with anatomical lesions.

The second approach compares ictal and inter-ictal images of the same patient. Database information from other patients is not included. The most common method to localize the EZ is to detect hyperperfusion regions on ictal/inter-ictal SPECT subtraction images by thresholding. A global fixed threshold is used, usually proportional to the standard deviation of the gray values in the subtraction image. Although the global thresholding technique has been evaluated and proven successful in EZ localization [3], there are some disadvantages to this method. The global approach is prone to corregistration, even when registration errors are low. Also high dependence on precise masking is observed. Regarding the choice of the threshold value, despite being based on clinical experience, it still lacks a solid statistical basis. Finally, a significant limitation of this approach is that it always detects foci that represent EZ candidates, even in the case of consecutive basal studies of the same subject.

In [1], we proposed a preliminary method that aims to determine detection thresholds from ictal/inter-ictal images of the same patient, in a more rigorous framework. This method is based on the a-contrario theory, a statistical framework developed by Desolneaux et al. [4]. Good results were reported, with better defined activations in the EZ and less amount of false detections than the classical thresholding technique. The proposed solution appears to be more robust to registration errors than thresholding and less sensitive to masking errors. Positive results were also obtained when evaluated on normal subjects.

6.3. A-contrario EZ detection

6.3.1. The a-contrario theory: basic concepts

The a-contrario theory was developed by Agnes Desolneux, Lionel Moisan and Jean-Michel Morel [4] in the late nineties. This theory considers the Gestalt grouping laws (color, shape, vicinity, etc) to determine the presence of a structure as a "strange" event under a randomness hypothesis. The Helmholtz principle formalizes this concept. It states that we perceive no structure in a uniform random image, in other words, "we immediately perceive what could not happen by chance". Figure 6.2 exemplifies this phenomenon. Figure 6.2a shows 100 uniformly distributed random points. This is a uniform random image and indeed we perceive no structure. Figure 6.2b shows the same random points and 34 additional aligned points. Now we perceive the points alignment, which cannot happen by chance in the random image (i.e. under the randomness hypothesis).

Assume that the atomic objects $O_1, \ldots, O_n$ are present in an image and that k of them share a common feature (e.g. same color, orientation, position). The following question arises: is this common feature happening by chance or is it significant enough to consider that the group the objects $O_1, \ldots, O_k$ share some common relation? To answer this question we can think of how would it be the feature distribution among the objects if it had been randomly and uniformly assigned. Then, answer the question: is the current configuration probable under a hypothesis of randomly assignment of the feature? If the answer is no, that proves a-contrario that a Gestalt grouping process is at play, i.e. the configuration could not happen by chance and we perceive a meaningful event. Desolneux et al. introduce in [4] the concept of ϵ-meaningful event,

Definition 1:

"*We say that an event that is ϵ-meaningful if the expectation of the number of occurrences of this event is less than ϵ under the a-contrario random assumption. When $\epsilon \leq 1$, we simply say that the event is meaningful.*"

This definition gives a generic criterion to determine the meaningfulness of an event. However,

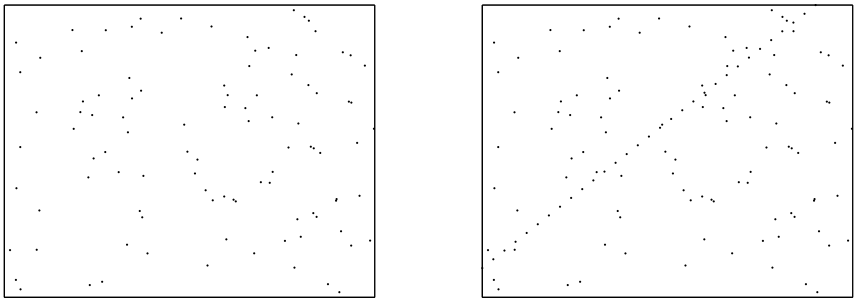

(a) (b)

Figure 6.2: According to the Helmholtz principle we perceive non casual alignments as large deviations from randomness. On the left we have an image of 100 uniformly distributed random points. No alignments are perceived. On the right 34 aligned points were added. The alignment is perceived as it could not have happened by chance under the uniform distribution.

an adequate a-contrario model (randomness hypothesis) must be defined in order to apply it in different situations. Linking Definition 1 and the Helmholtz principle, we find that if the latter is true, we perceive events if and only if they are meaningful in the sense of Definition 1.

If we want to find the meaningfulness of the event "*k out of n objects sharing the same feature*" according to Definition 1, we need to find an upper bound for the expected number of occurrences of the event under the a-contrario assumption. The expected number of occurrences of the event under the a-contrario assumption is called number of false alarms (NFA), since under the random assumption no occurrences of this event should happen. The NFA of an event measures how meaningful the event is. The smaller the NFA the more meaningful the event. The NFA is defined [4] as the product of the probability of occurrence of the event under the a-contrario model (PFA, probability of false alarm) and the number of all possible configurations of the searched gestalt, i.e. the number of all of the forms in which we could find the searched configuration.

$$\text{NFA} \triangleq N_{test}\text{PFA}. \tag{6.1}$$

Since the NFA is an upper bound on the expected number of false alarms, according to Definition 1, an event for which $\text{NFA} \leq \epsilon$ is ϵ-meaningful.

6.3.2. Application to EZ detection

The a-contrario EZ localization algorithm proposed in [1] is based on the one presented by Grosjean and Moisan [45] for spot detection in 2D textured backgrounds. By spot we understand a meaningful deviation from gray values in a certain neighborhood, whether positive (bright spot) or negative (dark spot). No particular shape, neither defined edges, are assumed for the spots. The method defines an a-contrario model for the ictal/inter-ictal subtraction image, and detects bright spots contradicting the model, i.e. spots with a gray level too high to occur under the a-contrario model. Those bright spots are the EZ candidates. As seen in the previous section, the a-contrario model is a statistical model that describes typical configurations where the searched structure is not present. In this case, the a-contrario model, also called background model, is white Gaussian noise. For each SPECT scan, the model is defined by the random 3D image

$$(H_0): \quad U = \mu + \sigma N, \tag{6.2}$$

where μ and σ are real parameters and N is a 3D white Gaussian noise image (with zero mean and unit variance). It is important to note that in the a-contrario framework, background models

are not required to be fully realistic. However, it is important to ensure that if the image fully complies with the background model, no structures are detected.

The application of the a-contrario theory also requires a measurement, made on the structures to be detected, to measure the meaningfulness of the structure under the a-contrario model. Let us consider the measurement $m \in \mathbb{R}$. If the searched structure is more significant as m takes high values, the weigh of significance is given by the probability $\text{PFA} = P(M \geq m)$, where m is the observed measurement and M is the random variable corresponding to the distribution of m in the background model. The NFA can then be computed according to Equation (6.1). This ensures that if the image verifies the background model hypothesis, the average number of ϵ-meaningful bright spots detected by chance is less than ϵ [4].

At each potential location two measurements are made: one in the ictal scan, m_1, and the other in the inter-ictal scan, m_2. Bright spots are detected as significantly high values of $m = m_1 - m_2$, which correspond to high contrast between the ictal and inter-ictal scan at the tested position. They can be also seen as bright spots in the subtraction image. Let u_{ictal} and $u_{interictal}$ be 3D images. The linear measurements can be expressed as

$$m_1(x, y, z) = \int_{\mathbb{R}^3} u_{ictal}(x - p, y - q, z - r)s(p, q, r)dpdqdr, \tag{6.3}$$

$$m_2(x, y, z) = \int_{\mathbb{R}^3} u_{interictal}(x - p, y - q, z - r)s(p, q, r)dpdqdr, \tag{6.4}$$

with s a normalized ellipsoidal measurement kernel, where the ellipsoid radii are related to the 3D image resolution. Let $M_i(x, y, z)$, $i = 1, 2$, be the random variable representing the measurement value $m_i(x, y, z)$. In order to compute the PFA, we need to know the distribution of $M_i(x, y, z)$ in the background model. From Equations (6.2), (6.3) and (6.4) it follows

$$M_i(x, y, z) = (U * s)(x, y, z),$$

and thus M_1 and M_2 are both colored Gaussian noise. Since the distribution is stationary and the measurements are invariant to translations, the detection thresholds will be exactly the same at each position. Thus we can shorten the notation

$$M_i = U * s = \mu + \sigma \langle N, s \rangle ,$$

where $< ., . >$ denotes the inner product. It can be shown [45] that $\sigma \langle N, s \rangle$ is normally distributed with zero mean and standard deviation $\sigma ||s||$. Then $M_i \sim N(\mu, \sigma^2||s||^2)$ and $M = M_1 - M_2$, subtraction of two independent Gaussian variables, satisfies $M \sim N(0, 2\sigma^2||s||^2)$. Finally, the NFA is computed as

$$\text{NFA} = |T|P(M \geq m) = |T| \, \Phi_c \left(\frac{m_1 - m_2}{\sigma \|s\|} \right) \tag{6.5}$$

$$= |T| \, \Phi_c \left(\frac{(m_1 - m_2)\sqrt{2\pi r_1 r_2 r_3}}{\sigma \sqrt{3}} \right), \tag{6.6}$$

where $|T|$ is the number of tested locations, r_i are the ellipsoid radii and Φ_c denotes the tail of the Normal distribution.
The NFA values are computed in a defined grid T. All spots centered in voxels having an $\text{NFA} \leq \epsilon$ as considered meaningful detections and therefore EZ candidates. The a-contrario threshold ϵ is set to 1, in order to have at most one false detection.

One of the main advantages of the a-contrario approach is that, unlike the classical thresholding, the threshold is not arbitrary but depends on the chosen model. In this case, the model

parameter to be estimated is σ. In [1], σ is computed as the gray level variance of the inter-ictal scan inside a brain mask. This approach has an important drawback, the resulting threshold is too restrictive and in some cases the detections are very few or even no detection is found in cases of know EZ presence. The threshold is too restrictive because computing the variance globally in the inter-ictal scan includes gray level variations that are not present in the subtraction image. For example, two regions of different gray level that match in the ictal and inter-ictal scans, will be mapped to zero in the subtraction image. Thus, they have different value (contribute to the variance computation) in the inter-ictal scan but they are equal in the subtraction image. Finally, using the variance of the inter-ictal scan to model the gray level variation of the subtraction image may be too restrictive.
In the following section we present a new a-contrario detection approach, based on a new background model which better suits the SPECT images characteristics. The new method aims to overcome the shortcomings of the present approach, avoiding the rule out of true EZ at the cost of increasing the false positives.

6.4. A-contrario EZ detection: new approach

The SPECT images characterization presented in Section 5.2.1 inspires the proposal of a new background model for the a-contrario EZ localization. A new detection strategy is also proposed, with a measurement combining global and local information and including a multi-scale approach.

6.4.1. The new model

Scan model

In Section 5.2.1 we presented the characterization of ML-EM reconstructed tomographic images proposed by Barrett et al. [8]. The presented analysis gives expressions for the mean vector, the covariance matrix and the multivariate probability density function of the reconstructed image $\hat{V}^{(k)}$, given the scanned object V. The reconstructed images in our case are the ictal and inter-ictal SPECT scans. We recall here the form of the probability density function

$$p(\hat{V}^{(k)}|V) = J(\hat{V}^{(k)})[(2\pi)N|K_\epsilon^{(k)}|]^{-1/2} \exp\left[-\frac{1}{2}[\ln(\hat{V}^{(k)}) - \ln(A^{(k)})]^T[K_\epsilon^{(k)}]^{-1}[\ln(\hat{V}^{(k)}) - \ln(A^{(k)})]\right]. \quad (6.7)$$

This function depends on the object being scanned V, the imaging system projection matrix H and the iteration number of the ML-EM algorithm k. If the introduced approximation is valid (the noise in the reconstruction is small compared to the mean reconstruction), the reconstruction must obey a multivariate log-normal law. Therefore, under this approximation, the **logarithm of the scan** obeys a **multivariate normal law**. Besides, it was found that the variance at each image location depends on the mean image value at that point, thus the variance is spatially non-stationary, contrarily to what was wrongly assumed in [1]. The spatial non-stationary nature of the mean image values (which implies that of the variance) is caused by the non-homogeneous characteristics of the object being scanned, in this case, the brain. The brain matter is not homogeneous and therefore the emission levels at different positions differ.

The previous result models the reconstructed image for a given scanned object V. Different objects lead to different parameters of the probability density function given by (6.7). In our case, the scanned object is the brain with the particular radiotracer distribution at the moment of injection, and therefore the particular rCBF pattern at that moment. Different rCBF patterns give different examples of V. For this reason, two functional images of the brain will never be equal, even if both of them are taken in basal state. It is impossible to obtain two equal inter-ictal scans, since the rCBF distribution in the brain depends on the brain activity which cannot be exactly

reproduced. If we compare two inter-ictal scans of the same patient, we can see a basic structure common to both images, and differences mostly in the borders of the inner shapes. See Figure 6.3 for an example. We may describe this variability through a random process $\mathbf{V}$ representing the physiological behavior of the brain. A realization of this process is a given rCBF distribution, i.e. an example of V. Then, each reconstructed image obtained form V can be modeled according to Equation (6.7).

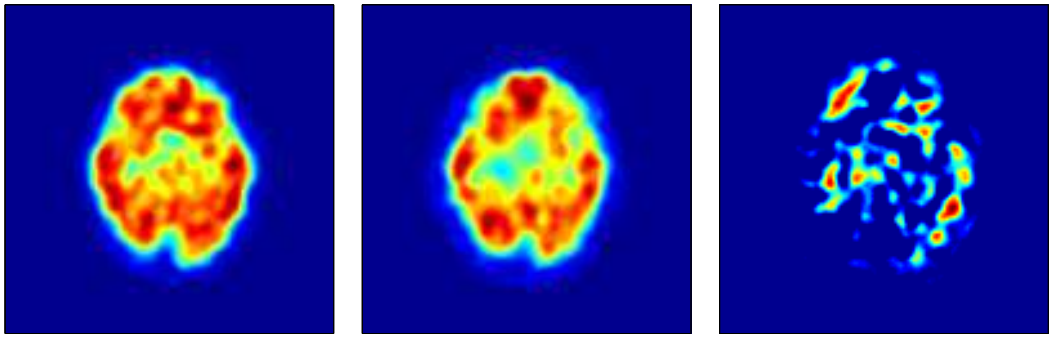

Figure 6.3: **Left:** One slice of two inter-ictal SPECT scans of the same patient. **Right:** Corresponding slice of the subtraction of the two scans. Note the structure common to both scans and the differences in the subtraction image. Images provided by the Center of Nuclear Medicine of Hospital de Clínicas, Facultad de Medicina, Universidad de la República, Uruguay.

We may now raise the question about the form of the probability density function $p(\hat{V}^{(k)})$, that is, give a more general model which includes the variability of V and gives a probability density function valid for all V. For that purpose we would need information about the physiological behavior of the brain and how the different regions vary. Because we do not have access to that information and such a model should be quite complicated, we chose to keep the dependence on V and incorporate the idea of functional variability in a posterior analysis. This variability needs to be considered for the EZ detection task since the difference between the inter-ictal and ictal scans are not only the EZ but also the inherent variabilities of the functional differences between the two studies.

Subtraction image model

Because we are interested in finding meaningful differences between the ictal and inter-ictal scans, we will work with the subtraction image. As mentioned in Section 6.3.2, the background model for the a-contrario detection using the subtraction image is given by the subtraction of two inter-ictal scans. The *normal* variability of the scans is that of the subtraction of two inter-ictal scans, since in that case we are sure that no EZ is included. If we had a large dataset of inter-ictal scans of the patient, we could make a statistical model of the *normal* variability. That variability is caused by the physiological process generating different V samples. Then, the EZ candidates can be found as deviations from the normal behavior in the inter-ictal/ictal subtraction. However, this is not the case and in general only one inter-ictal scan is available. For this reason, we are forced to use the inter-ictal/ictal subtraction image to characterize the background model. We make the assumption that the number of voxels belonging to EZ is small with respect to the brain volume and therefore does not bias the results. If we consider the subtraction of the logarithm of the scans, each voxel of the subtraction image is the difference of two independent normally distributed random variables, and therefore also normally distributed. They are independent since the inter-ictal and ictal scans are obtained at different moments. The voxels will remain spatially correlated and non-stationary in the subtraction image. A correlation study was performed in 8 real scans which showed that correlation decays to almost zero within a neighborhood of radius $3 \times 3 \times 1$ pixels (each of the 3D components). This correlation behavior was verified to be spatially

stationary. Part of the structure of the images is lost with the subtraction. We can see it in Figure 6.3. In spite of this, the subtraction image remains spatially non-stationary since the borders of the inner structures differ in each scan and give rise to spatially non-stationary gray levels (and correspondingly non-stationary variance). Given that the non-stationarity is due to the non-homogeneous nature of the brain and the inherent functional variabilities, it seems reasonable to suppose local stationarity. The brain matter changes smoothly and the structure is mostly kept in different realizations of V. Thus, we model the subtraction of the logarithm of the scans as non-stationary, colored Gaussian noise. The marginal distribution of each voxel is also normal, with different parameters for each voxel. In the following we will refer to the subtraction of the logarithm of the ictal and inter-ictal scan as subtraction image.

6.4.2. The measurement

The second step in the a-contrario detection process is to precise the measurement to be used for detection. As previously mentioned, we will use a combined local-global approach. The local approach allows us to find locally meaningful regions, i.e. regions meaningfully bright with respect to their context. The EZ does not have a specified shape. However, they are usually spot-like regions. On the other hand, the global approach is essential for detection, since the global comparison of gray level values is what let us identify feasible EZ candidates. The local measurement identifies regions too bright for the context, which does not mean being globally bright and therefore an EZ candidate. An EZ must be bright with respect to the rest of the volume.

Global measurement

As in the original version of a-contrario detection, the global measurement M_G will be the mean gray level value in an elliptical neighborhood centered on the tested voxel

$$m_G(x, y, z) = \int_{\mathbb{R}^3} u(x - p, y - q, z - r)s(p, q, r)dpdqdr, \tag{6.8}$$

with u the subtraction image and s the elliptical kernel. In order to evaluate whether the measurement value m_G is meaningful or not, we must answer the question: under the a-contrario image model, which is the probability for the measurement variable M_G to be higher than the observed measurement value m_G? If that probability is below a certain threshold we will say that the tested region is meaningfully bright. To compute that probability, we should know the probability density function of the gray level values in the subtraction of two inter-ictal images. To be more precise, we should know the probability density function of the measurement image, i.e. the convolution of the subtraction of the inter-ictal scans and the measurement kernel. From the image model analyzed above, among other things (projection matrix, ML-EM iteration), the gray level m_G at a given voxel in the measurement image depends on the realization of the physiological process for each scan, V_1 and V_2, and on the position on the scan x (non-stationarity due to inhomogeneity of the brain). The probability of M_G to be greater than m_G verifies

$$P(M_G \geq m_G) = \int_{m_G}^{\infty} \dots \int p(M_G|V_1, V_2, x)dV_1dV_2dxdM_G.$$

To correctly estimate $P(M_G \geq m_G)$ we should have various realizations of V_1 and V_2, which is not the case. We only have one ictal and one inter-ictal scans. Thus, we propose to use the empirical histogram of the gray level values of the measurement image. The Gaussian model cannot be used here since all the samples come from Gaussian distributions of different parameters. The non-stationarity of the proposed Gaussian model invalidates its usage in a global approach. However, we will use it for the local measurement model, since with the hypothesis of local stationarity, we can characterize the model locally.

Local measurement

The local measurement m_L is also given by Equation (6.9).

$$m_L(x,y,z) = \int_{\mathbb{R}^3} u(x-p, y-q, z-r)s(p,q,r)dpdqdr, \tag{6.9}$$

with u the subtraction image and s the elliptical kernel. Once again we rise the question: under the a-contrario image model, which is the probability for the measurement variable M_L to be higher than the observed measurement value m_L? For the local measurement, the colored Gaussian model is valid since we can assume local stationarity for the mean and variance values. We assume that in a neighborhood of the tested voxel, all samples are identically distributed. The measurement image in this case (the given neighborhood) can also be modeled as colored Gaussian noise, since it is the convolution of colored Gaussian noise with a measurement kernel. Thus, the voxels in the neighborhood are used to estimate the parameters of the model. Therefore we have

$$P(M_L \geq m_L) = \Phi_c\left(\frac{m_L - \mu_L}{\sigma_L}\right),$$

with Φ_c the tail of the normal distribution, μ_L and σ_L the mean and variance of the considered neighborhood.

Combined measurement

Since the idea is to test both aspects, global and local at the same time, the measurements are combined in a unique measurement. Despite the measurements are not independent, we can say that if the global measurement distribution is computed based on a region much larger than that of the local measurement, both probabilities can be considered independent. Note that if the local probability is computed based on a region much smaller than the global one, knowing that a region is locally meaningful does not say much about its global meaningfulness. On the other hand, saying that a region is globally meaningful does not imply that that the region is meaningful on its context (think of a large bright constant region). Finally the combined measurement is given by

$$pfa = pfa_G.pfa_L.$$

6.4.3. Multi-scale approach

Because the EZ may present different sizes, a multi-scale approach is mandatory. The combined measurement is computed for 3 different scales. Each scale defines the radii of the elliptical measurement kernel s and the size of the neighborhood for the local measurement. At each tested voxel, the NFA for each scale is computed using equation (6.1). Then, the most meaningful scale, i.e. the one corresponding to the minimum NFA is chosen.

6.4.4. Number of false alarms

In [1], as in [45], the number of false alarms is computed as the product of the probability of false alarms times the total number of tested voxels. For the new a-contrario detection method, the total number of tested voxels is the summation of the tested voxels for all scales. This definition, despite valid, is not the only option. Strictly speaking, according to the Proposition 2 presented by Grosjean et al. in [45], the function

$$NFA(i, x_i) = n_i P(X_i \geq x_i),$$

with $(X_i)_{1\leq i\leq N}$ is a set of random variables and $(n_i)_{1\leq i\leq N}$ a set of positive real numbers, is a NFA as soon as

$$\sum_{i=1}^{N} \frac{1}{n_i} \leq 1.$$

In particular, the function is a NFA if $n_i = N$ for all i, which is the case in the method proposed in [1].

In a multi-scale approach it seems reasonable to use differentiated NFA thresholds for the scales. We perform more tests of the smaller scale than that of the larger scale. Thus, we are increasing the probability of finding a meaningful spot on the smaller scale. On the other hand, the probability of finding spots of different sizes depends on the image characteristics: scales closer to that of the image model are more probable than others.

Burrus et al. introduce in [9] an innovative methodology to estimate the expectation of the number of false alarms by mixing analytical computations and Monte-Carlo simulations. The basic idea is to simulate various independent realizations of the background model and then perform the detection method on the simulated images. Under the background model hypothesis, all the detections are false positives. Thus the average number of detections can be taken as an estimation of the expected value of false alarms. Then the multiplicative constants n_i are set so that to have less than ϵ false alarms. At each iteration, a detection is found when it verifies

$$P(X_i \geq x_i) \leq \frac{\epsilon}{n_i} = \delta_i.$$

The procedure is performed iteratively until convergence of the δ_i values. In this manner, the a-contrario threshold δ_i is set automatically and ensures ϵ-reliability. Moreover, the proposed method allows to consider the differentiated computation of the NFA threshold for different *categories*. Categories are associated to differentiated tests, for example, the different scales in the multi-scale approach. In [9], the authors propose to use the iterative procedure to estimate a different threshold for each category. They argue that if an algorithm is $\frac{\epsilon}{K}$-reliable for each of the K tested categories, then it is ϵ-reliable in the complete test. The proof is straightforward using the linearity of the expectation. If an algorithm makes less than $\frac{\epsilon}{K}$ errors in average for each category, then it globally makes less than ϵ errors in average.

In the present work we combine the previous two approaches for the NFA thresholds computation. For each scale, we compute the NFA as the product of the PFA times the number of tested voxels for that scale. Then we set $\epsilon = \frac{1}{K}$ to perform the meaningfulness tests. Using the same expectation linearity argument presented by Burrus et al., if we ensure that the algorithm makes less than $\frac{\epsilon}{K}$ errors in average for each category, then it globally makes less than ϵ errors in average. On the other hand, it was shown in [45] that the function NFA $= N_{test}$PFA is a valid NFA when N_{test} is the number of tested voxels, which is therefore valid for the tests performed at each scale.

We found it not feasible in this case the application of the method of Burrus et. al as presented in [9] since we find it unworkable to simulate samples of non-stationary noise according to the SPECT scans subtraction characteristics. As previously mentioned (c.f. Section 6.4.1) for that purpose we should have a statistical model of the spatial variation of the gray levels of the subtraction of inter-ictal scans of the patient. A dataset of inter-ictal scans of the same patient would be needed. The idea of mixing scans of different patients to make the model was previously presented[2], but does not count with wide acceptance in the medical community since anatomical differences between patients or even age (there are no databases for children) are non-negligible drawbacks. Because the option of having several inter-ictal scans of the patient is usually not feasible, we find it unworkable to develop a statistical model of the spatial variation of gray level values and generate background model samples.

6.5. Experiments

The previously described a-contrario detection method is tested on phantoms and on a dataset of 7 patients with medically refractory epilepsy.

6.5.1. Simulations

The evaluation of the proposed method using phantoms is performed in first place as a sanity-check of the proposed approach. It intends to verify that, under controlled conditions, the method performs as expected. Detection performance is also compared against the previous a-contrario detection approach [1] and the classical subtraction method [3].

Experiments are performed using the NCAT brain phantom (see Figure 4.1). The phantom basal activity distribution (activity level in each phantom voxel) is set according to the indication of a specialist. From that basal configuration, various basal phantoms are generated uniformly varying the activity levels with a variation range of 10%. In order to simulate different seizures, the activity levels in specific regions are increased according to the specialist indication. These regions are chosen so that to be representative of real seizures. Three seizure configurations are defined, with increasing level of complexity, which we will refer to as *phantom 1*, *phantom 2* and *phantom 3*. The ictal phantom for each patient is obtained firstly varying the activity levels on its basal phantom (uniform variation 15%) and then increasing the activity levels of the corresponding regions.

The SPECT sinograms of the phantoms are obtained using an utility of the OSEM package used for reconstruction. This package allows not only to generate the reconstructed image from projections, but also generate projections from a given phantom. The simulated effects are the Poisson nature of photon emission, camera blur and attenuation. The SimSET tool was not used in this case for time constraints, but it would be interesting to perform the analysis using this tool and incorporate other non-idealities of the acquisition process. The reconstruction is performed using the OSEM algorithm.

It is important to notice that this evaluation does not take into account alignment issues that always appear in real cases. Ictal and basal scans are never perfectly aligned in real cases as they are in this test. In previous evaluations [1, 46], the a-contrario detection approach introduced in [1] was shown to be robust to alignment problems as opposed to the classical subtraction method which appears to be quite sensitive to alignments mismatch. The present sanity-check does not intend to verify this aspect for the new a-contrario detection approach. However, it would be interesting to include it in future evaluations. Despite not being strictly verified, given the similarities to the old approach, we expect the new method to have a similar behavior in this sense.

Phantom 1 This case corresponds to the activation of the left hippocampal formation. Four activation levels are tested: 30%, 50%, 70% and 100%. For the 30% activation, the a-contrario detection approach detects the EZ but not in all slices. It presents some false positives, which can be seen in the subtraction image as highly activated regions. Figure 6.4 shows the detection results for this case. In white are the correctly detected regions, in yellow the false negatives and in red the false positives. The old a-contrario approach finds no detections in this case. Results for the subtraction method are shown in Figure 6.5. It presents almost no false negatives but a large number of false positives (more false positives appear in the slices not displayed). For the 50% activation case, the a-contrario approach increases the number of correct detections without a major increase on false positives. See Figure 6.6. The old a-contrario approach still has no detections. The subtraction method has no false negatives but the detection is quite imprecise. See Figure 6.7. A similar behavior is seen for the 70% activation case. The a-contrario approach continues to increase the correct detections, while the old a-contrario approach has no detections.

See Figures 6.8 and 6.9. For the 100% activation case, the a-contrario approach has almost no false negatives nor false positives. The old a-contrario approach behaves similar to the new approach, but with a more precise detection (less false positives). The subtraction method continues to be imprecise. See results in Figures 6.10, 6.11 and 6.12.

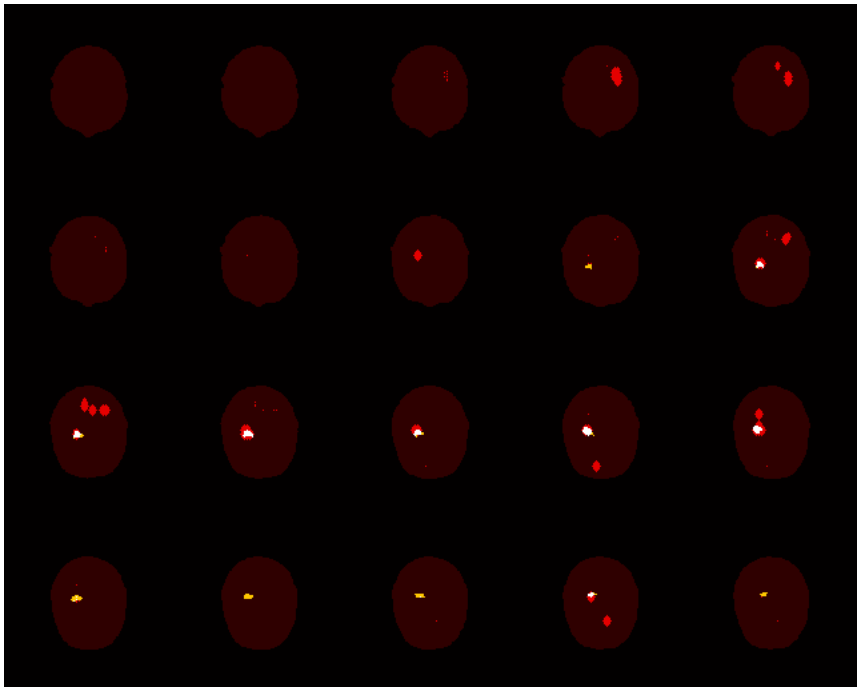

Figure 6.4: **Phantom 1 - Activation level: 30%, Method: a-contrario**. **White:** Correct detections. **Yellow:** False negatives. **Red:** False positives. The EZ is detected but not in all slices. It presents some false positives which can be seen as highly activated regions in the subtraction image.

Phantom 2 This case corresponds to the activation of the left hippocampal formation and the left parahippocampal gyrus. Three activation levels are tested: 20%, 40% and 60%. Neither the new nor the old a-contrario approaches have correct detections for the 20% activation approach. The new approach has one false positive. The substraction method detects a small region of the EZ and presents a large number of false positives. See Figures 6.13 and 6.14. The detectability of the a-contrario approach is increased for the 40% case, but it still does not find most of the EZ. The substraction method has no false negatives but increases the number of false positives. See Figures 6.15 and 6.16. For the 60% activation case, the a-contrario approach detects most of the EZ with a small number of false positives. The substraction approach detects all the active regions but very imprecisely. See Figures 6.17 and 6.18. The old a-contrario method yields no detections in any of the cases.

Phantom 3 This case corresponds to the activation of the left hippocampal formation (30%), left uncus (30%) and the deactivation of the right hippocampal formation (30%). It represents a more complex seizure, including the hipoperfusion of the right hippocampal formation. A similar behavior as in the previous cases is found for this configuration. The a-contrario method detects the EZ, but not completely. It presents a small number of false positives. The substraction approach has no false negatives but a very imprecise detection. The old a-contrario approach has no detections.

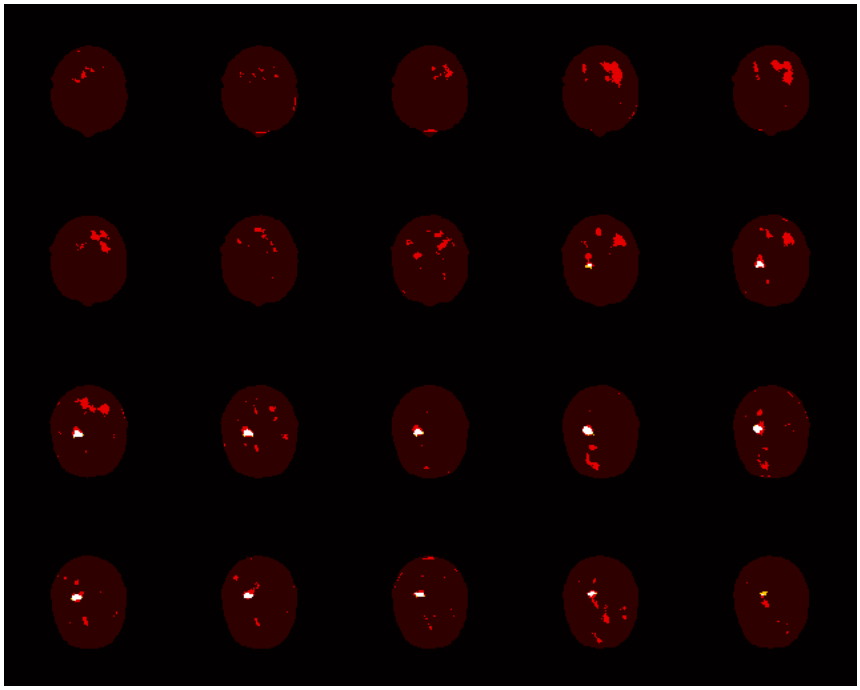

Figure 6.5: **Phantom 1 - Activation level: 30%, Method: classical substraction**. **White:** Correct detections. **Yellow:** False negatives. **Red:** False positives. The method presents almost no false negatives but a large number of false positives (more false positives appear in the slices not displayed).

Remarks The new method appears to perform as expected under controlled conditions. In certain cases, mostly of low activation levels, it presents false negatives. This is highly undesirable for the EZ localization application. However, it is important to highlight that in the real cases experiments that will be presented in the following section, the EZ is always among the detected candidates. Notice that despite the phantoms were set in order to approximate real seizures, activation differences between ictal and inter-ictal scans of 80% to 100% were found in various of the real cases. False positives are not a problem since they are a controlled number and in general do not affect the precision of EZ localization. The detectability threshold of the a-contrario approach seems to have been reduced. The EZ is correctly located for activation levels lower than that of the old a-contrario approach. Thus the new approach appears to be more sensitive than the previous one. In [46] the authors found a minimum activation threshold of 40% for the old a-contrario method. We found a different result for the tested configuration. However, beyond absolute values, the interesting point to highlight is the decrease of the detectability threshold for the new method. Moreover, it is important to remark that the good results obtained by the substraction method are highly influenced by the perfect alignment of the scans. As previously mentioned, the substraction method is prone to alignment artifacts.

6.5.2. Real cases

The previously described a-contrario detection method was tested on a dataset of 7 patients with medically refractory epillepsy (1-34, 3 male). Data was provided by the Center of Nuclear Medicine of Hospital de Clínicas, Facultad de Medicina, Universidad de la República. The location of the EZ was defined by consensus in the Epilepsy Surgery Program after pre-surgical evaluation. For each patient, two scans are available: an inter-ictal and an ictal SPECT scans. The pre-processing of the scans includes:

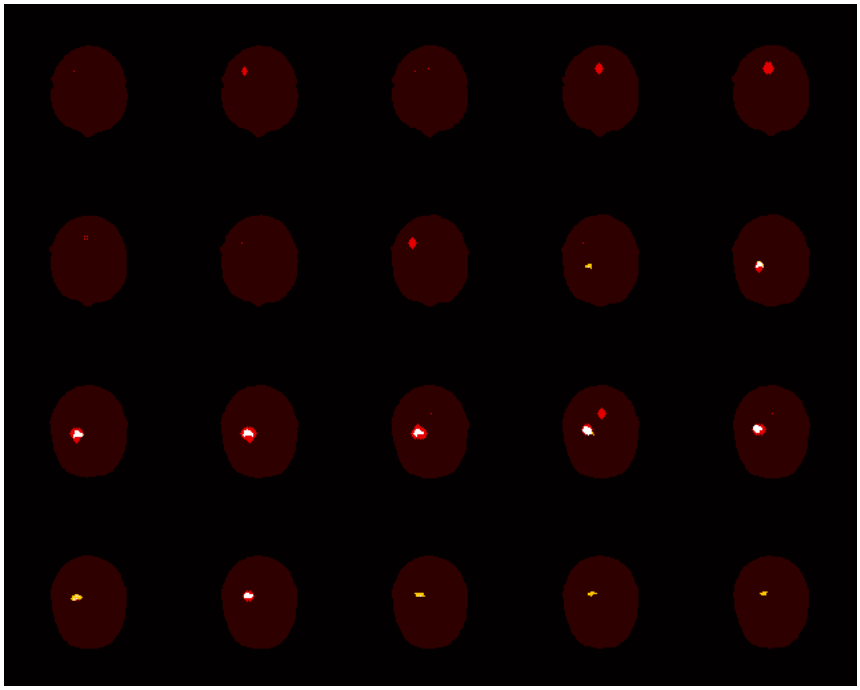

Figure 6.6: **Phantom 1 - Activation level: 50%, Method: a-contrario**. **White:** Correct detections. **Yellow:** False negatives. **Red:** False positives. For the 50% activation case, the a-contrario approach increases the number of correct detections without a major increase on false positives.

1. **Realignment:** both scans are realigned with each other using the realignment utility of the SPM software [47].

2. **Masking:** a mask of the brain is generated, based on the empirical histogram of the gray level values.

3. **Normalization:** Each scan is normalized to have constant total number of counts. In this manner, each voxel represents a relative number of counts with respect to the total counts. This allows to compare the scans even if the total number of counts differs from differences in the radiotracer concentration at the moment of injection, the time elapsed between injection and acquisition, etc.

The subtraction image is then computed and the a-contrario detection method is applied. The a-contrario thresholds are adjusted using the method described in Section 6.4. The measurement kernels are elliptical 3D kernels and three scales are tested: $[(2,1,1),(3,2,1),(4,3,1)]$, with (r_a, r_b, r_c) the kernel radius in each component, and $[(3,2,1),(4,3,1),(5,4,1)]$ the corresponding local measurement patch sizes.

The results are compared against those obtained using the old a-contrario approach and those obtained by the specialist using the substraction method. Results evaluation was conducted jointly with an specialist of the Center of Nuclear Medicine of Hospital de Clínicas. In all cases, the EZ area was among the detected EZ candidates. In 6 of the 7 cases, the results obtained by the new a-contrario detection approach are very similar to those obtained by the old a-contrario approach. Most detections match in position, varying in some cases on intensity and size. In [1], these 6 real cases were analyzed and the results of the old a-contrario approach were compared against those of the substraction method. The a-contrario method, in both the old and new approach, shows better defined activations in the EZ and fewer false detections than the substraction method. It is

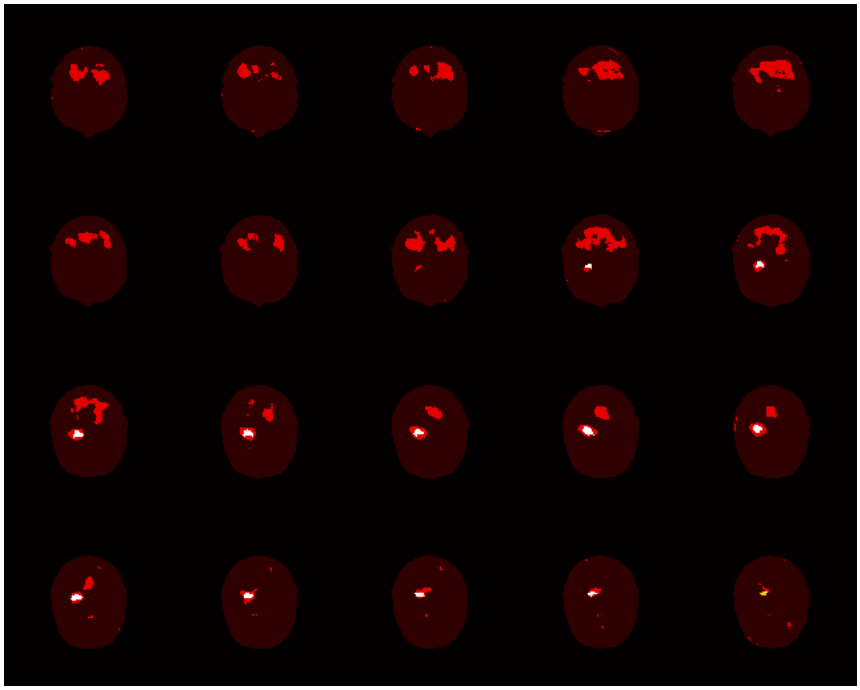

Figure 6.7: **Phantom 1 - Activation level: 50%, Method: classical substraction**. **White:** Correct detections. **Yellow:** False negatives. **Red:** False positives. Similar behavior as in the 30% activation case, with an increased number of false positives.

also more robust to alignment errors between the scans and less sensitive to masking errors than the latter. Among the differences between the results of the two a-contrario methods we highlight:

- Reduction of false positives. Despite the previous a-contrario approach already had very few false detections, this number diminishes in some of the studied cases (see Figures 6.21 and 6.22).
- Emergence of new detections that belong to the seizure activation circuit. This aspect is remarkable since the highly restrictive thresholding of the old a-contrario method gives *clean* images (low number of false detections) which are not in accordance with reality. The perfusion circuits are complex and several brain regions should show side effects of the seizure (see Figures 6.23 and 6.24). In the studied cases, the new a-contrario approach increments the detection of zones in the propagation circuit without increasing the false positives.
- The intensity level of the EZ. Some differences were found on the intensity level of the detections. In most cases the EZ appears with higher intensity in the new a-contrario approach (see Figures 6.25 and 6.26). In one case, we find the opposite behavior (see Figures 6.27 and 6.28).

The biggest difference appears in one of the cases where the old a-contrario approach finds no detection while the new approach does. Despite showing false detections, the new method attains the EZ detection.

Remarks If we compare the performance of both a-contrario methods, the major difference is given by the restriction level of the threshold. As we previously stated, the old a-contrario approach sets a too restrictive threshold, which allows *clean* images -desirable up to certain point- but which is prone to false negatives and even no detections in cases of known EZ presence. Having a low

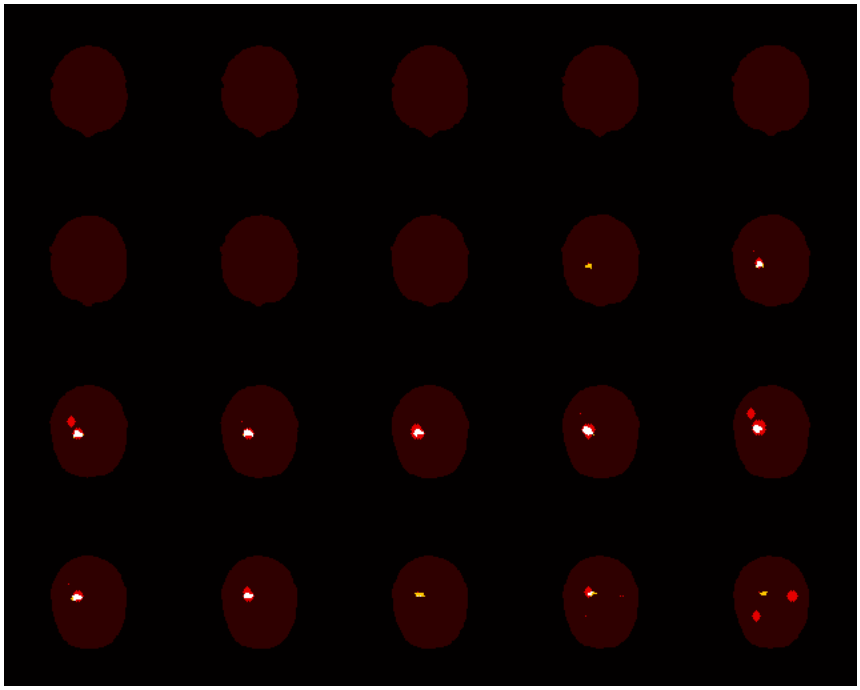

Figure 6.8: **Phantom 1 - Activation level: 70%, Method: a-contrario**. **White:** Correct detections. **Yellow:** False negatives. **Red:** False positives. The a-contrario method continues to increase the number of correct detections without increasing false positives.

number of false negatives is critical in this application. It is preferable to give a larger number of candidates, that can be evaluated by the specialist, than discarding most detections with the aim of automatically finding the EZ. The inherent complications of the problem, described in Section 6.1, strongly justify the selection of a less restrictive threshold. The same behavior had been verified in the experiments using phantoms. In the new approach, the threshold on the activation level is reduced. Moreover, the new approach has shown to have the quality of increasing the valid detections without considerably increasing the false positives.

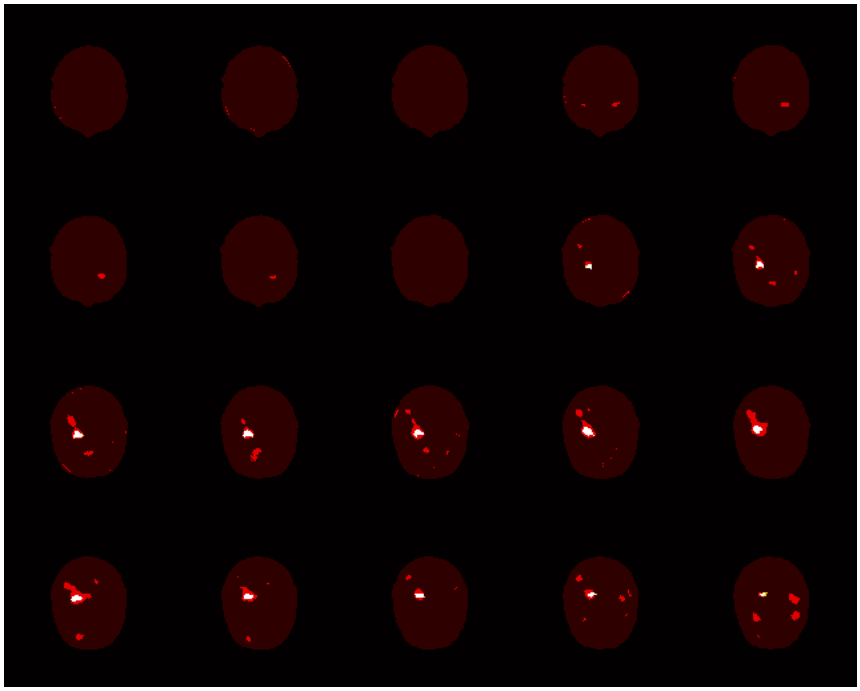

Figure 6.9: **Phantom 1 - Activation level: 70%, Method: classical substraction**. **White:** Correct detections. **Yellow:** False negatives. **Red:** False positives. No false negatives. The number of false positives is reduced.

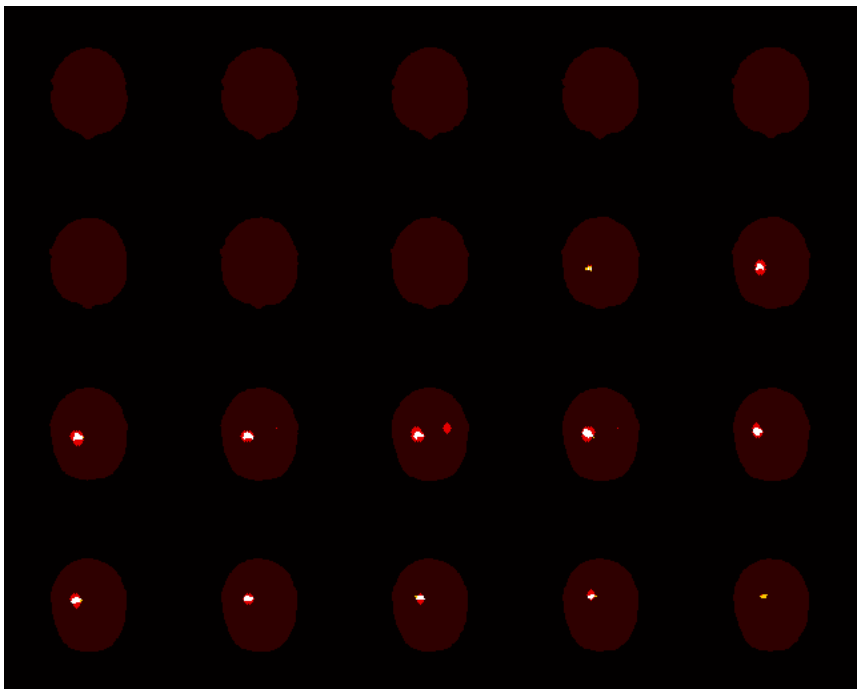

Figure 6.10: **Phantom 1 - Activation level: 100%, Method: a-contrario**. **White:** Correct detections. **Yellow:** False negatives. **Red:** False positives. The a-contrario method presents almost no false negatives nor false positives.

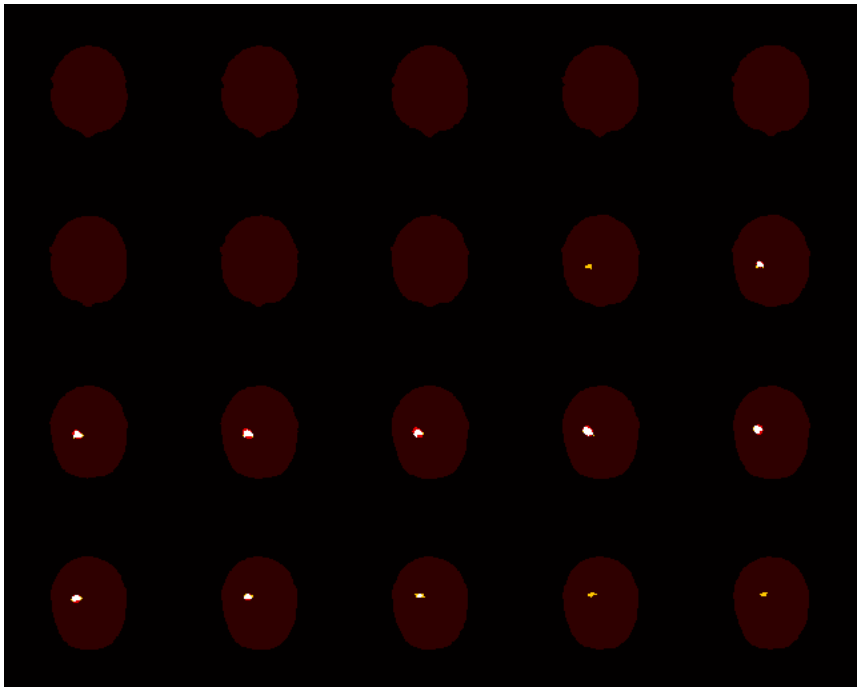

Figure 6.11: **Phantom 1 - Activation level: 100%, Method: old a-contrario**. **White:** Correct detections. **Yellow:** False negatives. **Red:** False positives. The detection results are similar to those of the new a-contrario approach but more precise (less amount of false positives).

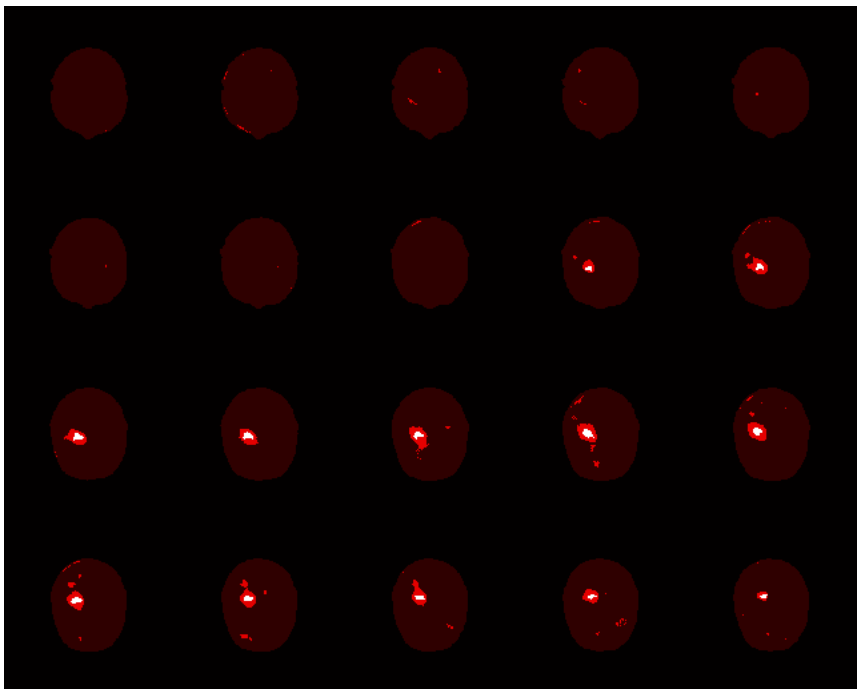

Figure 6.12: **Phantom 1 - Activation level: 100%, Method: classical substraction**. **White:** Correct detections. **Yellow:** False negatives. **Red:** False positives. No false negatives. The detection is less precise than that of the a-contrario methods.

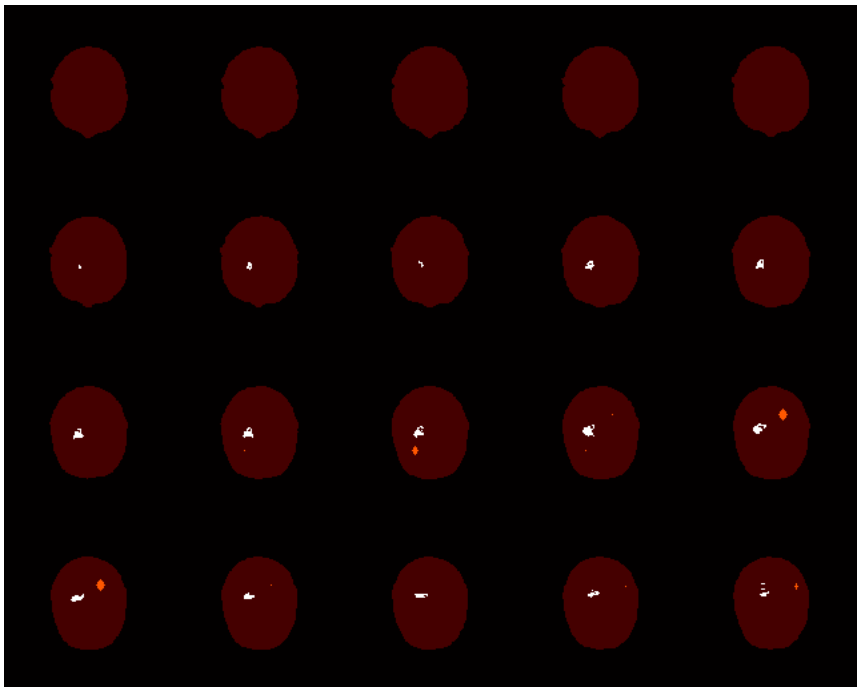

Figure 6.13: **Phantom 2 - Activation level: 20%, Method: a-contrario**. **White:** False negatives. **Orange:** False positives. The activation zone is not detected.

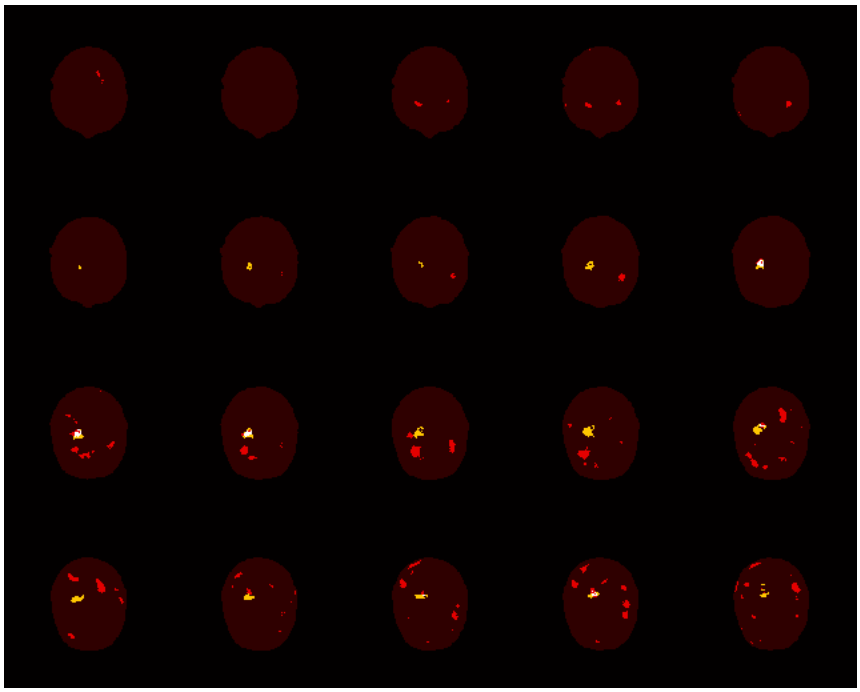

Figure 6.14: **Phantom 2 - Activation level: 20%, Method: classical substraction**. **White:** Correct detections. **Yellow:** False negatives. **Red:** False positives. The substraction method detects a small region of the EZ and presents a large number of false positives.

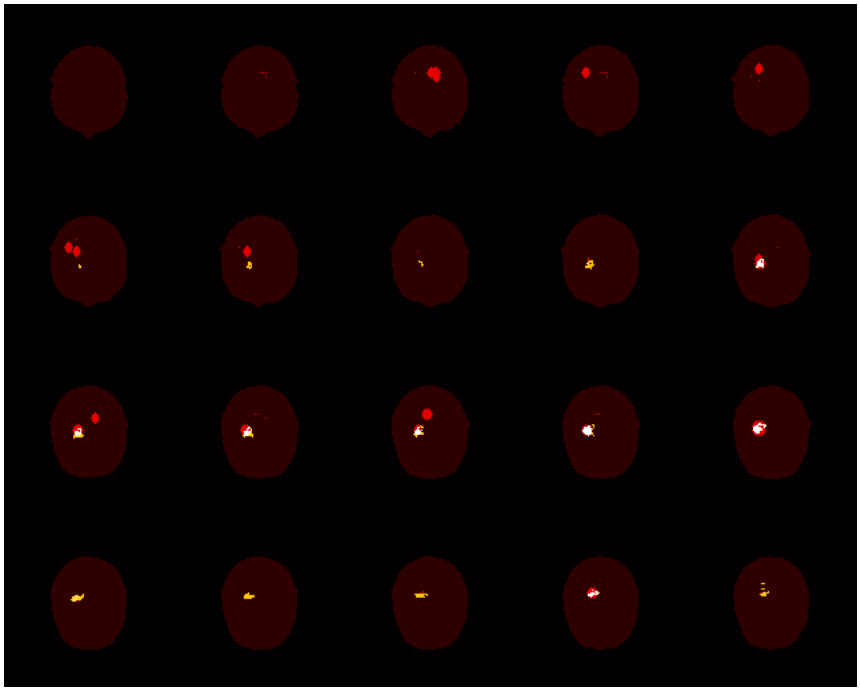

Figure 6.15: **Phantom 2 - Activation level: 40%, Method: a-contrario**. **White:** Correct detections. **Yellow:** False negatives. **Red:** False positives. The detectability of the a-contrario approach is increased for the 40% case, but it still does not find most of the EZ.

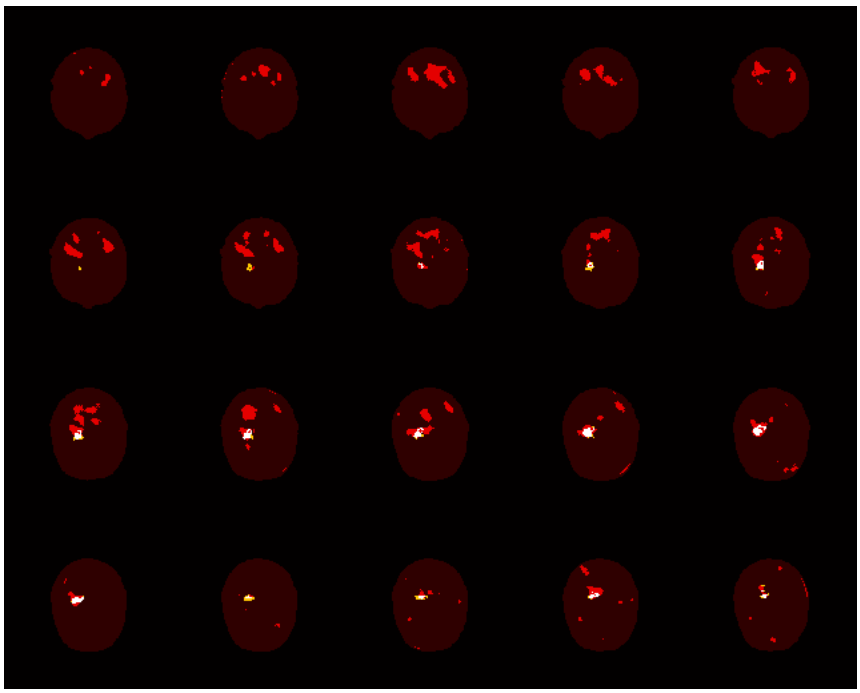

Figure 6.16: **Phantom 2 - Activation level: 40%, Method: classical substraction**. **White:** Correct detections. **Yellow:** False negatives. **Red:** False positives. The substraction method has no false negatives but increases the number of false positives.

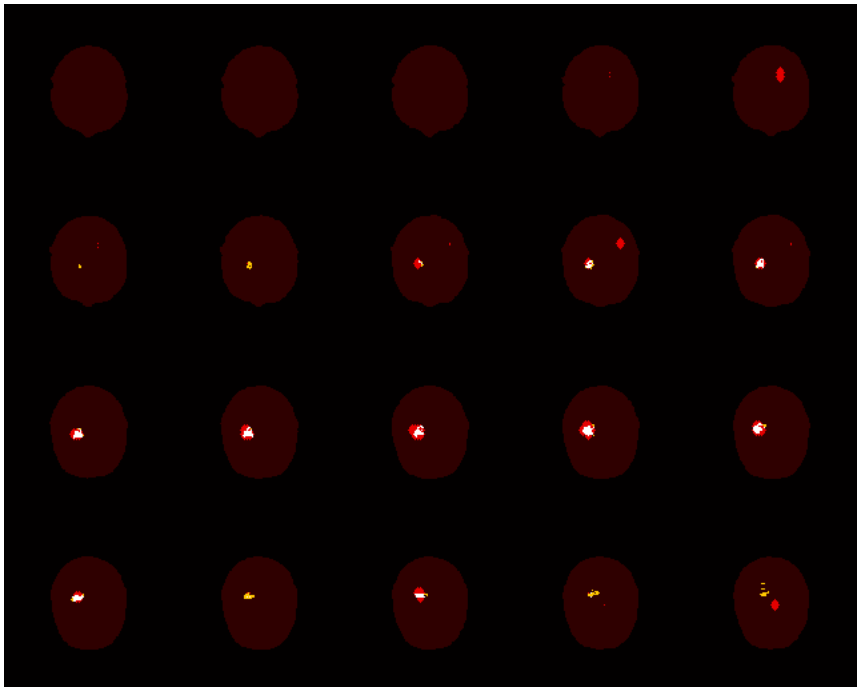

Figure 6.17: **Phantom 2 - Activation level: 60%, Method: a-contrario**. **White:** Correct detections. **Yellow:** False negatives. **Red:** False positives. The a-contrario approach detects most of the EZ with a small number of false positives.

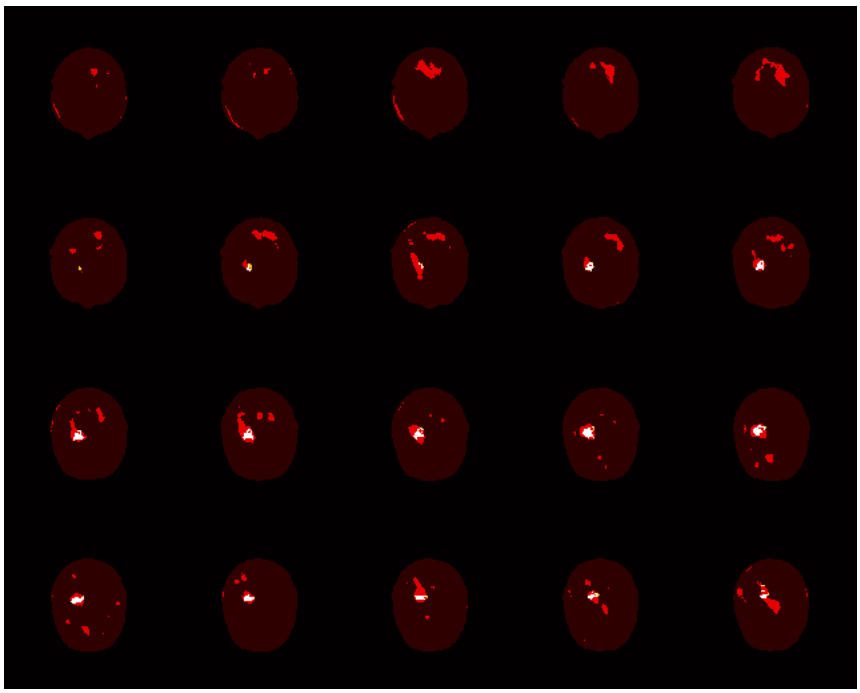

Figure 6.18: **Phantom 2 - Activation level: 60%, Method: classical substraction**. **White:** Correct detections. **Yellow:** False negatives. **Red:** False positives. The substraction approach detects all the active regions but very imprecisely.

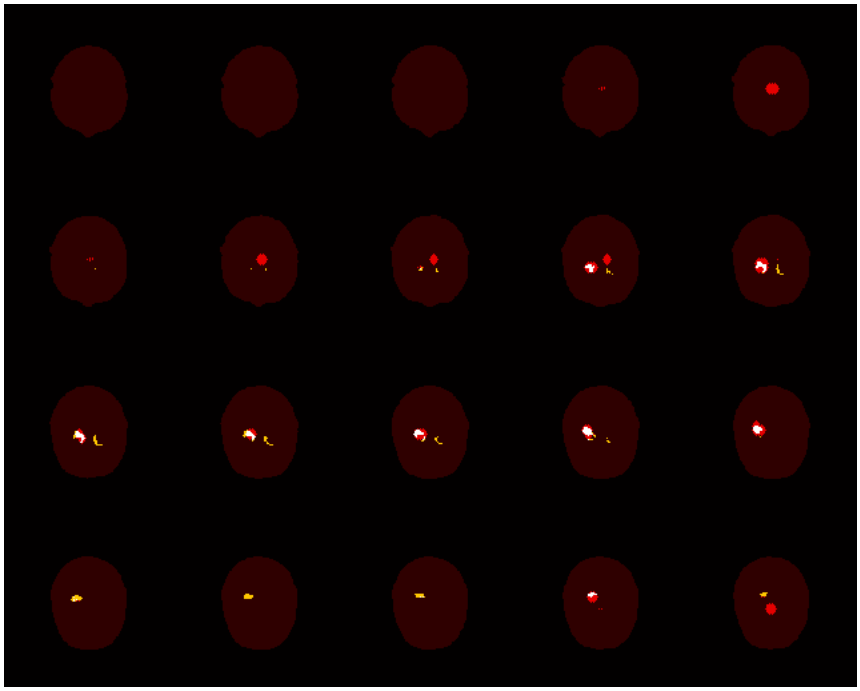

Figure 6.19: **Phantom 3 - Method: a-contrario**. **White:** Correct detections. **Yellow:** False negatives. **Red:** False positives. The a-contrario method detects the EZ, but not completely. It presents a small number of false positives.

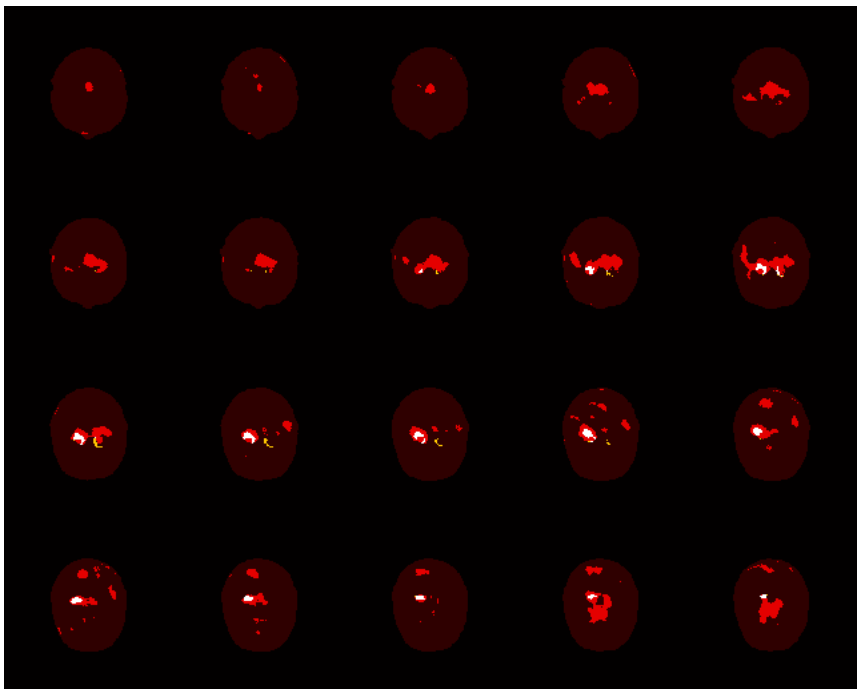

Figure 6.20: **Phantom 3 - Method: classical substraction**. **White:** Correct detections. **Yellow:** False negatives. **Red:** False positives. The substraction approach has no false negatives but a very imprecise detection.

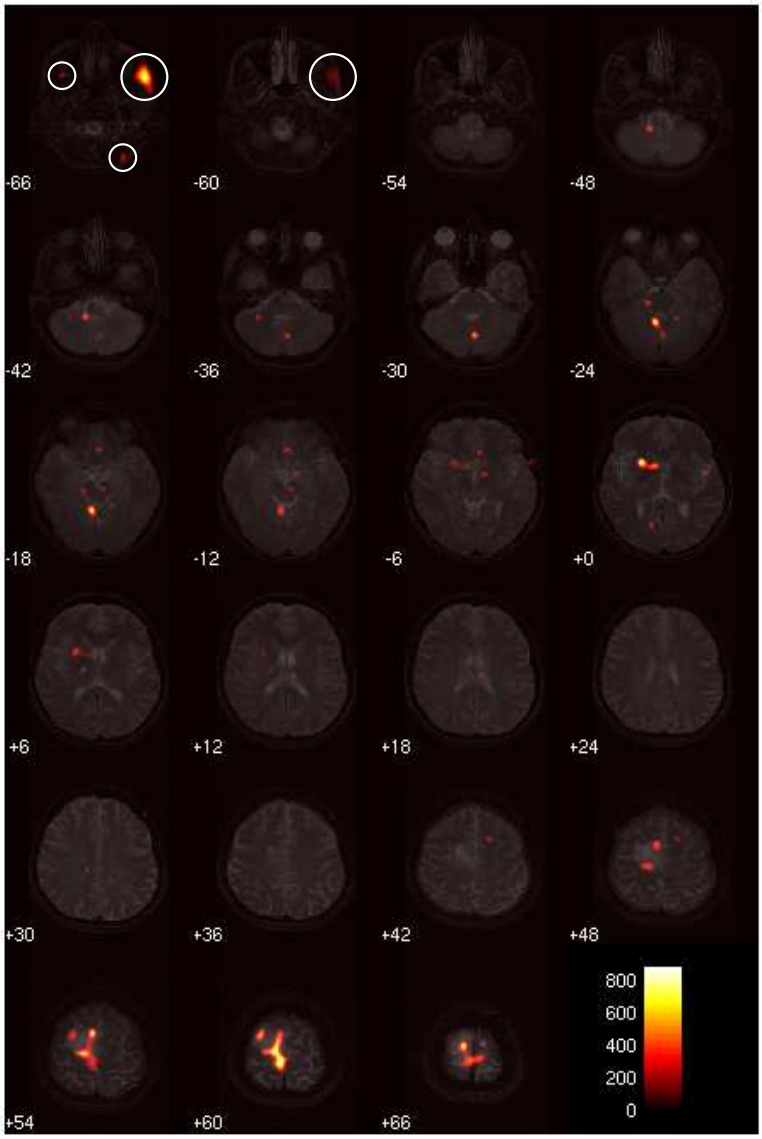

Figure 6.21: **Method: old a-contrario**. The white circles show four false positives that are no longer present on the new a-contrario detection result. See Figure 6.22.

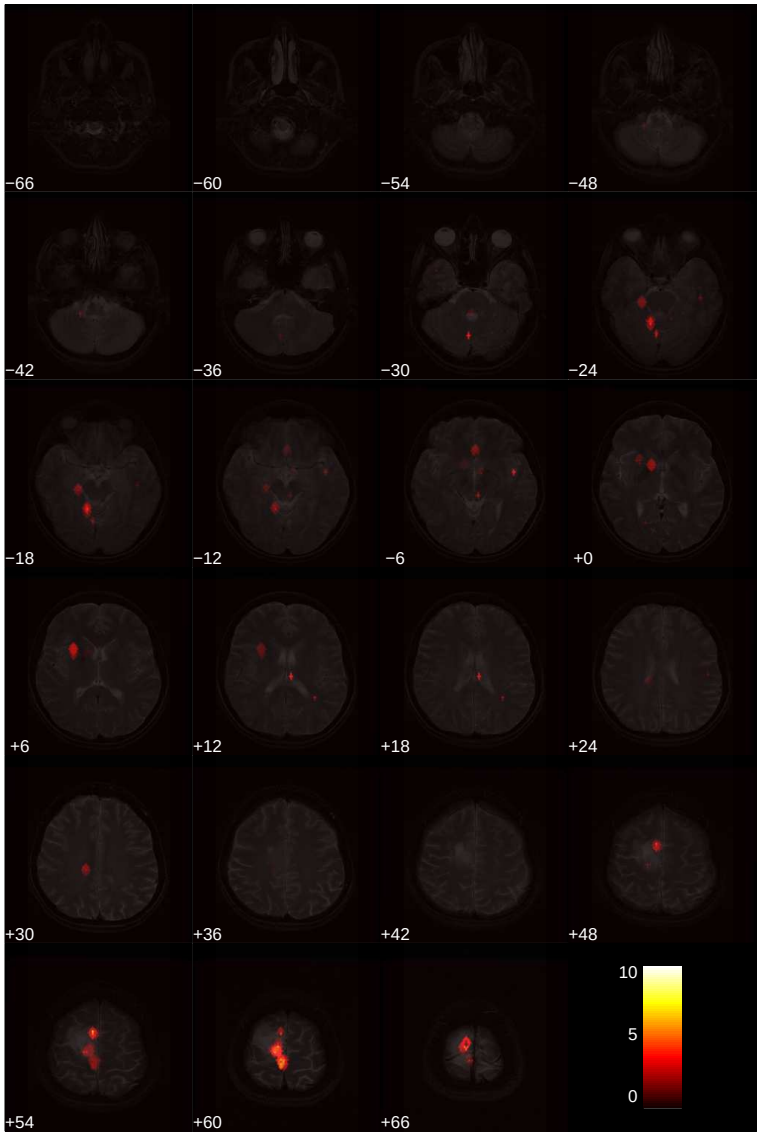

Figure 6.22: **Method: new a-contrario**. The false positives marked with white circles in Figure 6.21 are no longer present in the new a-contrario detection. Notice that the rest of the detections are quite similar and in particular the EZ is correctly localized by both methods (slices +54 and +60).

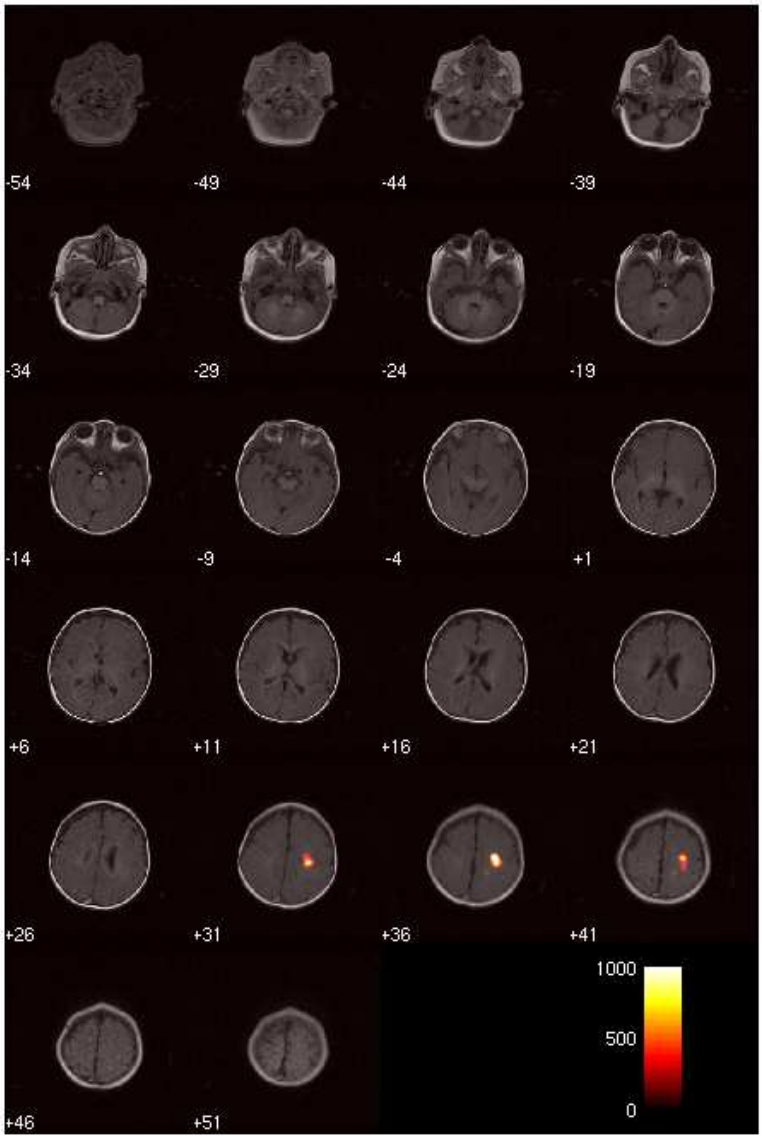

Figure 6.23: **Method: old a-contrario**. The old a-contrario detection in this case is particularly *clean*. The EZ is almost the only detection. A low number of false positives is desirable for a correct interpretation of the results. However, this image is not in accordance with reality since during a seizure the activated zone is not only the EZ.

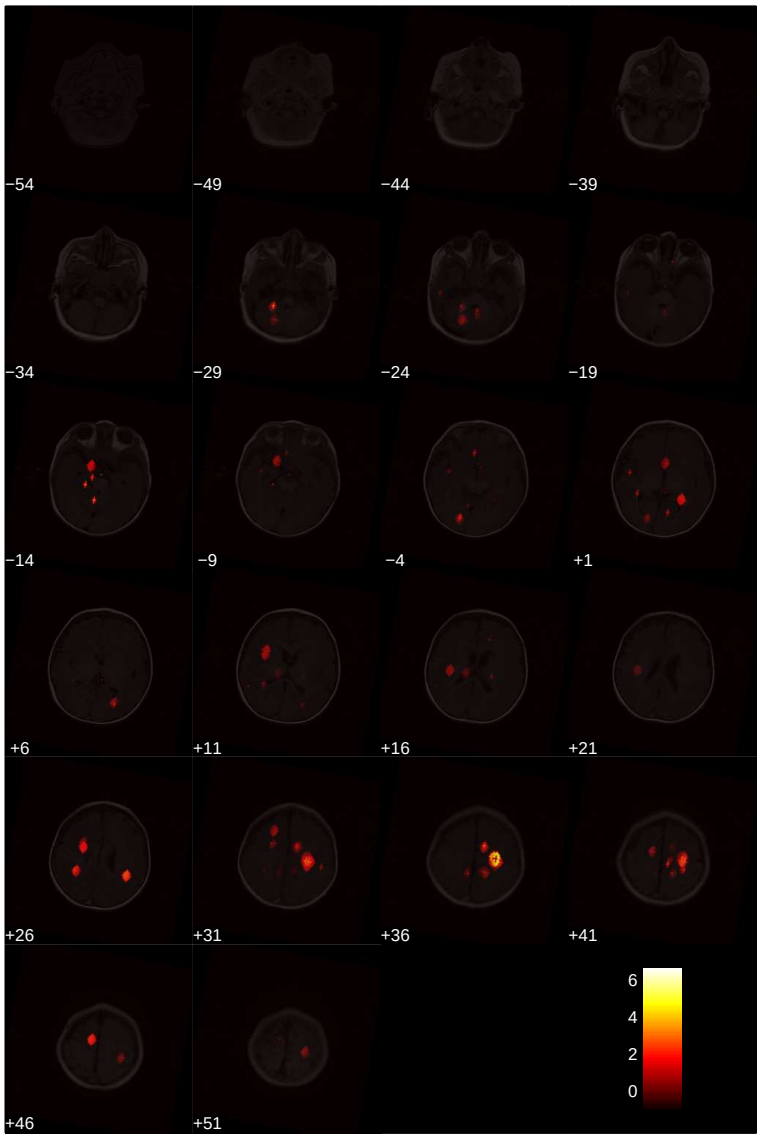

Figure 6.24: **Method: new a-contrario**. New detections appear with the new a-contrario detection method. Compare results with Figure 6.23. According to the specialist interpretation, most of the new detections are not false positives but parts of the seizure activation circuits.

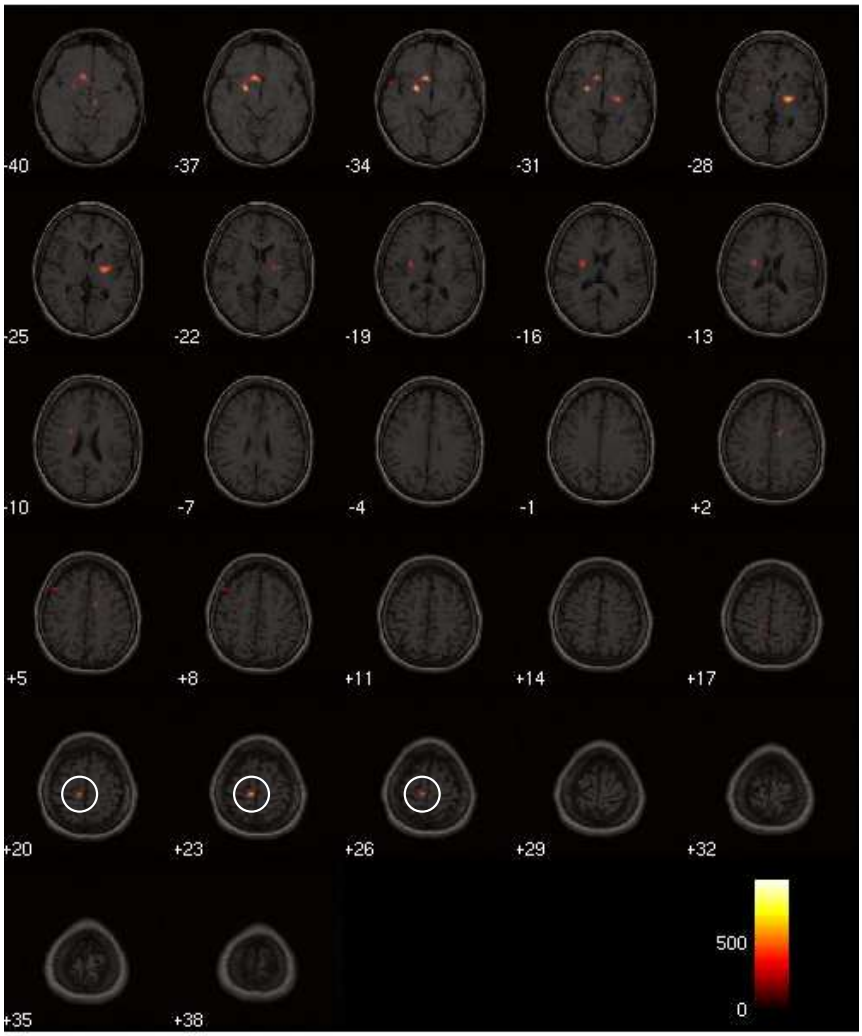

Figure 6.25: **Method: old a-contrario**. White circles show the EZ in different slices. The intensity level of the EZ is not among the highest on the image. Compare the results with those obtained by the new a-contrario method in Figure 6.25.

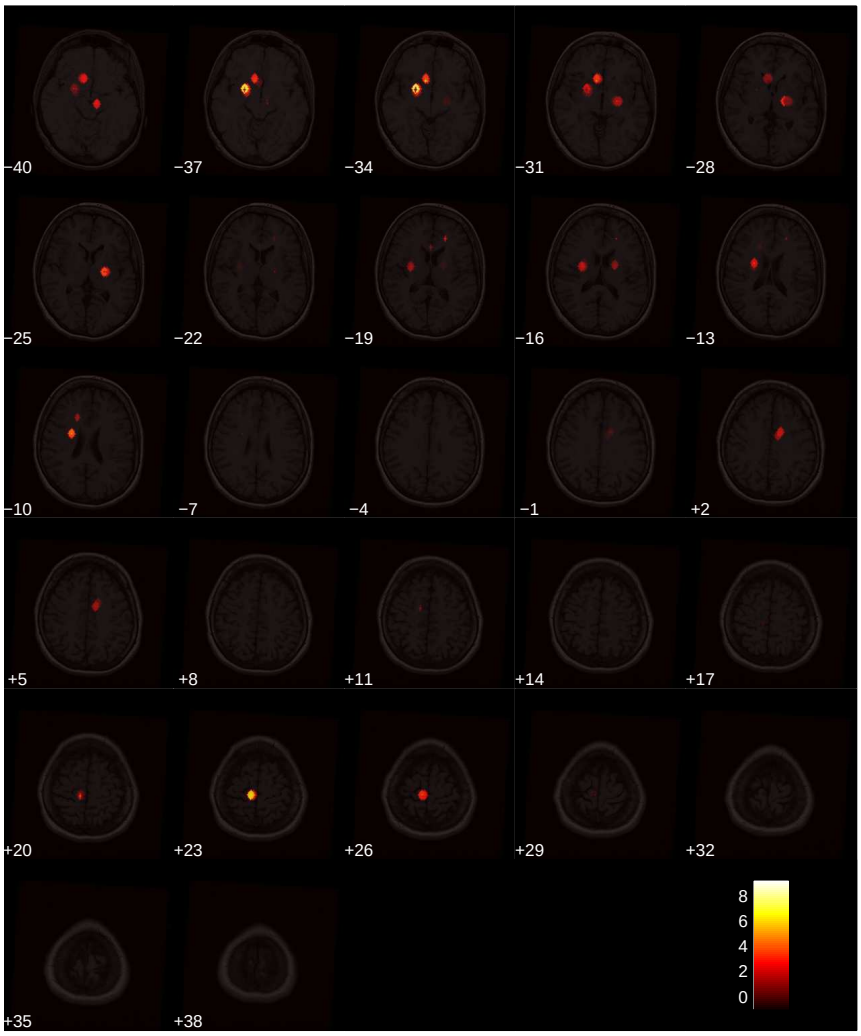

Figure 6.26: **Method: new a-contrario**. The EZ is clearly identified and its intensity is among the highest in the image (slice +23). Compare the results with those obtained by the old a-contrario method in Figure 6.25.

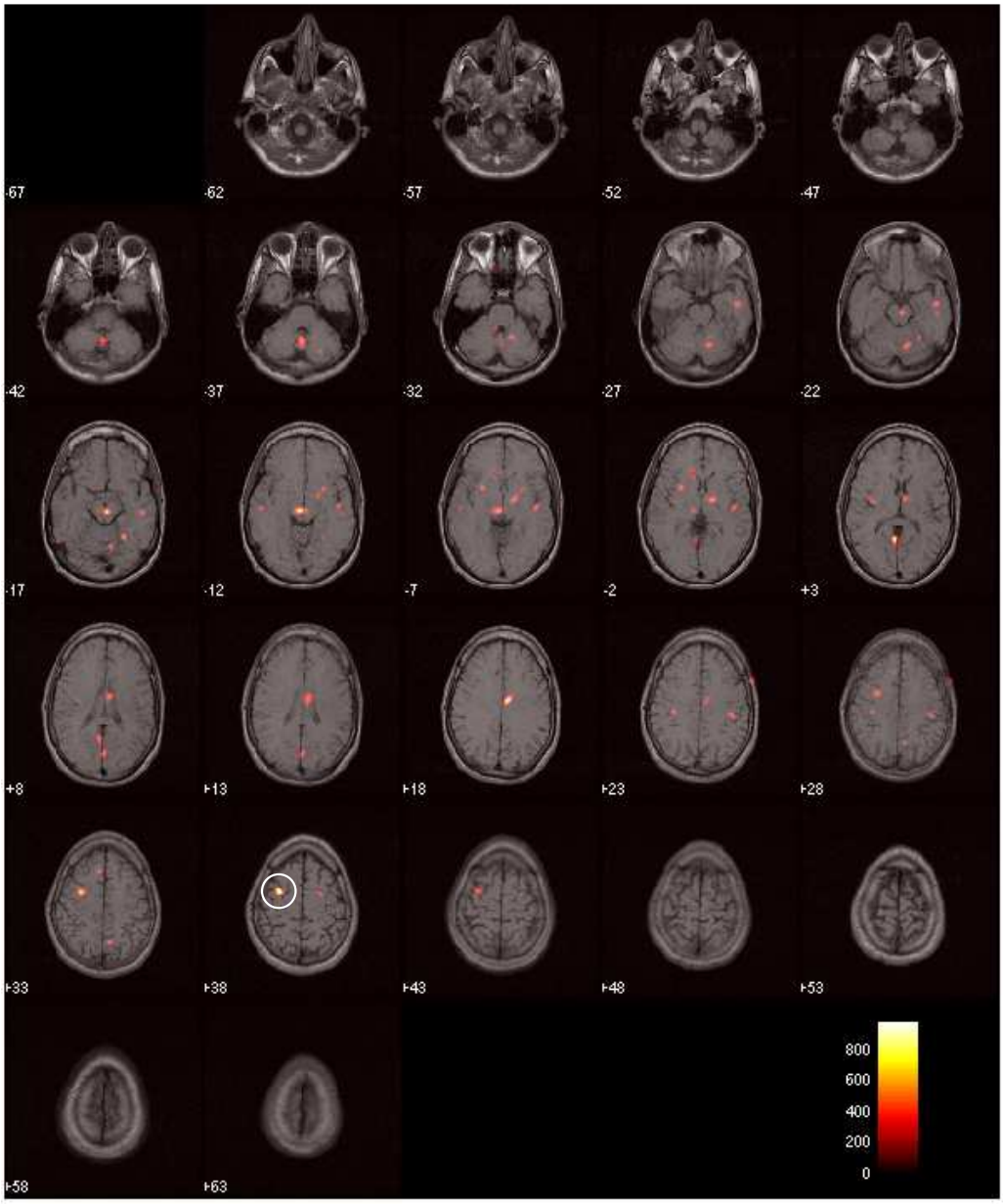

Figure 6.27: **Method: old a-contrario**. The White circle shows the EZ. It is clearly identified and its intensity level is among the highest on the image. Compare the results with those obtained by the new a-contrario method in Figure 6.28.

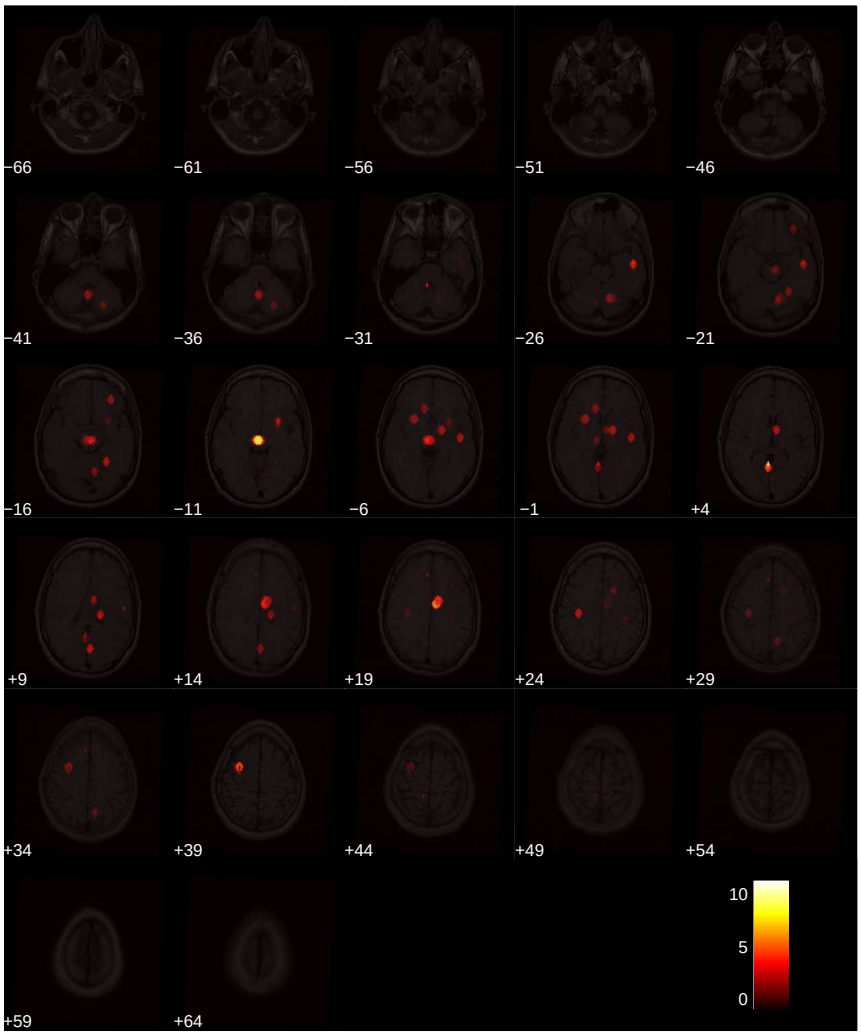

Figure 6.28: **Method: new a-contrario**. The EZ is identified but with lower intensity than in the old a-contrario result (slice +39). Compare the results with those obtained by the old a-contrario method in Figure 6.27.

Chapter 7

SPECT denoising

One of the aims of this work is to propose a denoising technique to improve SPECT images quality. For that purpose, we have studied the SPECT image formation process and we have characterized SPECT images, both sinograms and tomographic images, so that to propose a denoising technique well-suited to this kind of images. The denoising process can be performed either before reconstruction, i.e. on the sinograms, or after reconstruction, i.e. on the tomographic images. A post-reconstruction denoising method does not seem so direct, since as we showed in Section 5.2.1, the reconstructed image pixels are correlated (denoising techniques are usually based on the hypothesis of independent or uncorrelated noise) and follow a multivariate log-normal law. On the contrary, given that sinogram pixels can be modeled as independent, Poisson distributed random variables, we propose to apply a pre-reconstruction denoising technique specially designed to remove uncorrelated Poisson noise. This Poisson denoising technique was recently proposed by Deledalle et al. [48] and is an extension of the NL means image denoising approach [49].

We start this section presenting in 7.1 a brief summary of the denoising techniques applied to photon low-count images. Section 7.2 is devoted to describe the denoising approach of Deledalle et al. In Section 7.3 we present an experimental evaluation of the denoising technique, with simulated and real examples.

7.1. Denoising photon low-counts images

As we previously mentioned, the ET denoising process can be performed either before reconstruction, i.e. on the sinograms, or after reconstruction, i.e. on the tomographic images. However, most of the recent work in ET image denoising is performed before reconstruction. This may be caused by the same reason that motivated us to perform denoising before reconstruction, i.e. the known independent, Poisson distributed model for sinogram images. In the following we present a brief summary of pre-reconstruction denoising methods. We will classify them into two groups: whether taking into account the Poisson nature of the sinogram images or not.

Well-known filters like Hanning, Butterworth, Metz and Wiener have been widely used in ET applications to reduce noise components before reconstruction [12]. They are examples of those not considering the Poisson nature of the images. These filters have the drawback of degrading image contrast and introducing blur. In order to overcome this issues, adaptive non-stationary noise reduction filters have been proposed [50, 51, 52].

Multi-scale wavelet based techniques have been widely developed for ET denoising applications. Most of these algorithms are based on the idea of thresholding the wavelet image coefficients and then synthesizing the denoised image from the resulting coefficients. The two approaches can be encountered, both accounting for the Poisson nature or not. Among the latter we may mention

the work of Jin et al. [53] who propose a wavelet based multi-scale denoising technique using a cross-scale correlation scheme to define thresholds. Examples of those taking into account the Poisson nature of the images are the work of Timmermann and Nowak [54], who derived a Bayesian intensity estimate procedure, the Multiscale Multiplicative Innovations (MMI) model for Poisson denoising; the work of Willet and Nowak [55], who introduced a multiscale method for nonparametric piecewise polynomial intensity and density estimation of Poisson point processes; and the work of Nowak et al [56] who propose a wavelet-domain filtering procedure designed using cross-validation. In [57] we can find a comparative study of denoising wavelet based methods.

Variations of the total variation (TV) regularization scheme proposed by Rudin et al. [58] have also been applied to medical imaging denoising. Among them, the work of Dey et al. [59], proposes to combine the Richardson-Lucy algorithm with a regularizing constraint based on total variation, whose smoothing avoids oscillations while preserving edges; and the work of Bardsley et al. [60] proposes a total variation-penalized Poisson likelihood estimation approach. These two methods take into account the Poisson nature of images. On the contrary, Zhang et al. [61] propose a method based on a total variation minimization approach independent of the Poisson nature of the noise.
In [62, 63] we can find examples of platelet based methods, suited to Poisson distributed data, applied to nuclear imaging denoising. The performance of these denoising methods is not always fully investigated. One of the main reasons is the lack of ground-truth information for real ET studies. For this reason, in many cases the performance evaluation is only qualitative. Performance comparisons between different denoising algorithms are not easily done since an established protocol does not exist. Despite this, some examples of comparative analysis can be found in the literature[12, 57].

7.2. Poisson Non-local Means

In [48] Deledalle et al. propose an extension of NL means image denoising [49] for the case of images corrupted by Poisson noise. NL means performs image denoising by averaging pixels of similar value. Let us consider the true image u, the noisy data v and $\hat{u}$ the estimation of u from v. Images are considered to be defined over a discrete regular grid Ω and v_s denotes a pixel value at site $s \in \Omega$. NL means defines the estimate $\hat{u}$ of u as

$$\hat{u}_s = \frac{\sum_t w_{s,t} v_t}{\sum_t w_{s,t}}, \tag{7.1}$$

where t denotes image pixels and $w_{s,t}$ is a weight depending on the similarity between s and t pixel values. For robustness reasons, t is limited to a search window centered at s and the similarity between pixels s and t is based on patches Δ_s and Δ_t centered at them. Patches similarity is usually defined by the Euclidean distance, giving rise to the following expression for weight values

$$w_{s,t} = \exp\left(-\frac{\sum_b (v_{s+b} - v_{t+b})^2}{\gamma}\right),$$

where $_{s+b}$ and $_{t+b}$ denotes pixel b on Δ_s and Δ_t respectively and γ is a filtering parameter.
Deledalle et al. propose a probabilistic approach for weights calculation. They propose to find $w_{s,t}$ as

$$w_{s,t} = P(u_{\Delta_s} = u_{\Delta_t} | v)^{1/\alpha}. \tag{7.2}$$

The probability $P(u_{\Delta_s} = u_{\Delta_t} | v)$ evaluates the hypothesis

$$\mathcal{H}_0 : \quad u_{\Delta_s} = u_{\Delta_t},$$

i.e. patches Δ_s and Δ_t being equal in the noise-free image. Under the assumption of non-spatially correlated noise, the probability can be calculated as

$$P(u_{\Delta_s} = u_{\Delta_t}|v) = \prod_b P(u_{s+b} = u_{s+b}|v_{s+b}, v_{t+b}). \tag{7.3}$$

The value $P(\lambda_{\Delta_s} = \lambda_{\Delta_t}|k)$ is called *statistical similarity*. In a Bayesian framework we have

$$P(u_1 = u_2|v_1, v_2) = \underbrace{\frac{p(v_1, v_2|u_1 = u_2)}{p(v_1, v_2)}}_{\text{Similarity } L(v_1, v_2)} \underbrace{P(u_1 = u_2)}_{\text{Empirical Similarity}}, \tag{7.4}$$

where to simplify the notation we have substituted $_{s+b}$ and $_{t+b}$ for $_1$ and $_2$ respectively.

The first term in 7.4, $L(v_1, v_2)$, evaluates the hypothesis that the noisy pixels v_s and v_t come from a distribution with the same parameter u versus the hypothesis that their parameters u_1 and u_2 are independent. In the case of u, u_1 and u_2 being known, the likelihood ratio test $L(v_1, v_2)$ is the most powerful test (cf. Neyman-Pearson). Since in our case these parameters are unknown, a new formulation of $L(v_1, v_2)$ is needed including all their possible values. In [48] the authors propose to use an alternative test based on considering the parameter values that maximize the likelihood ratio. The *generalized* similarity function is then

$$\begin{aligned} L_G(v_1, v_2) &= \frac{\sup_{\mathsf{u}} p(v_1; u_1 = \mathsf{u}) p(v_2; u_2 = \mathsf{u})}{\left(\sup_{\mathsf{u}_1} p(v_1; u_1 = \mathsf{u}_1)\right) \left(\sup_{\mathsf{u}_2} p(v_2; u_2 = \mathsf{u}_2)\right)} \\ &= \frac{p(v_1, v_2; u_1 = \hat{\mathsf{u}}, u_2 = \hat{\mathsf{u}})}{p(v_1, v_2; u_1 = \hat{\mathsf{u}}_1, u_2 = \hat{\mathsf{u}}_2)}. \end{aligned} \tag{7.5}$$

Instead of evaluating the likelihood of v_1 and v_2 for all possible values u of the unknown u, the most favorable case is considered, i.e. the parameter values that maximize $L_G(v_1, v_2)$.

For low signal-to-noise ratio images it has been shown[48] that denoising performance can be improved by an iterative procedure incorporating a pre-estimate $\hat{\theta}$ of the noise-free image in the similarity calculation. The term named *Empirical Similarity* in Equation (7.4) meets this goal. It can be considered as a statistical test of the hypothesis $u_1 = u_2$ and the Kullback-Leibler divergence between the pre-estimations $\hat{\theta}_1$ and $\hat{\theta}_2$ is used for that purpose,

$$P(u_1 = u_2) = \exp\left(-\frac{1}{\nu} SD_{KL}(\hat{\theta}_1, \hat{\theta}_2)\right), \tag{7.6}$$

with

$$SD_{KL}(\hat{\theta}_1, \hat{\theta}_2) = \int [p(v|\hat{\theta}_1) - p(v|\hat{\theta}_2)] \log \frac{p(v|\hat{\theta}_1)}{p(v|\hat{\theta}_2)} dv,$$

The parameter ν represents the quality associated to the estimates $\hat{\theta}_1$ and $\hat{\theta}_2$.
Hence from (7.2), (7.3), (7.5) and (7.6) we have,

$$w_{s,t} = P(u_{\Delta_s} = u_{\Delta_t}|v)^{1/\alpha} \tag{7.7}$$

$$= \exp\left(-\frac{1}{\alpha} \underbrace{\sum_b -\ln L_G(v_{s+b}, v_{t+b})}_{F_{s,t}} - \frac{1}{\beta} \underbrace{\sum_b D_{KL}(\hat{u}_{s+b}, \hat{u}_{t+b})}_{G_{s,t}}\right) \tag{7.8}$$

$$= \exp\left(-\frac{1}{\alpha} F_{s,t} - \frac{1}{\beta} G_{s,t}\right), \tag{7.9}$$

with α a regularization parameter and $\beta = \alpha\nu$. The parameters α and β control the trade-off between the information obtained from the noisy data and that from the pre-estimate of the noise-free image. In the case of a good quality image it is better to choose a smaller α value and a larger β in order to prioritize the information from the noisy data. On the contrary, for low signal to noise ratio images it is better to increase α and decrease β so that to favor the pre-filtered data. In the case of Poisson degraded images, the noisy-data similarity criteria $F_{s,t}$ becomes [48]

$$F_{s,t} = \sum_b -\ln L_G(v_{s+b}, v_{t+b}) \tag{7.10}$$

$$= \sum_b v_{s+b}\ln v_{s+b} + v_{t+b}\ln v_{t+b} - (v_{s+b}+v_{t+b})\ln\frac{v_{s+b}+v_{t+b}}{2}, \tag{7.11}$$

and $G_{s,t}$

$$G_{s,t} = \sum_b -\ln D_{KL}(\hat{u}_{s+b}, \hat{u}_{t+b}) \tag{7.12}$$

$$= \sum_b (\hat{u}_{s+b} - \hat{u}_{t+b})\log\frac{\hat{u}_{s+b}}{\hat{u}_{t+b}}. \tag{7.13}$$

In order to define α and β values, Deledalle et al. propose to use an automatic method based on the mean square error (MSE) minimization. This method uses an estimator of the MSE for NL means with Poisson noise and the Newton's method to find the optimal parameters in few iterations.

The MSE is given by

$$\mathrm{E}\left[\frac{1}{N}|u-\hat{u}|^2\right] = \frac{1}{N}\sum_s (u_s^2 + \mathrm{E}[\hat{u}_s^2] - 2\mathrm{E}[u_s\hat{u}_s]),$$

with N the image size.
The MSE depends on the noise-free image u. However, it can be substituted by an estimation based on the Stein's unbiased risk estimator (SURE) that depends only on the noisy image $\hat{u}$. The SURE estimator for the case of Poisson noise is

$$R(\hat{u}) = \frac{1}{N}\sum_s (u_s^2 + \hat{u}_s^2 - 2v_s\bar{u}_s),$$

where $\bar{u}_s$ refers to the denoised value obtained by the NL means iterative approach applied to $\bar{v}$, i.e.

$$\bar{u}_s = \frac{\bar{w}_{s,t}\bar{v}_t}{\sum_t \bar{w}_{s,t}}, \tag{7.14}$$

with

$$\bar{w}_{s,t} = \exp\left(-\frac{\bar{F}_{s,t}}{\alpha} - \frac{G_{s,t}}{\beta}\right),$$

$$\bar{F}_{s,t} = \sum_b -\ln L_G(\bar{v}_{s+b}, \bar{v}_{t+b}),$$

$$\bar{v}_t = \begin{cases} v_t & \text{if } t \neq s \\ v_t - 1 & \text{otherwise} \end{cases}$$

Note that (7.14) is valid only if $G_{s,t}$ does not depend on the noise component v, i.e. $\hat{\theta}$ does not depend on v. This approximation holds if the noise variance is significantly reduced in $\hat{\theta}$

estimation. At last, Newton's method is used to minimize $R(\hat{u})$ and find the optimal α and β values. These parameters will be set according to the trade-off between the information brought by the noisy and the pre-estimate images. In the case of a high quality pre-estimate image, β will be low in order to prioritize the pre-estimate information in the weights calculation. The opposite occurs for a low quality pre-estimate image.

7.3. Experiments

In Section 5.1.1 we showed that the independent Poisson noise model is a suitable model for SPECT sinogram images. Thus we used the Poisson NL means algorithm to denoise sinogram images before reconstruction in order to improve the reconstructed images quality. Experiments were performed with both simulated and real scans.

7.3.1. Simulations

Emitting Sphere

We begin with a simple phantom, a spherical phantom of radius 5 cm with an inner off-centered sphere of radius 1 cm. Two activity level values were tested for the inner sphere, i.e. two and four times the activity of the outer sphere, namely *Phantom 1* and *Phantom 2*. This was found to be equivalent to relative increase of counts respect to the outer sphere of approximately 30% and 80% respectively. This *contrast* levels are of the order of those found in real scans. Simulation parameters were set in order to obtain a total number of counts in the order of 4 million, based on what would be expected for a volume of that size in a real scan [21]. We remark these aspects since higher counts and *contrast* levels inevitably lead to better denoising and reconstruction results but are not necessarily in accordance to realistic cases. Attenuation effects are simulated and scatter noise is considered. Non-ideal collimation is simulated by means of an acceptance angle of 5.0 degrees. Non-ideal detector effects are not included. The *ground-truth* used for denoising performance evaluation is obtained with the same phantom using important sampling techniques during the simulations. Almost noise-free projections are obtained and reconstructed using OSEM, set with the same parameters used to reconstruct the noisy and denoised images. The noise-free reconstructed phantom (one for each inner activity level) is taken to be the *ground-truth* for denoising performance evaluation.

Denoising performance will be evaluated through the quality of the reconstructed image. The performance indicator is the MSE between the reconstructed image and the ground-truth image. Table 7.1 shows the results obtained for both phantoms. Figures 7.1, 7.2 and 7.3 show slices 70 to 81 of the ground-truth, denoised and noisy case respectively for Phantom 1. Figures 7.5, 7.6 and 7.7 show slices 70 to 81 of the ground-truth, denoised and noisy case respectevely for Phantom 2. The inner sphere is supposed to appear in slices 72 to 85. The reconstruction from the noisy sinogram is clearly much more noisy than that of the denoised sinogram. Also very high voxel values are obtained in the outer sphere edges for the reconstructed noisy case, which makes visualization difficult since it enlarges the dynamic range of the image. In Figure 7.4 we can see a *saturated* version of Figure 7.3. All voxel values greater than 450 have been set to that value.
We find a considerably reduced value of the MSE for the denoised projections reconstruction case, 52.2 against 896.3 for Phantom 1 and 55.0 against 812.9 for the Phantom 2. The case of Phantom 1 (inner activity 2) is supposed to be more difficult since the contrast between the inner and the outer spheres is lower.

NCAT brain phantom

We performed the same denoising experiment using the NCAT brain phantom (see Figure 4.1). The phantom activity distribution (activity level in each phantom voxel) was set according to the real scan mean activity levels deduced in Section 5.1.6. Specific brain regions were set to activity

	Phantom 1		Phantom 2	
Metric	Denoised	Noisy	Denoised	Noisy
MSE	52.2	896.3	55.0	812.9

Table 7.1: **Sphere:** Denoising experimental tests results.

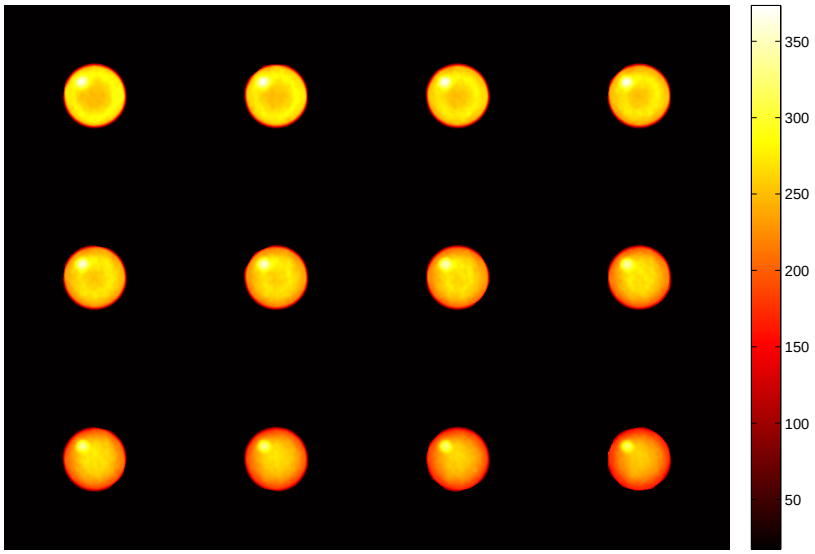

Figure 7.1: Slices of the ground-truth phantom. Phantom 1

level values below or above the mean according to the indication of a medical expert. This way a more realistic brain activity distribution is achieved. A parallel hexagonal-holes collimator was simulated. Collimator dimensions (thickness, hole radius, septal thickness) were set according to a real collimator [33]. The detector is a two-layered detector with an energy resolution (FWHM) of 10% and a reference energy of 140 keV. Attenuation effects are simulated. Scatter noise is included.

We first generated the ground-truth sinograms using importance sampling techniques. As in the previous case, we obtained an almost noise-free image that was reconstructed and used as ground-truth for the denoising performance evaluation. For this experiment, the noisy sinograms were obtained from the almost noise-free sinograms adding Poisson noise. As was explained in Section 4.2.1, the *weights* image obtained using importance sampling techniques is the image of expected values and can be used to generate various noisy versions of the simulated acquisition process by adding Poisson noise. Next, we applied the Poisson NL means denoising algorithm to the noisy sinograms to obtain the denoised version of the sinograms. The OSEM package was used to reconstruct the ground-truth, noisy and denoised sinograms.

As in the previous case we used the MSE between the reconstructed images (noisy and denoised) and the reconstructed ground-truth as denoising performance indicator. The MSE for the noisy case and the denoised cases, with different parameter values of the denoising technique, are displayed in Table 7.2. The MSE(%) indicator shows the MSE as a percentage of the sum of squared values of the ground-truth image. The parameter **patchSize** represents the denoising patch size

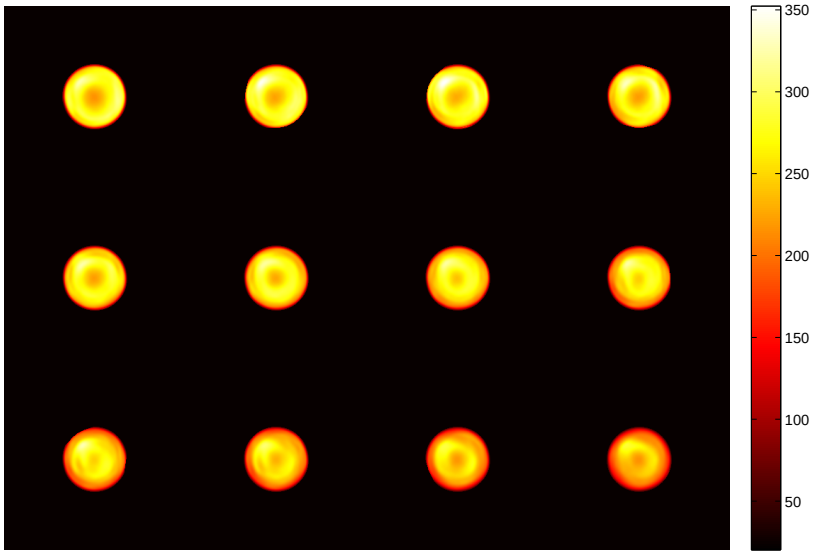

Figure 7.2: Slices of the reconstructed denoised sinogram. Phantom 1.

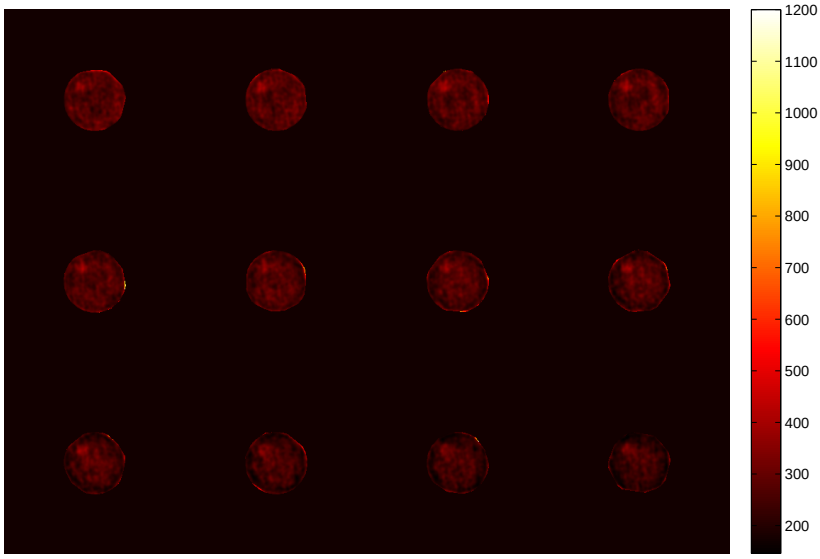

Figure 7.3: Slices of the reconstructed noisy sinogram. Phantom 1.

(**patchSize** $\times$ **patchSize**). The pre-estimate $\hat{\theta}$ of the noise-free image used in the similarity calculation is initialized as the convolution of the input image with a disk of radius **preEstSz**. Figures 7.8, 7.9 and 7.10-7.14 show slices of the reconstruction of the ground-truth, noisy and denoised

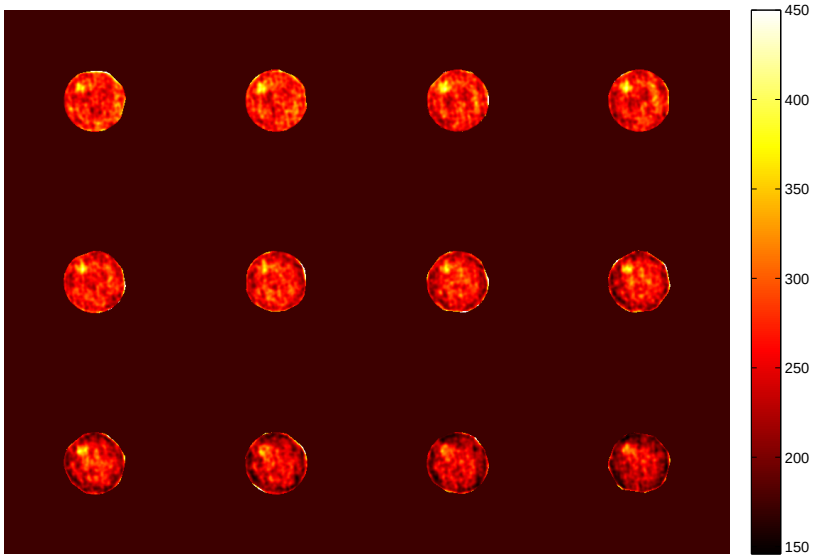

Figure 7.4: Slices of the reconstructed noisy sinogram. Saturated image. Phantom 1.

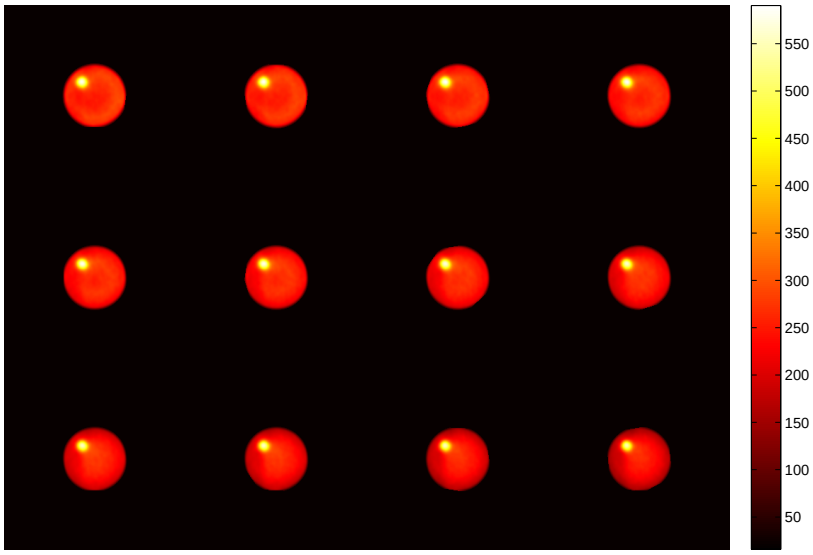

Figure 7.5: Slices of the ground-truth phantom. Phantom 2.

images respectively.

We find an improvement in reconstruction performance after sinograms denoising. The MSE

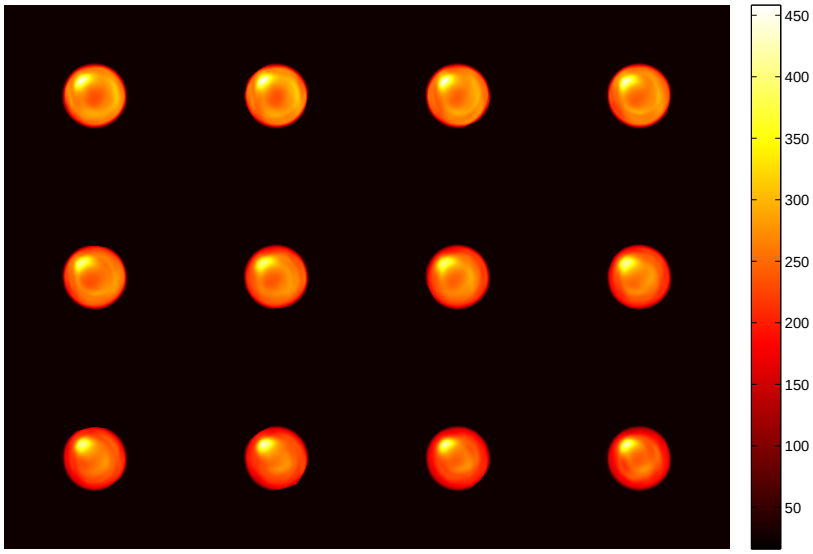

Figure 7.6: Slices of the reconstructed denoised sinogram. Phantom 2.

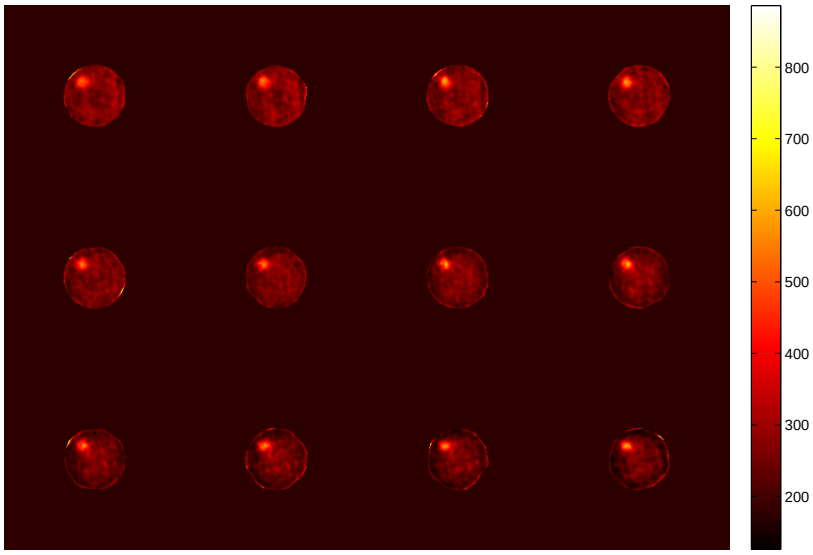

Figure 7.7: Slices of the reconstructed noisy sinogram. Phantom 2.

values for the pre-denoised images are lower than that of the noisy image. From an observer perspective, this result can also be perceived comparing the slices displayed in Figures 7.10-7.14 to those in Figure 7.9. The slices for the pre-denoised sinograms appear less noisy. On the other

	patchSize	preEstSz	MSE	MSE(%)
Noisy			7.8×10^7	2.5
Denoised	3	0	7.6×10^7	2.4
	3	1	5.0×10^7	1.6
	5	0	7.4×10^7	2.3
	5	1	4.3×10^7	1.4
	5	2	3.7×10^7	1.2

Table 7.2: **NCAT:** Denoising experimental tests results.

hand, we see different behaviors among the pre-denoised results. The larger the **patchSize**, the less noisy the results. However, this also implies much smoother images with less defined edges. The same happens for **preEstSz**, since the larger **preEstSz**, the smoother the initialization of the pre-estimate of the noise-free image. For medical applications, having correctly defined edges is crucial. Therefore, it is necessary to find a good compromise between residual noise and smoothness.

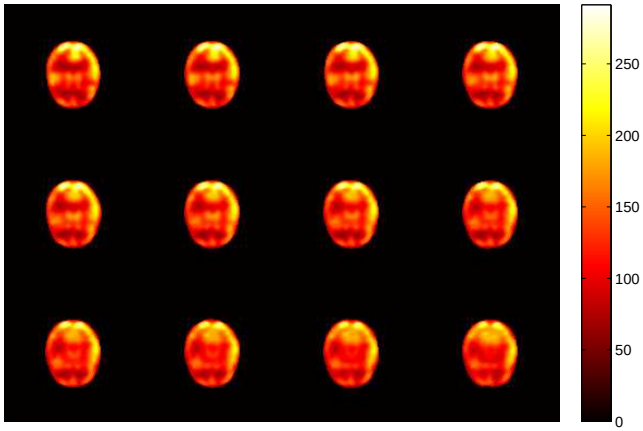

Figure 7.8: Slices of the ground-truth reconstructed NCAT phantom.

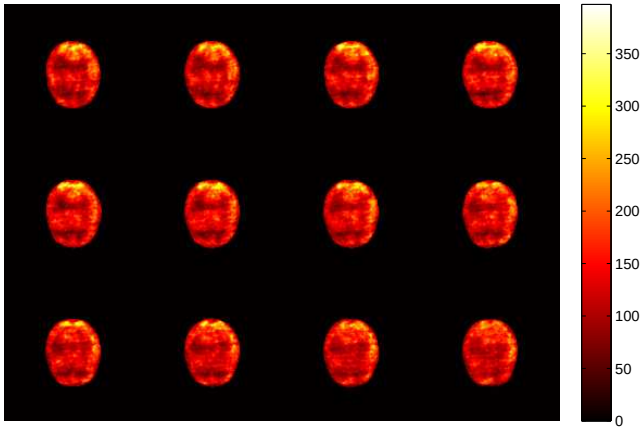

Figure 7.9: Slices of the reconstructed noisy NCAT sinogram.

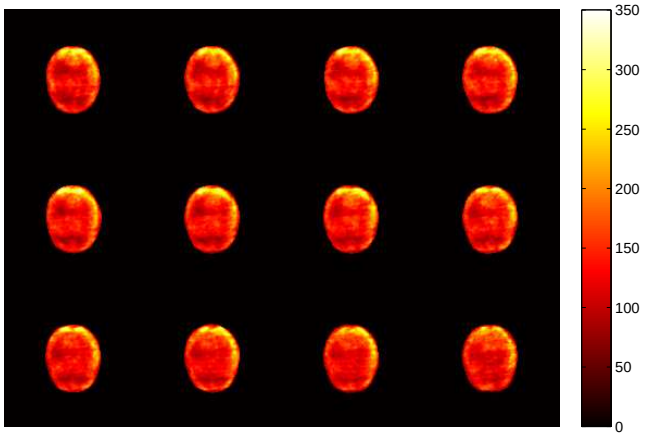

Figure 7.10: Slices of the reconstructed denoised NCAT sinogram (**patchSize** $= 3$, **preEstSz** $= 0$).

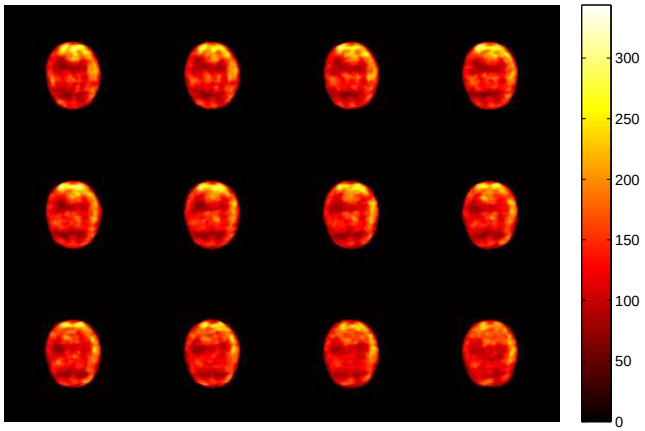

Figure 7.11: Slices of the reconstructed denoised NCAT sinogram (**patchSize** $= 3$, **preEstSz** $= 1$).

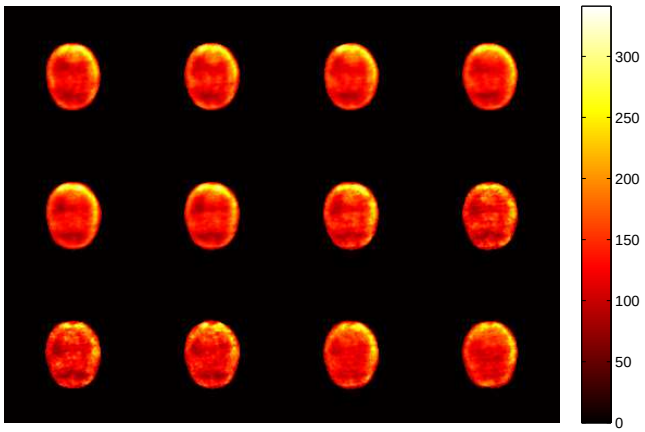

Figure 7.12: Slices of the reconstructed denoised NCAT sinogram (**patchSize** $= 5$, **preEstSz** $= 0$).

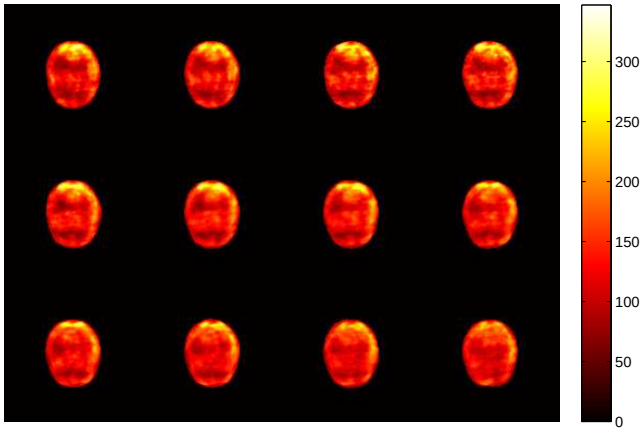

Figure 7.13: Slices of the reconstructed denoised NCAT sinogram (**patchSize** $= 5$, **preEstSz** $= 1$).

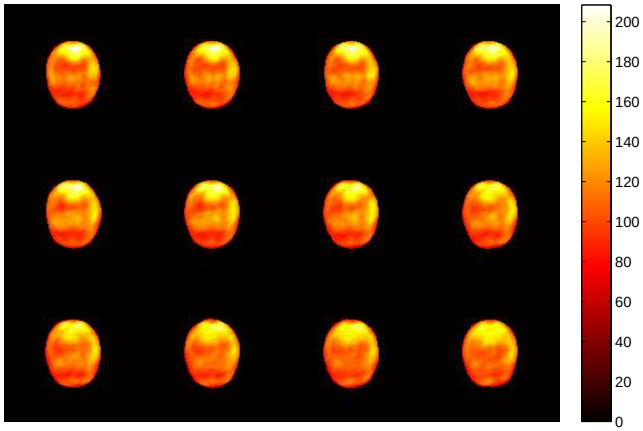

Figure 7.14: Slices of the reconstructed denoised NCAT sinogram (**patchSize** $= 5$, **preEstSz** $= 2$).

7.3.2. Real scans

The Poisson denoising technique was applied to 10 scans of 5 patients with medically refractory epilepsy (ictal and inter-ictal scans of each patient). Data was provided by the Center of Nuclear Medicine of Hospital de Clínicas, Facultad de Medicina, Universidad de la República. For each scan, three reconstructions were made:

- the OSEM reconstruction of the denoised sinograms
- the OSEM reconstruction of the denoised sinograms + post-processing (Butterworth low-pass filtering)
- the OSEM reconstruction of the original sinograms + post-processing (Butterworth low-pass filtering)

The latter is the configuration commonly used at the Center.

The low-pass filtering post-processing is necessary since the reconstruction algorithm introduces additional noise. Without post-processing, the reconstructed images are too noisy to be analyzed. The cutoff frequency of the post-processing Butterworth filters were chosen by a spe-

cialist of the Center in order to obtain the best visual result in each case.

At the Center, regular acquisitions (matrix 128×128, pixel size of 2.67mm and total photon counts of about 6 million) are processed after reconstruction using a Butterworth filter of order 10 and a frequency cutoff ranging from 0.18 to 0.20. For this study, eight of the scans were acquired with the regular parameters and post-processed with a cutoff frequency of 0.18. This frequency was increased to 0.23 to process the reconstruction of the corresponding denoised sinograms. The remaining two scans had been acquired with a pixel size of 3.45 and post-processed with a Butterworth filter of order 10 and cutoff frequency 0.25. For that case, a cutoff frequency of 0.32 was enough to obtain good results in the pre-denoised sinograms case. Thus, in all cases, the pre-denoising of the sinograms allows the utilization of a higher post-processing cutoff frequency which leads to less smoothed results.

The reconstruction of the denoised sinograms without post-processing was done for evaluation purposes. However, the results are no longer compared against the ones with post-processing since the noise introduced by the reconstruction algorithm is high and makes these images too noisy to be analyzed.

The results of the reconstructions after post-processing, with and without sinogram denoising, were analyzed and compared by an expert physician of the Center of Nuclear Medicine of Hospital de Clínicas. Figures 7.15, 7.16 and 7.17 show slices of the obtained results for two basal and one ictal scan. According to his opinion, the pre-denoised images show a significant improvement in the contrast between brain and extra-cerebral tissues with respect to the original acquisition. The cerebral cortex is shown more intense and its contours are defined with greater precision. Visual analysis of the pre-denoised images shows a better edge definition, which leads to an improvement in the anatomical detail of the brain structures and the appearance of higher resolution. In this sense, sharper edges are observed between the sulci and the brain gyrus. Certain brain areas are more prone to resolution problems, as very small or very close structures, that fail to distinguish at the common SPECT resolution. The inspection of the images was focused particularly on this kind of areas, such as the striatum, the insula or the mesial cortex and the cingulate gyrus. In most cases, a clearer separation was achieved between the head of the caudate nucleus and the putamen, the two structures that make up the striatum. A similar effect was observed in the mesial cortex and cingulate gyrus, with a better separation between the two hemispheres, as well as the separation between the insula, the inferolateral frontal cortex and the putamen. In some cases, greater contrast was seen between the hyperactive and hypoactive areas, as well as better visualization of deep brain structures with low uptake, as the mesial temporal cortex, of great importance in various neurological and psychiatric diseases, including epilepsy and dementia. This might improve the quantification of cerebral blood flow changes in these structures. In general terms, the method was considered promising, with potential improvements in several aspects and without loss of image quality.

7.3.3. Thresholding

Since the ultimate goal of denoising is improving the reconstructed images quality to ease analysis and lesion detection, we perform a simple thresholding test to evaluate lesion *detectability* in both cases: pre-denoised and non pre-denoised reconstructed images. We use the word *detectability* in italics since the concept of detectability has not been formally defined. The idea is simply to evaluate whether it exists a threshold to separate lesion from background, in our case: inner sphere from outer sphere.

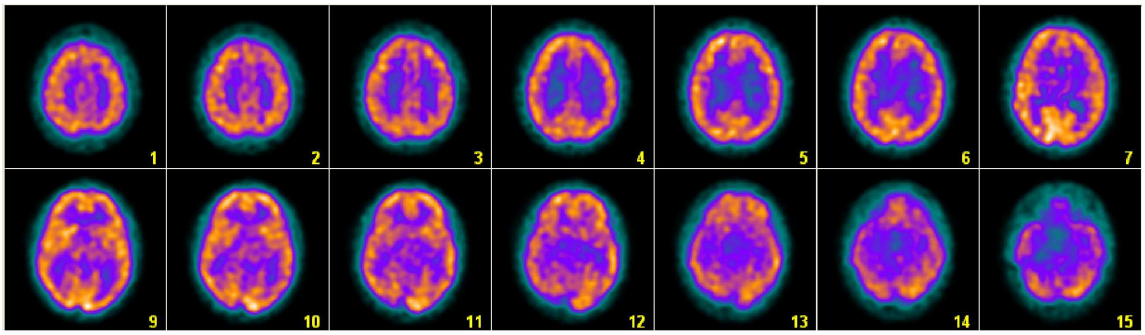

(a) Reconstruction of the denoised sinograms using OSEM with post-processing.

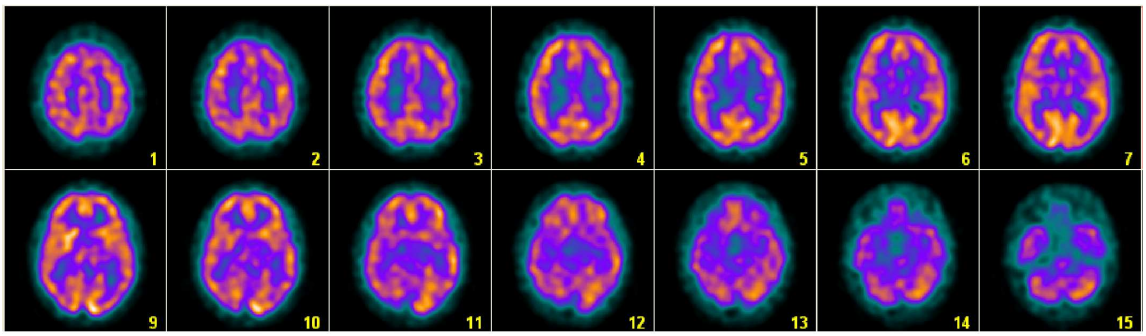

(b) Reconstruction of the original sinograms using OSEM with post-processing.

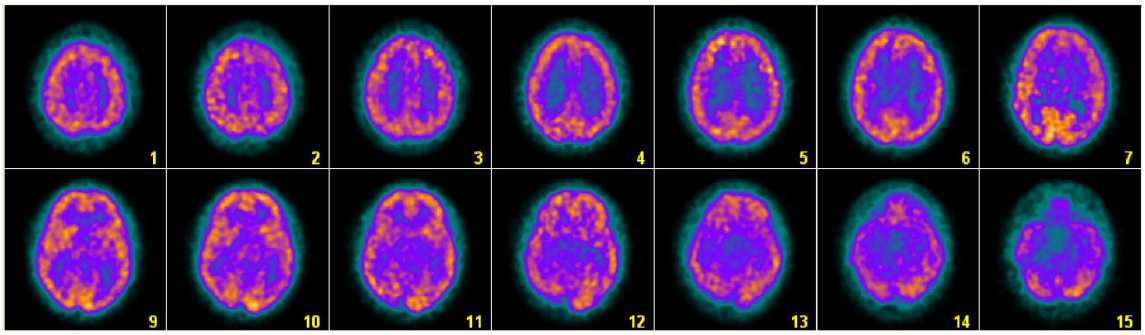

(c) Reconstruction of the denoised sinograms using OSEM without post-processing.

Figure 7.15: Comparing images (a) and (b) we can see that the denoising method seems to improve edges definition and better distinguish small adjacent structures. The post-processing filtering in (a) is less smoothing than that of (b). In image (c) we verify that the reconstruction results obtained without post-processing are too noisy.

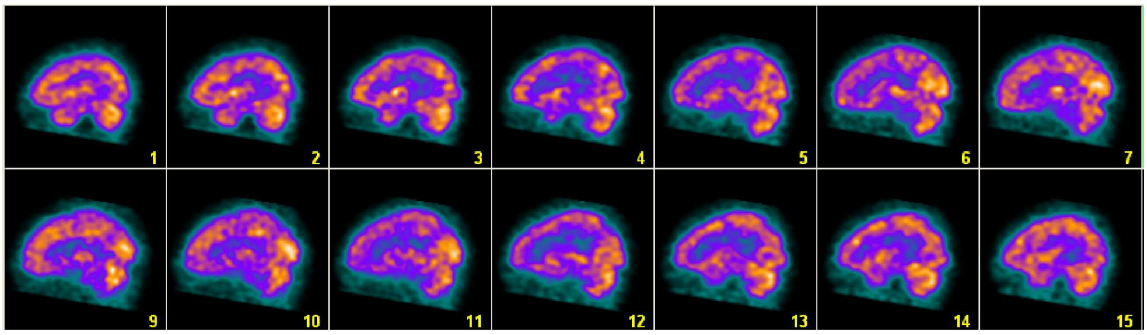

(a) Reconstruction of the denoised sinograms using OSEM with post-processing.

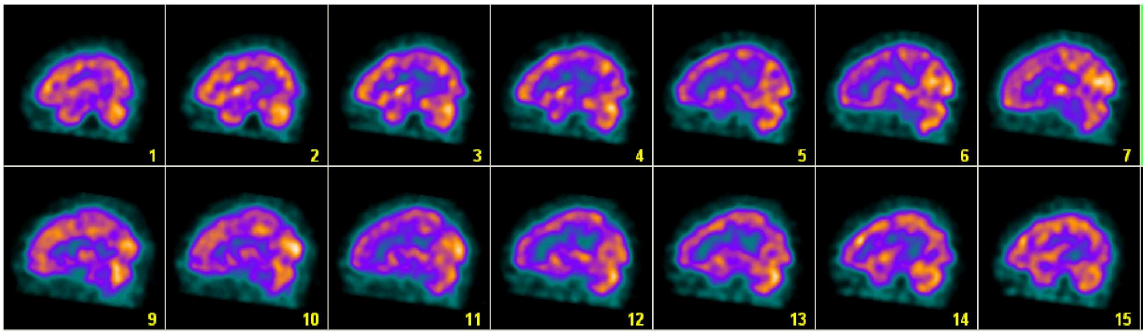

(b) Reconstruction of the original sinograms using OSEM with post-processing.

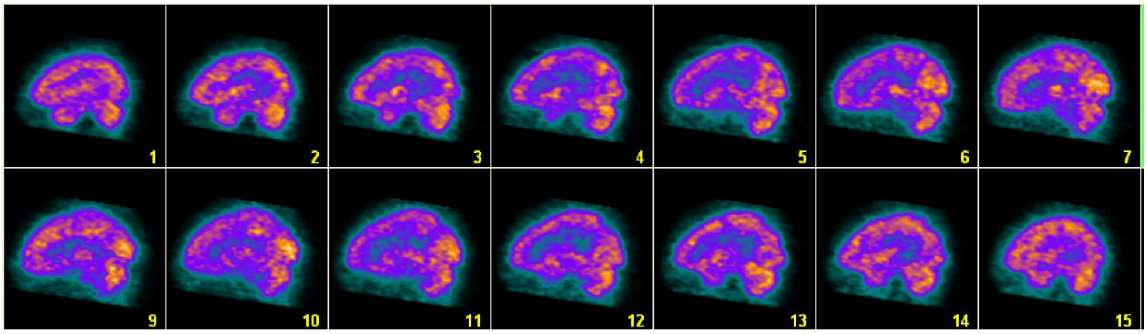

(c) Reconstruction of the denoised sinograms using OSEM without post-processing.

Figure 7.16: See caption on Figure 7.15.

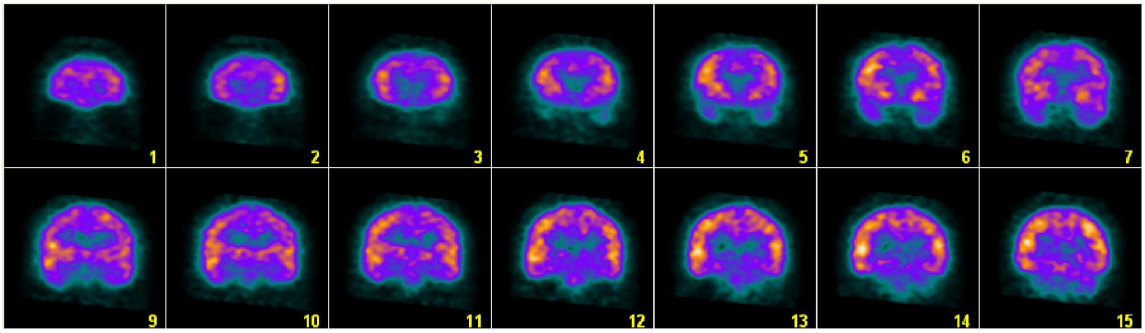

(a) Reconstruction of the denoised sinograms using OSEM with post-processing.

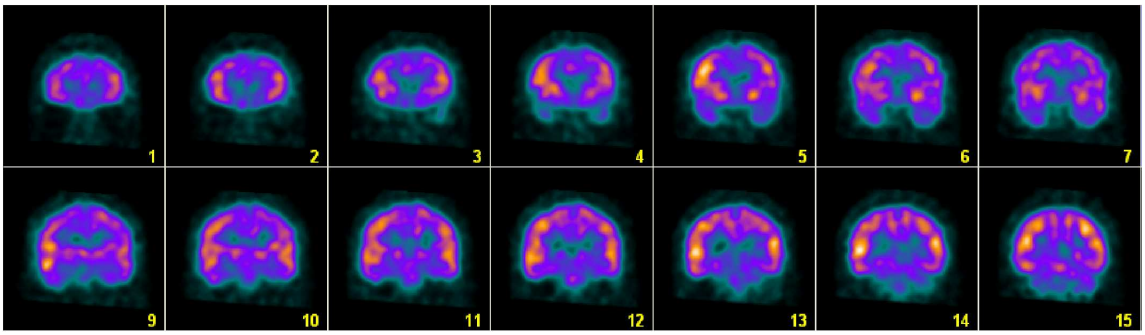

(b) Reconstruction of the original sinograms using OSEM with post-processing.

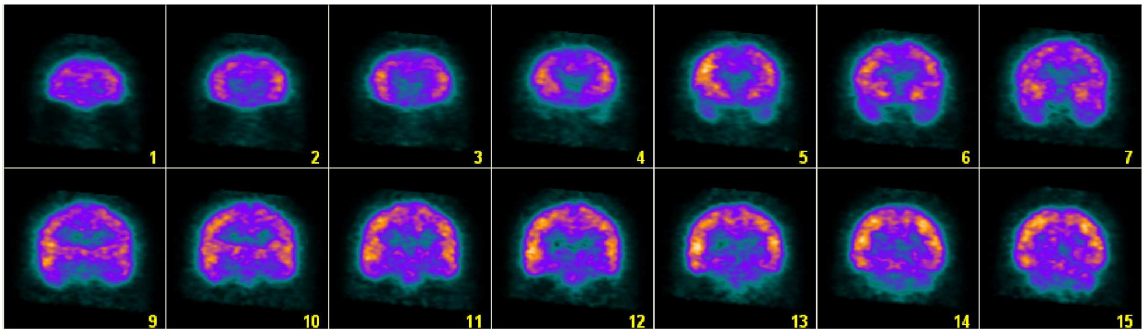

(c) Reconstruction of the denoised sinograms using OSEM without post-processing.

Figure 7.17: See caption on Figure 7.15.

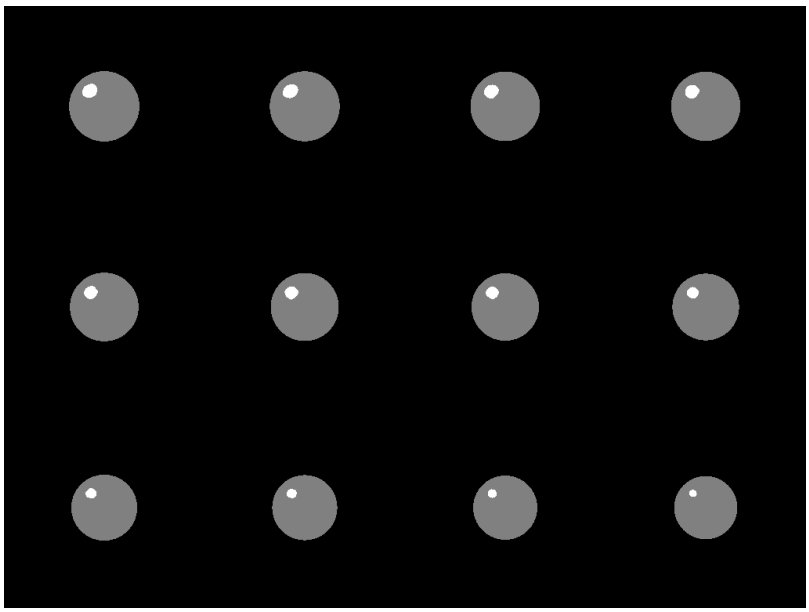

Figure 7.18: Global thresholding results for the ground-truth image. Phantom 1.

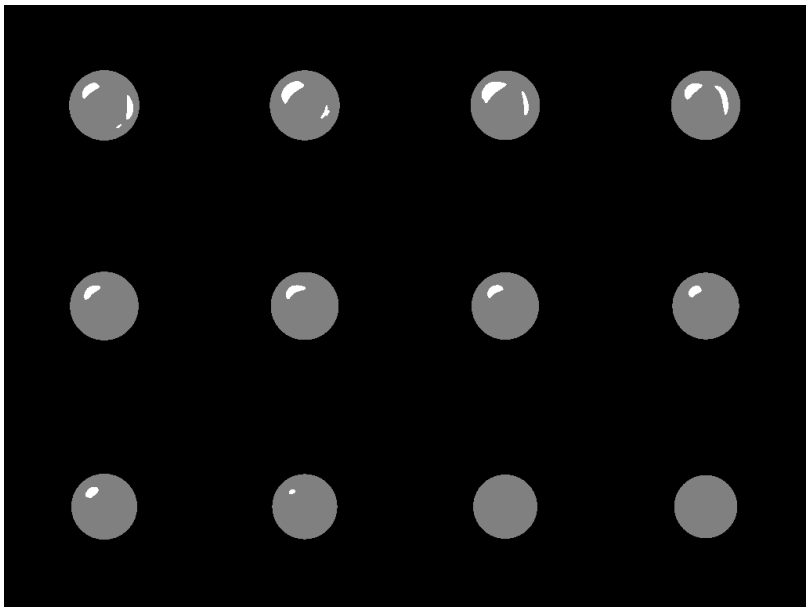

Figure 7.19: Global thresholding results for the pre-denoised case. Phantom 1.

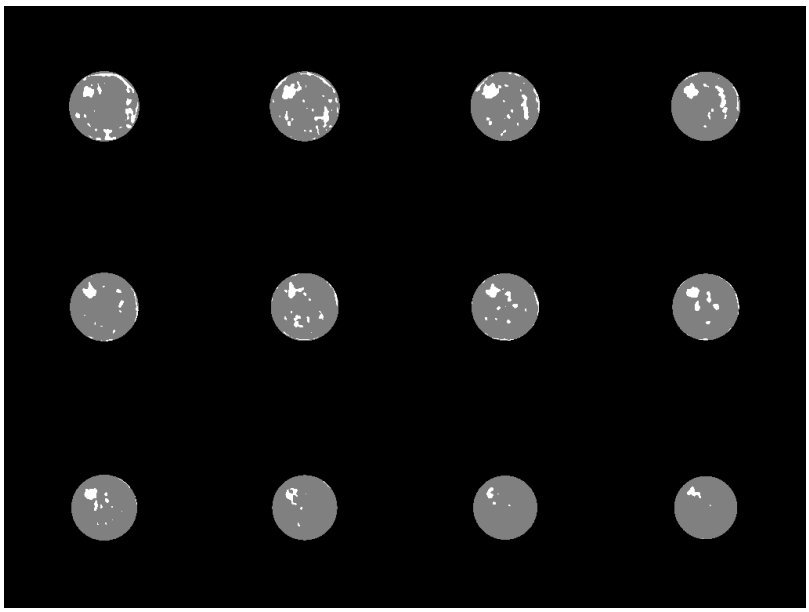

Figure 7.20: Global thresholding results for the non pre-denoised case. Phantom 1.

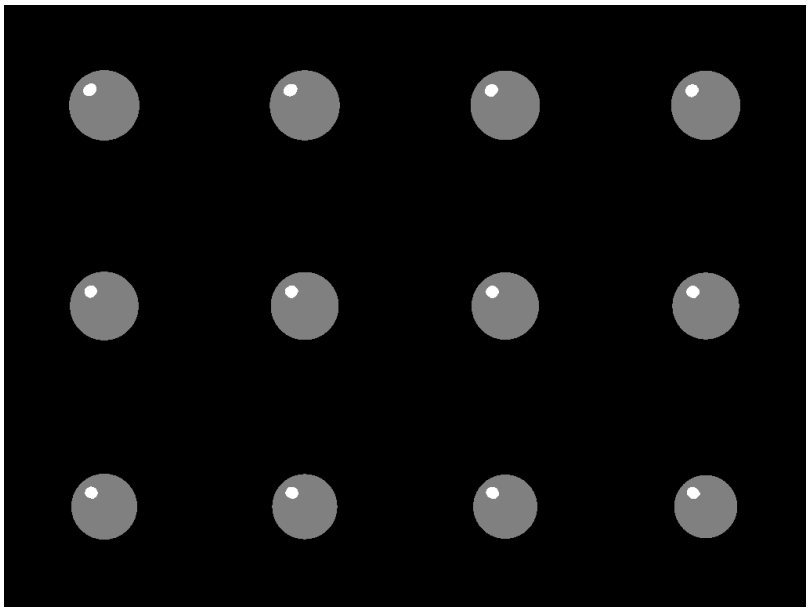

Figure 7.21: Local thresholding results for the ground-truth image. Phantom 1.

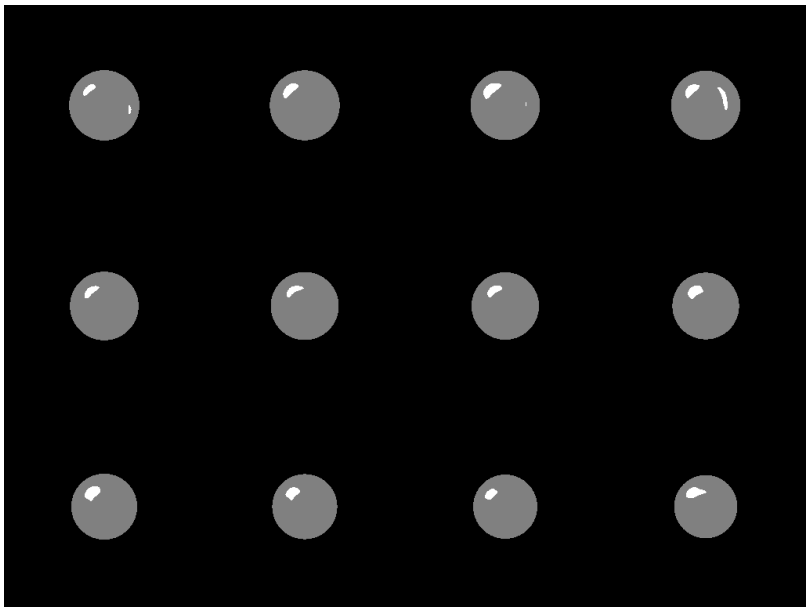

Figure 7.22: Local thresholding results for the pre-denoised case. Phantom 1.

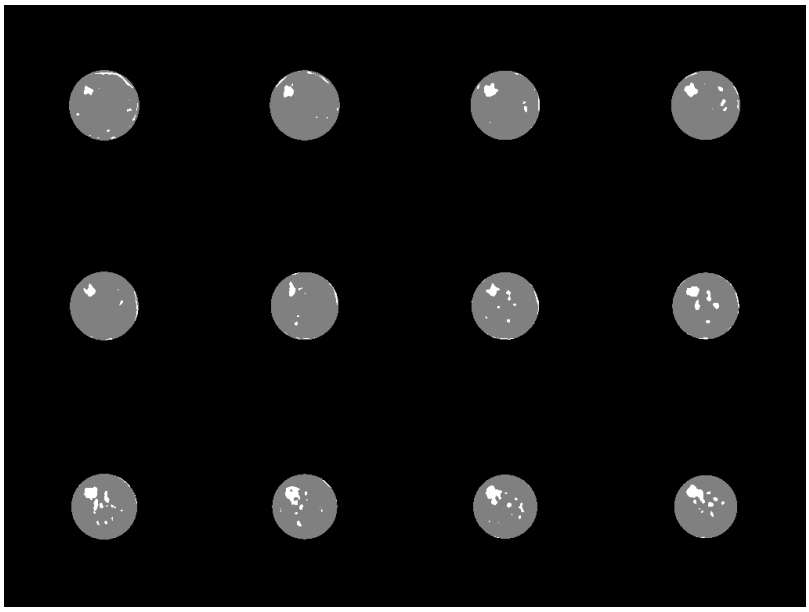

Figure 7.23: Local thresholding results for the non pre-denoised case. Phantom 1.

Thresholding is performed in two ways: globally and locally. The global threshold is a multiple of the mean volume value and is applied to all slices. The local threshold is a multiple of each slice mean value and is calculated for each slice. In both cases, the mean value is calculated inside

a mask discarding the background. Figures 7.18-7.20 and 7.21-7.23 show the results obtained for Phantom 1, the global and local case respectively. Figures 7.24 to 7.26 and 7.27 to 7.29 show the results obtained for Phantom 2, also for the global and local cases.

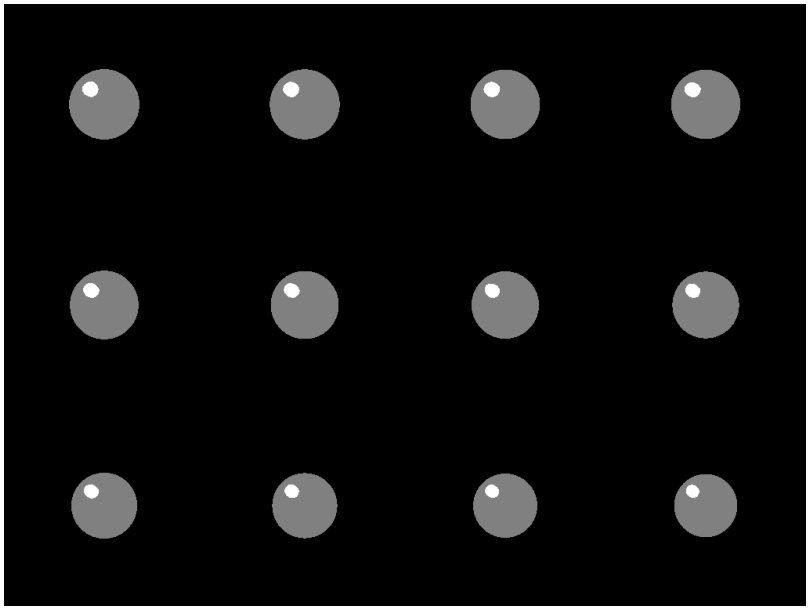

Figure 7.24: Global thresholding results for the ground-truth image. Phantom 2.

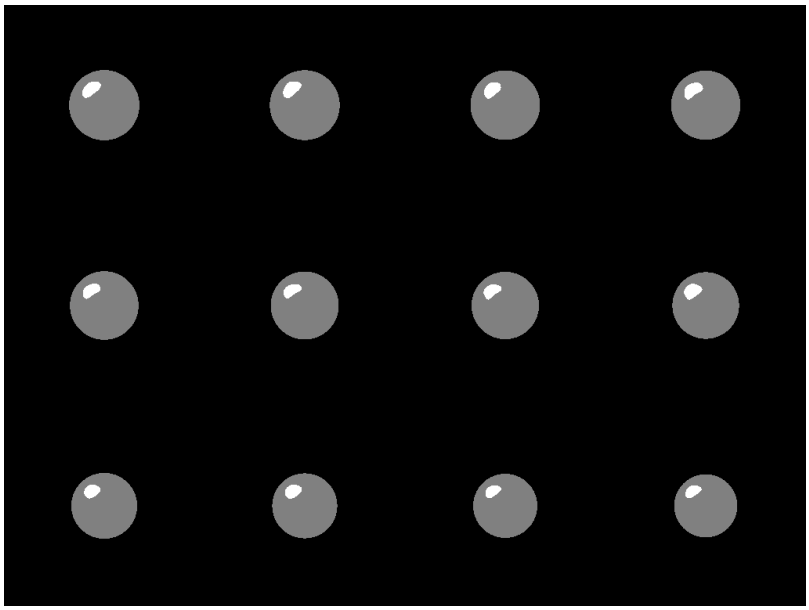

Figure 7.25: Global thresholding results for the pre-denoised case. Phantom 2.

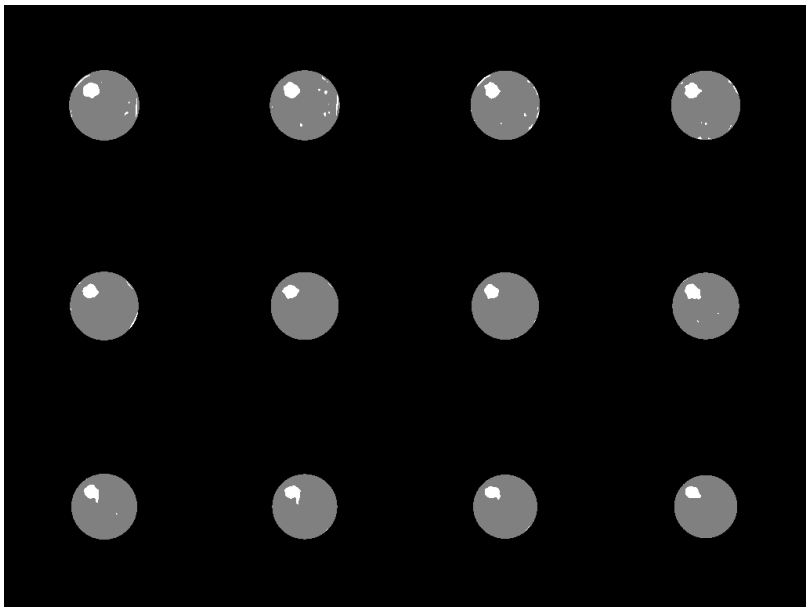

Figure 7.26: Global thresholding results for the non pre-denoised case. Phantom 2.

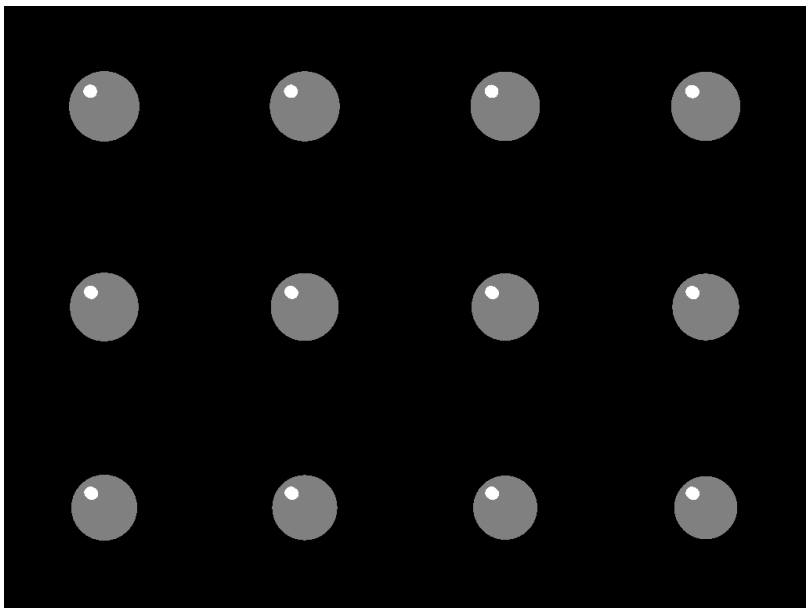

Figure 7.27: Local thresholding results for the ground-truth image. Phantom 2.

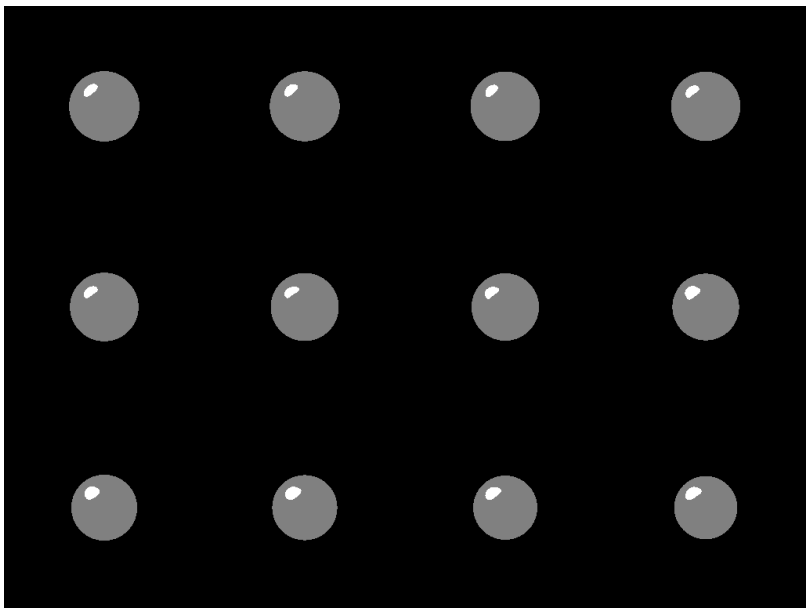

Figure 7.28: Local thresholding results for the pre-denoised case. Phantom 2.

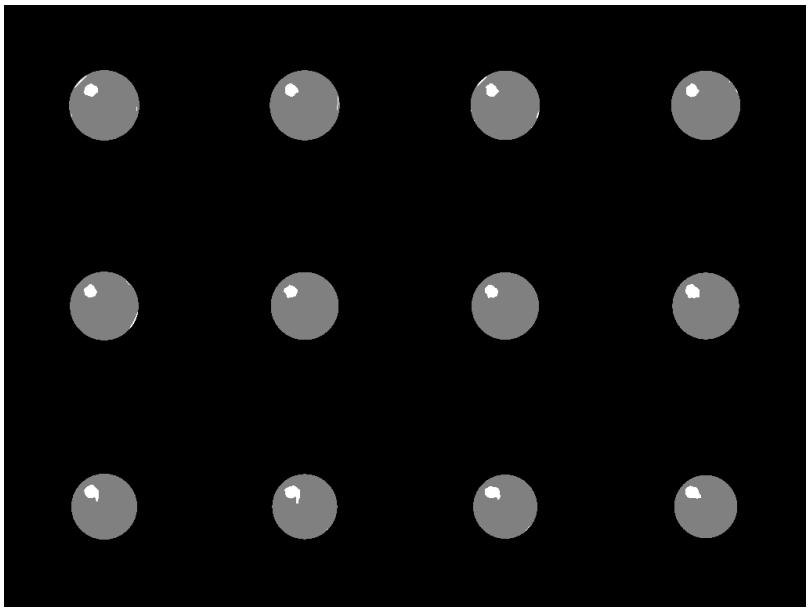

Figure 7.29: Local thresholding results for the non pre-denoised case. Phantom 2.

Chapter 8

Conclusions and future work

In the present work we conducted an exhaustive analysis of the SPECT image formation process. A mathematical model of the SPECT images acquisition was presented, for the case of Anger like gamma cameras. This model led to the statistical characterization of the SPECT sinograms as independent Poisson distributed random variables. This characterization of SPECT sinograms is widely known and accepted in the scientific community [5, 6, 7]. However, to the best of our knowledge, a detailed analysis of the acquisition process and justification of the validity of the previous assumption is not presented. In this work we analyzed each step of the acquisition process, starting from the 3D volumetric emission, considering photon evolution throughout the volume and the acquisition process itself, in order to understand in depth the process, study the applicability of the model and justify each assumption that is made. A statistical characterization was also presented for the post-reconstruction images. The approach of Barrett et al. [8] proposes a statistical model of the ML-EM reconstructed images. They show that, up to an approximation, the reconstructed image follows a multivariate log-normal law. The extension of this analysis for OSEM reconstructed images [42] was also presented.

The SPECT image model that was obtained encouraged the reconsideration of the a-contrario EZ localization method we had previously introduced in [1]. The new a-contrario EZ detection method introduces the following changes: the incorporation of the new background model, based on that of Barrett et al. [8]; a new measurement, combining a global and a local approach; the testing of different scales (multi-scale approach); the computation of different NFA thresholds for each scale, inspired in the method of Burrus et al. [9]. The performance of the new a-contrario method was evaluated using both phantoms and real scans.

Regarding the new a-contrario detection method, we found that it maintains positive features of the previous approach such as: robustness to alignment and masking problems, correct foci definition and low number of false positives. Some improvements were found in the experimental evaluation. One of the most remarkable is the greater sensitivity of the new method (a lower detectable activity threshold). The new threshold is less restrictive than the previous one, allowing the reduction of false negatives, which is critical in the EZ localization application. Moreover, the reduction on the false negatives is achieved without a significant increase in false positives. In some cases, we even found a reduction on the number of false positives. The new threshold also allows the emergence of new detections that belong to the seizure activation circuit. This aspect is remarkable since the highly restrictive thresholding of the old a-contrario method gives *clean* images (low number of false detections) which are not in accordance with reality. The perfusion circuits are complex and several brain regions are active during the seizure. Finally, greater intensity level of the EZ was found in some cases (not all cases).

The SPECT image model also inspired the application of a denoising technique to perform sinograms denoising. The method, introduced by Deledalle et al. [48], is an extension of NL means

denoising for the case of images corrupted by Poisson noise. The denoising performance was evaluated using phantoms and real scans. In both cases good results are obtained. In particular, for real scans, the denoising method seems to improve edges definition and better distinguish small adjacent structures. Moreover, it seems to increase the intensity in areas of low uptake, as the temporal lobes, which is a positive aspect. On the other hand, the reconstructed images, even after the post-processing, are a little noisy. For this reason, results obtained with a low-pass filtering post-processing are preferred to those without it. Finally, results are promising and it would be interesting to test some variations of the denoising approach and analyze a larger number of real cases.

Some interesting ideas came up from the work and we would like to include them as future work. First it would be interesting to create a more complex statistical model of SPECT images, that takes into account its spatial variability caused by the brain physiology. For that purpose, it may be useful to create a brain map assigning different variability to each region depending on its functional characteristics. This model could be applied to both EZ detection and sinograms denoising. In particular, for EZ detection, it would be interesting to develop a probability map that reflects the probability of an EZ to be on each brain region. This map could be included as a prior to the detection task, incorporating part of the a priori knowledge acquired in medical practice. For example, a simple map would be a segmentation of white and grey matter, since EZ only appear on the latter.

It is important to do a more exhaustive evaluation of the new a-contrario detection method using phantoms, including alignment problems and other non-idealities. The evaluation on more real patients is also crucial.

The reconstructed images obtained from denoised sinograms no longer follow the statistical model introduced by Barrett et al. since the denoising filter is nonlinear. It would be interesting to propose a new image model for that case in order to apply the a-contrario detection approach. For example, the new model could be based on a linearization of the denoising filter. On the other hand, it would be interesting to derive a new detection technique that makes use of the denoised image characteristics.

Appendices

Appendix A

V(r) expected value

In order to find $\mathrm{E}[\mathbf{V}(\mathbf{r})]$, let us begin by calculating the conditional expected value [5]

$$\mathrm{E}[\mathbf{V}(\mathbf{r})|\mathbf{K}=k],$$

$$\begin{aligned}\mathrm{E}[\mathbf{V}(\mathbf{r})|\mathbf{K}=k] &= \int\dots\int\sum_{j=1}^{k}\delta(\mathbf{r}-\mathbf{r}_j)p(\mathbf{r}_1)\dots p(\mathbf{r}_k)d\mathbf{r}_1\dots d\mathbf{r}_k \\ &= \int\dots\int[\delta(\mathbf{r}-\mathbf{r}_1)+\dots+\delta(\mathbf{r}-\mathbf{r}_k)]p(\mathbf{r}_1)\dots p(\mathbf{r}_k)d\mathbf{r}_1\dots d\mathbf{r}_k \\ &= \sum_{j=1}^{k}\underbrace{\int\dots\int\delta(\mathbf{r}-\mathbf{r}_j)p(\mathbf{r}_1)\dots p(\mathbf{r}_k)d\mathbf{r}_1\dots d\mathbf{r}_k}_{t_j}\end{aligned} \tag{A.1}$$

We proceed to calculate one of the terms t_j of the previous sum. We take for example $j=1$ and calculate t_1 as

$$\begin{aligned}t_1 &= \int\dots\int\delta(\mathbf{r}-\mathbf{r}_1)p(\mathbf{r}_1)\dots p(\mathbf{r}_k)d\mathbf{r}_1\dots d\mathbf{r}_k \\ &\overset{(1)}{=} \int\dots\int p(\mathbf{r})p(\mathbf{r}_2)\dots p(\mathbf{r}_k)d\mathbf{r}_2\dots d\mathbf{r}_k \\ &= p(\mathbf{r})\int\dots\int p(\mathbf{r}_2)\dots p(\mathbf{r}_k)d\mathbf{r}_2\dots d\mathbf{r}_k \\ &\overset{(2)}{=} p(\mathbf{r})\end{aligned} \tag{A.2}$$

(1) $\int\delta(\mathbf{r}-\mathbf{r}_1)p(\mathbf{r}_1)d\mathbf{r}_1 = p(\mathbf{r})$
(2) $\int p(\mathbf{r}_i)d\mathbf{r}_i = 1$

Note that the result of (A.2) does not depend on the chosen j value, i.e. the result is valid for all the terms t_j.

Thus from (A.1) and (A.2) we have,

$$\mathrm{E}[\mathbf{V}(\mathbf{r})|\mathbf{K}=k] = \sum_{j=1}^{k}p(\mathbf{r}) = kp(\mathbf{r})$$

At last we find $\mathrm{E}[\mathbf{V}(\mathbf{r})]$ as

$$\begin{aligned}
\mathrm{E}[\mathbf{V}(\mathbf{r})] &= \sum_{k=0}^{\infty} \mathrm{E}[\mathbf{V}(\mathbf{r})|\mathbf{K}=k] P_{\mathbf{K}}[\mathbf{K}=k] \\
&= \sum_{k=0}^{\infty} k p(\mathbf{r}) P_{\mathbf{K}}[\mathbf{K}=k] \\
&= p(\mathbf{r}) \sum_{k=0}^{\infty} k P_{\mathbf{K}}[\mathbf{K}=k] \\
&\overset{(3)}{=} \lambda p(\mathbf{r})
\end{aligned} \tag{A.3}$$

(3) $\sum_{k=0}^{\infty} k P_{\mathbf{K}}[\mathbf{K}=k] = \mathrm{E}[\mathbf{K}] = \lambda$

Appendix B

Pearson Chi-square test

Pearson's chi-square goodness of fit test is a non-parametric test of goodness of adjustment to a given distribution. Given n observations $(X_1, \ldots, X_n)$ of an unknown distribution, we define the m classes $(c_1, \ldots, c_m)$ as a partition of the set of possible values. The empirical distribution is then defined as

$$\hat{P}(c_k) = \frac{1}{n} \sum_{i=1}^{n} \mathbf{1}_{c_k}(X_i),$$

where $\mathbf{1}_{c_k}(X_i)$ is the indicator function taking value 1 when X_i belongs to class c_k.
The hypothesis to test $\mathcal{H}_0$ is,

$$\mathcal{H}_0 \quad : \quad P[X_i \in c_k] = P_0(c_k), \forall k = 1, \ldots, m$$

with P_0 the theoretical distribution to be tested for adjustment to samples $(X_1, \ldots, X_n)$. Under $\mathcal{H}_0$, the empirical distribution should be close to P_0. The level of adjustment between both distributions is measured by the chi-square test statistic $D_{\chi^2}(P_0, \hat{P})$,

$$D_{\chi^2}(P_0, \hat{P}) = \sum_{i=1}^{m} \frac{(P_0(c_i) - \hat{P}(c_i))^2}{P_0(c_i)}.$$

Under $\mathcal{H}_0$, the probability distribution of the random variable $nD_{\chi^2}(P_0, \hat{P})$ converges, for $n \to \infty$, to the chi-square probability distribution of parameter $m - 1$. Otherwise, if $\mathcal{H}_0$ is false, $nD_{\chi^2}(P_0, \hat{P})$ diverges to infinity. Thus the null hypothesis is rejected for very large values of the statistic. Since the previous result is asymptotic, the sample size must be large enough to guarantee the test confidence. Samples sizes at least in the order of hundreds are usually recommended.

Appendix C

Rank Correlation Coefficients

C.1. Spearman's rank correlation

Spearman's rank correlation coefficient is a non-parametric measure of statistical dependence between random variables. It evaluates monotonic relationships between variables, i.e. either the variables increase in value together, or one decreases when the other increases.
Let $\mathbf{X}$ and $\mathbf{Y}$ be two random variables with sample values $(X_1, \ldots, X_n)$ and $(Y_1, \ldots, Y_n)$ respectively. Let $(x_1, \ldots, x_n)$ and $(y_1, \ldots, y_n)$ be the ranks associated to $\mathbf{X}$ and $\mathbf{Y}$ sample values. In the case of no tied ranks, Spearman's coefficient of rank correlation ρ is then given by

$$\rho = 1 - \frac{6 \sum_i d_i^2}{n(n^2 - 1)},$$

where $d_i = x_i - y_i$ and n is the sample size. If tied ranks exists, Pearson's correlation coefficient formula should be used instead,

$$\rho = \frac{\sum_i (x_i - \bar{x})(y_i - \bar{y})}{\sqrt{\sum_i (x_i - \bar{x})^2 \sum_i (y_i - \bar{y})^2}}.$$

C.2. Kendall's rank correlation

Let $(X_1, Y_1), \ldots, (X_n, Y_n)$ be a set of joint observations of two random variables $\mathbf{X}$ and $\mathbf{Y}$. Two pairs (X_i, Y_i),(X_j, Y_j) are called *concordant* if the product $(X_i - X_j)(Y_i - Y_j)$ is positive, i.e. if the sign of the difference between the X and Y components is the same, and *discordant* if the product is negative. If C is the number of concordant pairs and D is the number of discordant pairs, the Kendall's rank correlation coefficient τ is defined as,

$$\tau = \frac{2(C - D)}{n(n - 1)}$$

Thus τ is the proportion of concordant minus discordant pairs ($n(n-1)/2$ is the number of possible pair comparisons). For a pair of objects taken at random, τ can be interpreted as the difference between the probability for this objects to be in the same order and the probability of these objects being in a different order. τ takes values between -1 and 1, with 1 obtained when both orders are identical and -1 when the order is the exact reverse.

Appendix D

Post-reconstruction Noise - C and D matrices

For the ML-EM case, under *Approximation 1* and *Approximation 2*, matrix $C^{(k)}$ is expressed in terms of its elements as

$$[C^{(k)}]_{ij} = \frac{A_j^{(k)}}{s_i} \sum_{m=1}^{M} \left(\frac{H_{mi} H_{mj}}{\sum_{n=1}^{N} H_{mn} A_n^{(k)}} \right),$$

and matrix $D^{(k)}$ as

$$[D^{(k)}]_{ij} = \frac{H_{ij}}{s_i \sum_{n=1}^{N} H_{jn} A_n^{(k)}}.$$

For the OSEMcase, under *Approximation 1* and *Approximation 2*, matrix $C_m^{(k)}$ is expressed in terms of its elements as

$$[C_m^{(k)}]_{ij} = \frac{A_j^{(k)}}{s_i} \sum_{m=1}^{M} \left(\frac{[H_m]_{mi} H_{mj}}{\sum_{n=1}^{N} H_{mn} A_n^{(k)}} \right),$$

and matrix $D_m^{(k)}$ as

$$[D_m^{(k)}]_{ij} = \frac{[H_m]_{ij}}{s_i \sum_{n=1}^{N} H_{jn} A_n^{(k)}}.$$

Bibliography

[1] P. Musé C. Aguerrebere, P. Sprechmann and R. Ferrando. A-contrario localization of epileptogenic zones in spect images. In *Proceedings of the Sixth IEEE international conference on Symposium on Biomedical Imaging: From Nano to Macro*, ISBI'09, pages 570–573, Piscataway, NJ, USA, 2009. IEEE Press.

[2] A. LeBron Paige G. Varghese H. Zhang E.J. Novotny S.S. Spencer I.G. Zubal K.A., McNally and H. Blumenfeld. Localizing value of Ictal-interictal SPECT Analyzed by SPM (ISAS). *Epilep.*, 9:1450–64, 2005.

[3] B. P. Mullan B. H. Brinkmann D. Hanson C. R. Jack T. J. O'Brien, M.K. O'Connor and E. L. So. Subtraction ictal spet co-registered to mri in partial epilepsy: Description and validation of the method with phantom and patient studies. *Nuclear medicine communications*, 19:31–45, 1998.

[4] L. Moisan A. Desolneux and J. M. Morel. *From Gestalt Theory to Image Analysis*. Springer-Verlag, 2008.

[5] H. Barrett, hJ. Myers, and S. Dhurjaty. Foundations of Image Science. *Journal of Electronic Imaging*, 14(2):029901, 2005.

[6] H. Barrett and W. Swindell. *Radiological Imaging: The Theory of Image Formation, Detection, and Processing*. Academic Press, October 1996.

[7] A. Macovski. *Medical Imaging Systems*. Prentice-Hall, 1983.

[8] H. H. Barrett, D. W. Wilson, and B. M. Tsui. Noise properties of the EM algorithm: I. Theory. *Phys Med Biol*, 39(5):833–846, May 1994.

[9] T. M. Bernard N. Burrus and J.M. Jolion. Image segmentation by a contrario simulation. *Pattern Recogn.*, 42:1520–1532, July 2009.

[10] M. N. Wernick and J. N. Aarsvold. *Introduction to Emission Tomography*, chapter 2, pages 11–23. Emission Tomography: The Fundamentals of PET and SPECT. Elsevier Academic Press, San Diego, USA, 2004.

[11] M. Defrise P. E. Kinahan and R. Clackdoyle. *Analytic Image Reconstruction Methods*, chapter 20, pages 421–442. Emission Tomography: The Fundamentals of PET and SPECT. Elsevier Academic Press, San Diego, USA, 2004.

[12] S. Skiadopoulos, A. Karatrantou, P. Korfiatis, L. Costaridou, P. Vassilakos, D. Apostolopoulos, and G. Panayiotakis. Evaluating image denoising methods in myocardial perfusion single photon emission computed tomography (SPECT) imaging. *Measurement Science and Technology*, 20(10):104023, 2009.

[13] L. A. Shepp and Y. Vardi. Maximum likelihood reconstruction for emission tomography. *IEEE Transactions On Medical Imaging*, 1(2):113 – 122, 1982.

[14] H. M. Hudson and R. S. Larkin. Accelerated image reconstruction using ordered subsets of projection data. *IEEE Trans Med Imaging*, 13(4):601–609, 1994.

[15] A. P. Dempster, N. M. Laird, and D. B. Rubin. Maximum likelihood from incomplete data via the EM algorithm. *Journal of the Royal Statistical Society. Series B (Methodological)*, 39(1):1–38, 1977.

[16] C. Levin. *Basic Physics of Radionuclide Imaging*, chapter 4, pages 53–88. Emission Tomography: The Fundamentals of PET and SPECT. Elsevier Academic Press, San Diego, USA, 2004.

[17] P. Matthews J. Foster, K. Kouris and N. M. Spyrou. Binomial vs Poisson statistics in radiation studies. *Nuclear Instruments and Methods in Physics Research*, 212(1-3):301 – 305, 1983.

[18] M. Wernick R. Mintzer G. Zeng, J. Galt and J. Aarsvold. *Single-Photon Emission Computed Tomography*, chapter 7, pages 127–152. Emission Tomography: The Fundamentals of PET and SPECT. Elsevier Academic Press, San Diego, USA, 2004.

[19] O. Smith Z. Rattner R. Gindi G. Zubal, R. Harrell and B. Hoffer. The zubal phantom, voxel-based anthropomorphic phantoms. *http://noodle.med.yale.edu/zubal/*.

[20] W. Segars. Ncat phantom for medical imaging research.

[21] C. Grova, P. Jannin, A. Biraben, I. Buvat, H. Benali, A.M. Bernard, J.M. Scarabin, and B. Gibaud. A methodology for generating normal and pathological brain perfusion spect images for evaluation of MRI/SPECT fusion methods: application in epilepsy. *Physics in Medicine and Biology*, 48(24):4023–4044, 2003.

[22] I. Buvat and D. Lazaro. Monte Carlo simulations in emission tomography and GATE: An overview. *Nuclear Instruments and Methods in Physics Research Section A: Accelerators, Spectrometers, Detectors and Associated Equipment*, 569(2):323 – 329, 2006.

[23] I. Buvat and I. Castiglioni. Monte Carlo simulations in SPET and PET. *The Quarterly Journal of Nuclear Medicine*, 46:48 – 61, 2002.

[24] D. Haynor S. Gillispie M. Kaplan R. Harrison, S. Vannoy and T. Lewellen. Simulation system for emission tomography (SimSET). *http://depts.washington.edu/simset/html/simset_main.html*, 2009.

[25] M. Ljungberg and S. Strand. A Monte Carlo program for the simulation of scintillation camera characteristics. *Computer Methods and Programs in Biomedicine*, 29(4):257 – 272, 1989.

[26] N.C. Rouze, M. Schmand, S. Siegel, and G.D. Hutchins. Design of a small animal PET imaging system with 1 microliter volume resolution. *Nuclear Science, IEEE Transactions on*, 51(3):757 – 763, jun. 2004.

[27] A. Blanco, N. Carolino, N. C. Ferreira, C. Correia, M. P. Macedo, L. Fazendeiro, M. F. Marques, R. F. Marques, C. Gil, and P. Fonte. RPC-PET: a new very high resolution PET technology. *Nuclear Science Symposium Conference Record, 2004 IEEE*, 4:2356 – 2360 Vol. 4, oct. 2004.

[28] G. Sgouros, E. Frey, R. Wahl, B. He, A. Prideaux, and R. Hobbs. Three-dimensional imaging-based radiobiological dosimetry. *Seminars in Nuclear Medicine*, 38(5):321 – 334, 2008. Radiation Dosimetry and Exposure in Nuclear Medicine.

[29] S. Shokouhi, P. Vaska, S. Southekal, D. Schlyer, M. Purschke, V. Dzordzhadze, C. Woody, S. Stoll, D.L. Alexoff, D. Rubins, A. Villanueva, and S. Krishnamoorthy. Statistical 3D image reconstruction for the RatCAP PET tomograph using a physically accurate, Monte Carlo based system matrix. *Nuclear Science Symposium Conference Record, 2004 IEEE*, 6:3901 – 3905 Vol. 6, oct. 2004.

[30] R. Harrison D. Haynor and T. Lewellen. The use of importance sampling techniques to improve the efficiency of photon tracking in emission tomography simulations. *Medical Physics*, 18(5):990 – 1001, 1991.

[31] D. L. Fried. Noise in photoemission current. *Appl. Opt.*, 4(1):79–80, 1965.

[32] D. W. Wilson, B. M. Tsui, and H. H. Barrett. Noise properties of the EM algorithm: II. Monte Carlo simulations. *Phys Med Biol*, 39(5):847–871, May 1994.

[33] D. Gunter. *Collimator Design for Nuclear Medicine*, chapter 8, pages 153–168. Emission Tomography: The Fundamentals of PET and SPECT. Elsevier Academic Press, San Diego, USA, 2004.

[34] J. Correia R. Ackerman J. Chang S. Finklestein S. Davis G. Brownell N. Alpert, D. Chesler and J. Taveras. Estimation of the local statistical noise in emission computed tomography. *IEEE Transactions On Medical Imaging*, 1(2):142 – 146, 1982.

[35] L. Thomas D. Snyder, M. Miller and D. Politte. Noise and edge artifacts in maximum-likelihood reconstruction for emission tomography. *IEEE transactions on medical imaging*, 6(3):228 – 238, 1987.

[36] J. K. Brown S. C. Liew, B. H. Hasegawa and T. F. Lang. Noise propagation in SPECT images reconstructed using an iterative maximum-likelihood algorithm. *Physics In Medicine And Biology*, 38(12):1713 – 1726, 1993.

[37] D. W. Wilson and B. Tsui. Noise properties of filtered-backprojection and ML-EM reconstructed emission tomographic images. In *IEEE transactions on nuclear science*, volume 40, pages 1198 – 1203, 1993.

[38] J. L. Bernon M. Rossi D. Mariano-Gouland, M. Fourcade and M. Zanca. Experimental study of stochastic noise propagation in SPECT images reconstructed using the conjugate gradient algorithm. *Computerized medical imaging and graphics*, 27(1):53 – 63, 2002.

[39] Jinyi Qi. A unified noise analysis for iterative image estimation. *Physics in Medicine And biology*, 48(21):3505 – 3519, 2003.

[40] J.P. Guillement and R. G. Novikov. A noise property analysis of single-photon emission computed tomography data. *Inverse problems*, 20(1):175 – 198, 2004.

[41] H. Schnieder B. Langstrom E. Maripuu E. Bengtsson P. Razifar, M. Sandstrom and M. Bergstrom. Noise correlation in PET, CT, SPECT and PET/CT data evaluated using autocorrelation function: a phantom study on data, reconstructed using FBP and OSEM. *BMC Medical Imaging*, 5:5, 2005.

[42] E.J. Soares, C.L. Byrne, and S.J. Glick. Noise characterization of block-iterative reconstruction algorithms. i. Theory. *Medical Imaging, IEEE Transactions on*, 19(4):261 –270, apr. 2000.

[43] E.J. Soares, S.J. Glick, and J.W. Hoppin. Noise characterization of block-iterative reconstruction algorithms: II. Monte Carlo simulations. *Medical Imaging, IEEE Transactions on*, 24(1):112 –121, jan. 2005.

[44] PubMed Health. "*http://www.ncbi.nlm.nih.gov/pubmedhealth/PMH0001714*".

[45] B. Grosjean and L. Moisan. A-contrario detectability of spots in textured backgrounds. *Journal of Mathematical Imaging and Vision*, 2008. To appear.

[46] F. Miceli A. Mottini and G. Albin. "Proyecto HDFE, Herramienta de detección de focos epileptógenos". Master's thesis, Facultad de Ingeniería, Universidad de la República, Uruguay, 2009.

[47] K. J. Worsley J.P. Poline C. D. Frith K. J. Friston, A. P. Holmes and R. S. J. Frackowiak. Statistical parametric maps in functional imaging: a general approach. *Hum Brain Mapp.*, 2:189–210, 1995.

[48] C. Deledalle, L. Denis, and F. Tupin. Poisson NL Means: Unsupervised Non Local Means for Poisson noise. *ICIP IEEE Conf.*, 2010.

[49] A. Buades, B. Coll, and J.-M. Morel. A non-local algorithm for image denoising. *Computer Vision and Pattern Recognition, 2005. CVPR 2005. IEEE Computer Society Conference on*, 2:60 – 65 vol. 2, jun. 2005.

[50] Pascal Hannequin and Jacky Mas. Statistical and heuristic image noise extraction (shine): a new method for processing poisson noise in scintigraphic images. *Physics in Medicine and Biology*, 47(24):4329, 2002.

[51] Pascal Hannequin and Jacky Mas. Application of iterative and non-stationary smoothing filters for statistical noise reduction in nuclear medicine. *Nuclear Medicine Communications*, 19:875–85, 1998.

[52] A. Yahil A. Vija and E. Hawman. Preprocessing of SPECT projection data: Benefits and pitfalls. *IEEE Nucl. Sci. Symp. Conf.*, 4:2160–64, 2005.

[53] Y. Jin, E. D. Angelini, P. D. Esser, and A. Laine. De-noising SPECT/PET images using cross-scale regularization. In Randy E. Ellis and Terry M. Peters, editors, *MICCAI (2)*, volume 2879 of *Lecture Notes in Computer Science*, pages 32–40. Springer, 2003.

[54] Klaus E. Timmermann and Robert D. Nowak. Multiscale modeling and estimation of Poisson processes with application to photon-limited imaging. *IEEE Trans. on Information Theory*, 45:846–862, 1999.

[55] R. Willett and R. Nowak. Fast multiresolution photon-limited image reconstruction. In *Proc. IEEE Int. Sym. Biomedical Imaging ISBI 04*, pages 15–18, 2004.

[56] R.D. Nowak and R.G. Baraniuk. Wavelet-domain filtering for photon imaging systems. *Image Processing, IEEE Transactions on*, 8(5):666 –678, may. 1999.

[57] L. Wang, J. Wen, J. Yang, Y. Chen, and Z. Liang. Wavelet based de-noising methods for local SPECT reconstruction with nonuniform attenuation. *Medical Imaging 2009: Physics of Medical Imaging*, 7258(1):72582O, 2009.

[58] L. I. Rudin., S. Osher, and E. Fatemi. Nonlinear total variation based noise removal algorithms. *Physica D: Nonlinear Phenomena*, 60(1-4):259–268, 1992.

[59] N. Dey, L. Blanc-Feraud, C. Zimmer, Z. Kam, J.-C. Olivo-Marin, and J. Zerubia. A deconvolution method for confocal microscopy with total variation regularization. *Biomedical Imaging: Nano to Macro, 2004. IEEE International Symposium on*, pages 1223 – 1226 Vol. 2, apr. 2004.

[60] J. Bardsley and A. Luttman. Total variation-penalized Poisson likelihood estimation for ill-posed problems. *Advances in Computational Mathematics*, 31:35–59, 2009. 10.1007/s10444-008-9081-8.

[61] Xiao-Qun Zhang and J. Froment. Total variation based Fourier reconstruction and regularization for computer tomography. *Nuclear Science Symposium Conference Record, 2005 IEEE*, 4:2332 – 2336, oct. 2005.

[62] R.M. Willett and R.D. Nowak. Platelets for multiscale analysis in medical imaging. *EMBS/BMES Conference, 2002. Proceedings of the Second Joint*, 2:1023 – 1024 vol.2, 2002.

[63] R. Willett and R. Nowak. Platelets: A multiscale approach for recovering edges and surfaces in photon limitedmedical imaging. *IEEE Trans. Med. Imaging*, 22(3):332–350, 2003.